EUROPEAN ORGANIZATION FOR NUCLEAR RESEARCH

CERN-PH-EP/2009-006
5 March 2009

Inclusive production of protons, anti-protons and neutrons in p+p collisions at 158 GeV/c beam momentum

T. Anticic[15], B. Baatar[6], J. Bartke[4], L. Betev[8], H. Białkowska[14], C. Blume[7], B. Boimska[14], J. Bracinik[1,a], V. Cerny[1], O. Chvala[11,b], J. Dolejsi[11], V. Eckardt[10], H.G. Fischer[8], Z. Fodor[3], P. Foka[5], V. Friese[5], M. Gaździcki[7], C. Höhne[5], K. Kadija[15], A. Karev[8], V. Kolesnikov[6], M. Kowalski[4], M. Kreps[1,c], M. Makariev[13], A. Malakhov[6], M. Mateev[12], G. Melkumov[6], M. Mitrovski[7], S. Mrówczyński[9], R. Renfordt[7], M. Rybczyński[9], A. Rybicki[4], A. Sandoval[5], N. Schmitz[10], P. Seyboth[10], G. Stefanek[9], R. Stock[7], H. Ströbele[7], T. Susa[15], P. Szymanski[14], V. Trubnikov[14], D. Varga[2], G. Vesztergombi[3], D. Vranić[5], S. Wenig[8],Z. Włodarczyk[9], A. Wojtaszek[9]

(The NA49 Collaboration)

[1]Comenius University, Bratislava, Slovakia
[2] Eötvös Loránt University, Budapest, Hungary
[3]KFKI Research Institute for Particle and Nuclear Physics, Budapest, Hungary
[4]H. Niewodniczański Institute of Nuclear Physics, Polish Academy of Sciences, Cracow, Poland
[5]Gesellschaft für Schwerionenforschung (GSI), Darmstadt, Germany.
[6]Joint Institute for Nuclear Research, Dubna, Russia.
[7]Fachbereich Physik der Universität, Frankfurt, Germany.
[8]CERN, Geneva, Switzerland
[9]Institute of Physics Świętokrzyska Academy, Kielce, Poland.
[10]Max-Planck-Institut für Physik, Munich, Germany.
[11]Charles University, Faculty of Mathematics and Physics, Institute of Particle and Nuclear Physics, Prague, Czech Republic
[12]Atomic Physics Department, Sofia University St. Kliment Ohridski, Sofia, Bulgaria
[13]Institute for Nuclear Research and Nuclear Energy, BAS, Sofia, Bulgaria
[14]Institute for Nuclear Studies, Warsaw, Poland
[15]Rudjer Boskovic Institute, Zagreb, Croatia
[a]now at School of Physics and Astronomy, University of Birmingham, Birmingham, UK
[b]now at UC Riverside, Riverside, CA, USA
[c]now at Institut fur Experimentelle Kernphysik, Karlsruhe, DE

to be published in EPJC

Abstract

New data on the production of protons, anti-protons and neutrons in p+p interactions are presented. The data come from a sample of 4.8 million inelastic events obtained with the NA49 detector at the CERN SPS at 158 GeV/c beam momentum. The charged baryons are identified by energy loss measurement in a large TPC tracking system. Neutrons are detected in a forward hadronic calorimeter. Inclusive invariant cross sections are obtained in intervals from 0 to 1.9 GeV/c (0 to 1.5 GeV/c) in transverse momentum and from -0.05 to 0.95 (-0.05 to 0.4) in Feynman x for protons (anti-protons) respectively. p_T integrated neutron cross sections are given in the interval from 0.1 to 0.9 in Feynman x. The data are compared to a wide sample of existing results in the SPS and ISR energy ranges as well as to proton and neutron measurements from HERA and RHIC.

1 Introduction

In the framework of its extensive experimental programme concerning soft hadronic interactions at SPS energies, the NA49 collaboration has recently published detailed data on the inclusive production of charged pions in p+p collisions [1]. The present paper extends this study to the baryonic sector by providing inclusive cross sections for protons, anti-protons and neutrons. The aim is again to obtain precise sets of data covering the available phase space as densely and completely as possible in accordance with the available event statistics and the limitations set by the NA49 detector layout.

As in the case of pions, the experimental situation in the SPS energy range is far from being satisfactory also for baryons. The presently available data sets suffer from insufficient coverage and at least partially large systematic and statistical error margins. It is therefore one of the main aims of this study to provide a concise overview and evaluation of the experimental situation on a quantitative basis.

This paper is arranged as follows. The present experimental situation is discussed in Sect. 2. Section 3 concentrates on those aspects of the NA49 experiment which are special to baryon detection, as for instance high momentum tracking and neutron calorimetry. The acceptance coverage and the binning scheme are presented in Sect. 4, followed by the description of charged particle identification in Sect. 5. The evaluation of invariant cross sections and of the applied corrections is given in Sect. 6. Results concerning double differential cross sections for protons and anti-protons are presented in Sect. 7, followed by a detailed comparison to existing data in Sects. 8 and 9. Sections 10 and 11 show p_T integrated results for protons and neutrons including a comparison to other experiments. Finally in Sect. 12 the NA49 results on proton and neutron production are compared to baryon production in deep inelastic lepton scattering from HERA.

2 The Experimental Situation

Concerning the present publication we are interested in the available measurements of the double differential cross section of identified baryons,

$$\frac{d^2\sigma}{dx_F dp_T^2}, \tag{1}$$

as a function of the phase space variables defined in this paper as transverse momentum p_T and reduced longitudinal momentum

$$x_F = \frac{p_L}{\sqrt{s}/2} \tag{2}$$

where p_L denotes the longitudinal momentum component in the cms.

Defining a range of beam momenta from 100 to about 400 GeV/c as SPS/Fermilab energy range, quite a few experiments have published inclusive particle yields [2–10]. The corresponding data coverage of the p_T/x_F plane is shown in Fig. 1a for protons and in Fig. 1d for anti-protons. It is apparent from these plots that data are scarce in the regions of p_T below 0.3 GeV/c and above 1 GeV/c as well as x_F below 0.3. At large x_F there is abundant coverage only for protons in a p_T interval from about 0.2 to 0.6 GeV/c from experiments concentrating on single diffraction. It is therefore mandatory to also regard data from the ISR [11–19] at least in the overlapping region of $\sqrt{s}$ up to 30 GeV for this comparison. The corresponding phase space regions are presented in Figs. 1b and 1e for protons and anti-protons, respectively. Ex-

cept for a rather complete coverage at x_F close to zero a lack of data in the intermediate region $0.1 < x_F < 0.4$, at p_T below 0.3 GeV/c and above about 1.5 GeV/c is evident.

The NA49 phase space coverage, Figs. 1c and 1f, is essentially only limited by counting statistics at large p_T, and at large x_F for the anti-protons. In addition there is a small phase space gap not accessible due to the interaction trigger, in a p_T range below 0.05 GeV/c at x_F = 0.6 to 0.4 GeV/c at x_F = 0.95 which only concerns protons.

For neutrons, the situation is less favourable. There is only one measurement from Fermilab [20] and one ISR experiment [21, 22], with coverages shown in Fig. 1g and 1h. Due to lack of transversal granularity, the NA49 calorimeter only allows for the measurement of p_T integrated neutron yields. The corresponding p_T/x_F coverage, limited by the fiducial dimension of the calorimeter, is shown in Fig. 1i.

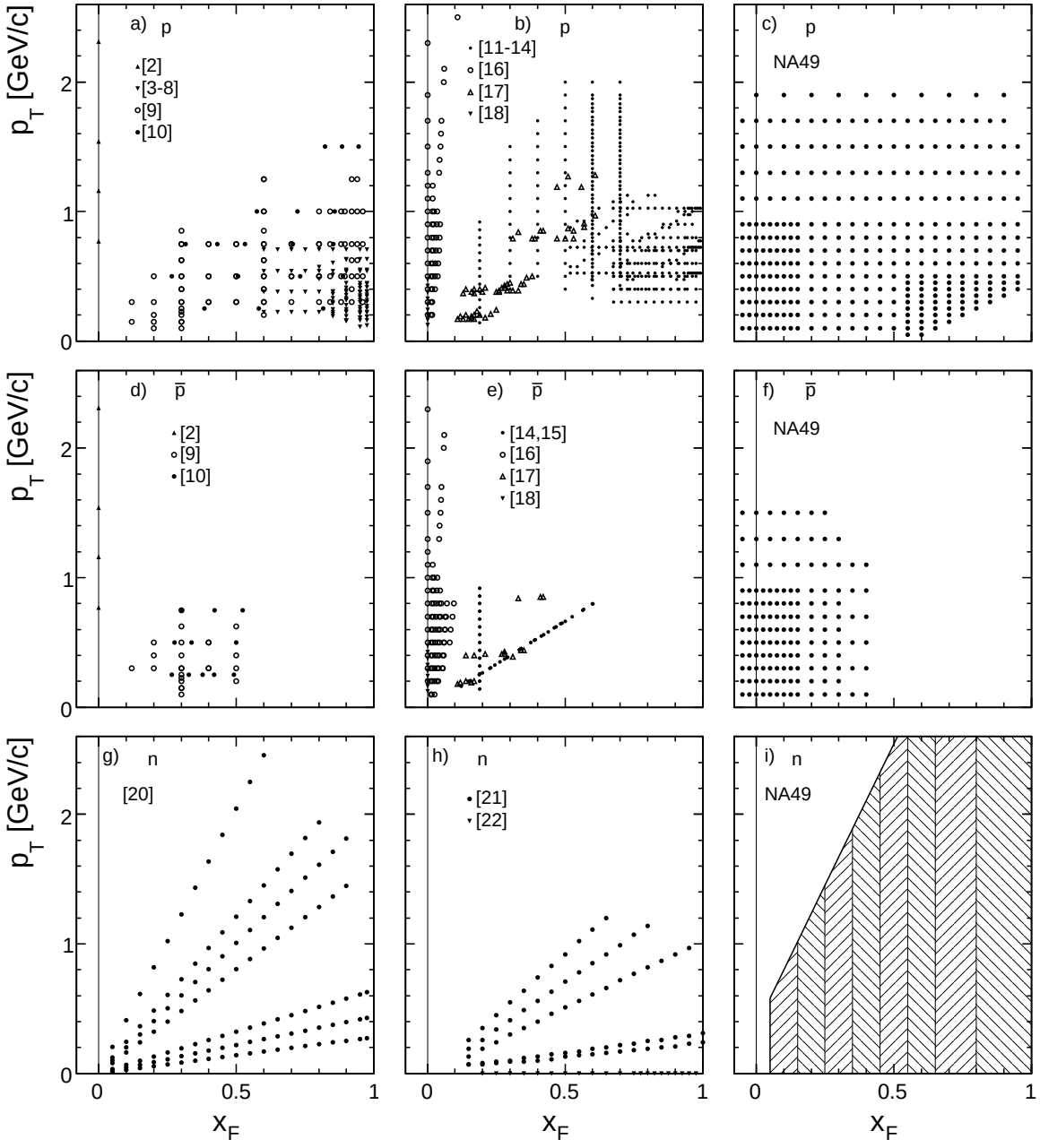

Figure 1: Phase space coverage of existing data

It is useful to repeat here that the main aim of the present paper is to contribute precise new data covering the accessible phase space as densely and continuously as possible in a single experiment in order to clarify the unsatisfactory experimental situation and to provide a sound base for the comparative study of the more complex nuclear interactions.

3 The NA49 Experiment

The basic features of the NA49 detector have been described in detail in references [1,23]. The top view shown in Fig. 2 recalls the main components.

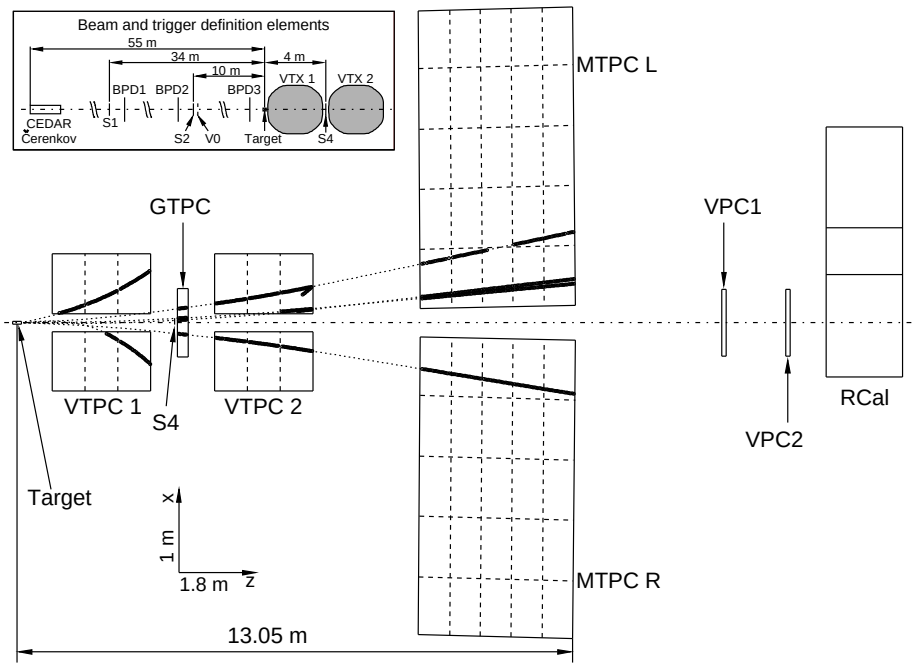

Figure 2: NA49 detector layout and real tracks of a typical mean multiplicity p+p event. The thick lines give the points registered in the TPC's, the dotted lines are the interpolation trajectories between the track segments and the extrapolations to the event vertex in the LH_2 target. The beam and trigger definition counters are presented in the inset

The beam is defined by a CEDAR Cerenkov counter, several scintillation counters (S1, S2, V0) and a set of high precision proportional chambers (BPD1-3). The hydrogen target is placed in front of two superconducting Magnets (VTX1 and VTX2). Four large volume Time Projection Chambers (VTPC1 and VTPC2 inside the magnetic fields, MTPCL and MTPCR downstream of the magnets) provide for charged particle tracking and identification. A smaller Time Projection Chamber (GTPC) placed between the two magnets together with two Multiwire Proportional Chambers (VPC1 and VPC2) in forward direction allows tracking in the high momentum region through the gaps between the principal track detectors. A Ring Calorimeter (RCal) closes the detector setup 18 m downstream of the target.

As details of the beam and target setup, the trigger definition as well as the event and track selection have been given in [1] only those parts of the detector which are of special interest for the present paper will be described here. This concerns in particular the extension of the acceptance into the large x_F region and the neutron calorimetry.

3.1 Tracking at high momenta using the GTPC and VPC's

The particles originating from the primary interaction vertex and missing, at high momentum, the main TPC arrangement, are detected in the GTPC and VPC's. These three sets of points are sufficiently far from each other to provide a reasonable lever arm for momentum measurement. A sketch of this detector part is shown in Fig. 3. For experimental details see [24].

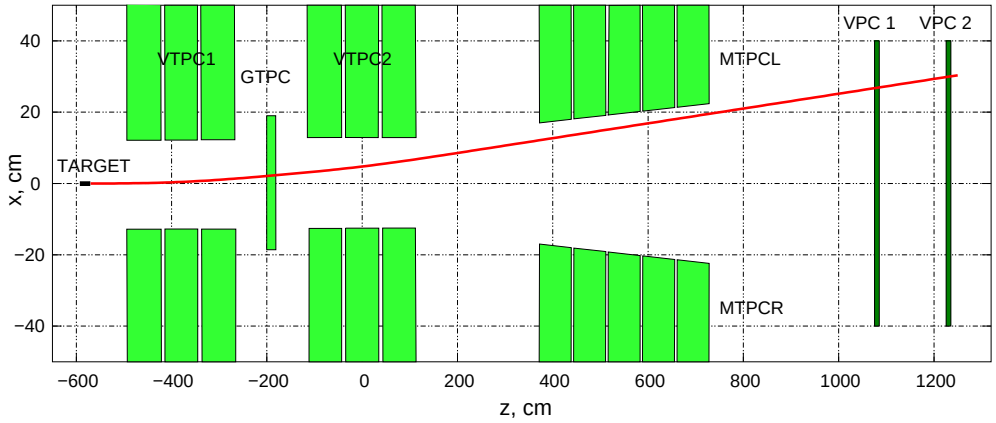

Figure 3: Forward proton detection with the GTPC and the VPC-s: the trajectory of a 110 GeV particle is shown. The scale is stretched in the x direction

The VPC proportional chambers feature a single sense wire plane with strip readout ($\pm$30 degree inclination) on both cathode surfaces resulting in a space resolution of 2 mm. This results, together with the GTPC resolution of less than 150 μm, in a longitudinal momentum resolution of

$$\frac{\Delta p_z}{p_z} \approx 0.013\% \times p_z(\text{GeV/c}) \tag{3}$$

where the error is dominated by the VPC position resolution. The momentum resolution at maximum momentum was controlled using a trigger on beam particles. For inelastic events, it is also established by the width of the diffractive peak as shown in the raw p_z distribution in Fig. 4.

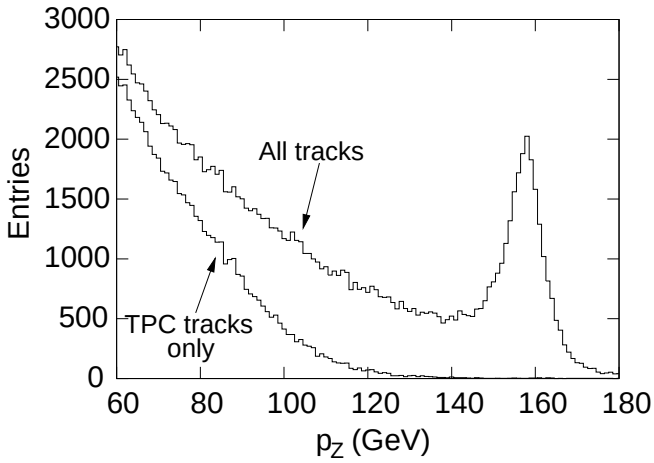

Figure 4: Raw p_z distribution in p+p interaction. The diffractive peak is clearly visible. Lower histogram VTPC+MTPC tracking, upper histogram GTPC+VPC tracking added

The general improvement of charged particle acceptance at $x_F > 0.4$ due to this detector combination, as compared to the tracks visible in the main TPC detector only, is also apparent from Fig. 4.

The corresponding transverse momentum resolution is given by

$$\Delta p_T \approx 2 \times 10^{-4} p_z. \tag{4}$$

It is dominated by both the GTPC and the transverse vertex resolutions. The resulting uncertainty of 30 MeV/c at beam momentum is small enough to allow the extraction of transverse momentum distributions up to the kinematic limit.

3.2 Neutron detection

Forward neutrons as well as fast forward charged particles are detected in the Ring Calorimeter (RCal). This device, originally designed for the study of jet production in deep inelastic interactions by the CERN NA5 experiment [25–27], is placed 18 m downstream of the target. It is a cylindrical structure with azimuthal and radial subdivision into 240 cells, each with an electromagnetic and hadronic compartment.

For the present purpose, it was off-centered with respect to the beam axis such that a fully sensitive fiducial area of 80×160 cm^2 corresponding to the size of the VPC chambers could be established, see Fig. 2. This corresponds to a p_T cut-off of 1.25 GeV/c at x_F = 0.2, increasing to more than 2 GeV/c at $x_F > 0.4$, for neutral particles.

Each RCal cell is built up from 2 parts: an electromagnetic part (20 radiation lengths of Pb/scintillator sandwich) and a hadronic part (4 interaction lengths of Fe/scintillator sandwich) [26]. Energy deposits in the two parts are recorded separately. As the position resolution of the RCal is rather limited in the transverse plane due to the substantial cell size, only p_T integrated x_F distributions are presented in this paper. For experimental details see [24].

3.2.1 Veto against charged particles

The VPC detectors are essential for the discrimination between charged and neutral hadrons impinging on the RCal. The geometrical situation is shown in Fig. 5, where the VPC acceptance is superposed to the r/ϕ structure of the calorimeter.

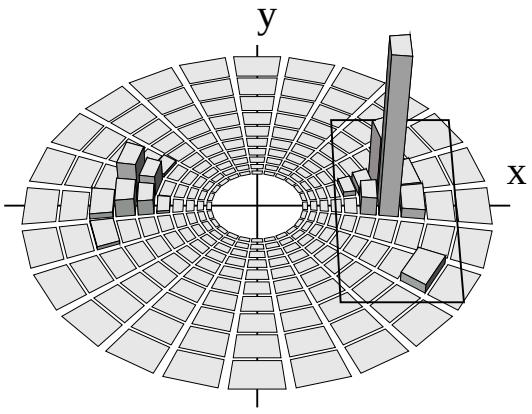

Figure 5: Example of an event in which the RCal energy deposit is not associated with a VPC hit. The VPC fiducial area is projected on the RCal

As the efficiency of the VPC detectors for charged particles has been measured to be higher than 99%, the presence of a calorimeter cluster together with the absence of a corresponding hit in the VPC surface yields a clean selection of neutral particles. In the case of multiple-hit patterns the equality of the signal amplitudes induced on the cathode surface by a traversing particle was used for pattern recognition by matching equal-amplitude strip combinations.

Two reliable tests of the VPC-RCal performance using external constraints were developed. The first one uses the fact that the vast majority of fast forward tracks is of positive charge. In case of VPC inefficiency this would lead, due to the bending of charged tracks in the magnetic field, to a noticeable left-right asymmetry of neutron detection. The second test uses the GTPC information as additional constraint on charged trajectories. In both cases a reliable assessment of the systematic errors is obtained.

3.2.2 Calorimeter calibration and performance

The RCal calibration was performed with beam particles of 40 and 158 GeV/c momentum. The resulting hadronic energy resolution can be parametrized by the following expression:

$$\frac{\sigma(E)}{E} = \sqrt{\frac{(0.9 \pm 0.1)}{E} + (0.02 \pm 0.005)}. \tag{5}$$

This is well compatible with earlier detailed studies [26]. The constant term in addition to the square-root behaviour is mainly due to the non-uniformity of the response over the calorimeter surface. The energy response was found to be non-Gaussian which was taken into account in the unfolding procedure.

Using beams of identified electrons and pions, a precise separation of the RCal response to hadronic and electromagnetic particles has been obtained. This separation is quantified by a cut in the electromagnetic fraction of the cluster-energy which was placed at 0.6, as shown in Fig. 6.

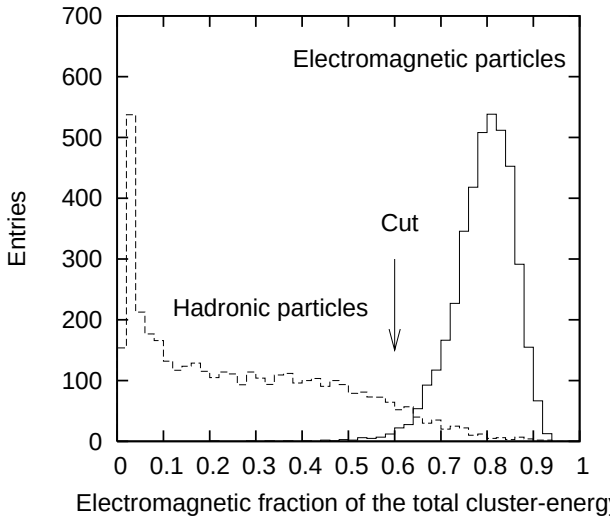

Figure 6: Electromagnetic and hadronic particle response (40 GeV pion and electron beam)

With this cut, the contamination from electromagnetic particles (mainly photons from π^0 decay) is negligible at all energies. The loss of hadrons due to the cut has been determined using identified beam particles at different momenta and also by matching identified tracks in the TPC

system and the corresponding calorimeter clusters in the region of common acceptance. It can be parametrized as:

$$\delta(\%) = \frac{51 \pm 5}{\sqrt{E}}. \tag{6}$$

The analysis of the calorimeter response required the development of an optimized cluster finding algorithm which fully exploits the analog response of the RCal cells. As the magnetic field suppresses low energy hadrons on the RCal fiducial surface, in most cases only single high energy protons or neutrons which may be accompanied by lower-energy K_L^0 or anti-neutrons, have to be accounted for. The cluster-finding algorithm thus first tries to find the largest cluster and verifies its shape-compatibility with the cluster model as obtained from calibration data. If needed, clusters are split further. Monte Carlo methods were used to estimate the effects of cluster overlap, demonstrating that this causes only small and well controllable systematic errors on the 2% level.

3.2.3 Energy resolution unfolding

A critical step in the analysis of the neutron data is the unfolding of the calorimeter resolution from the measured momentum distribution. With a starting estimate of the real neutron distribution as an input, a Monte Carlo simulation is used to predict the distribution modified by the calorimeter resolution. The difference between the real measurement and the Monte Carlo output is fed back to correct the input estimation. In a few steps, this iterative process results in a precise description of the raw neutral particle energy distribution. Due to the approximately linear behaviour of the measured spectrum as a function of x_F, the raw and the unfolded distributions are consistent with each other over most of the x_F range with the exception of the regions around x_F = 1 and x_F = 0.1. As the real neutron distribution is constrained to the physical region $x_F < 1$, the unphysical tail beyond the kinematic limit is removed. This is demonstrated in Fig. 7.

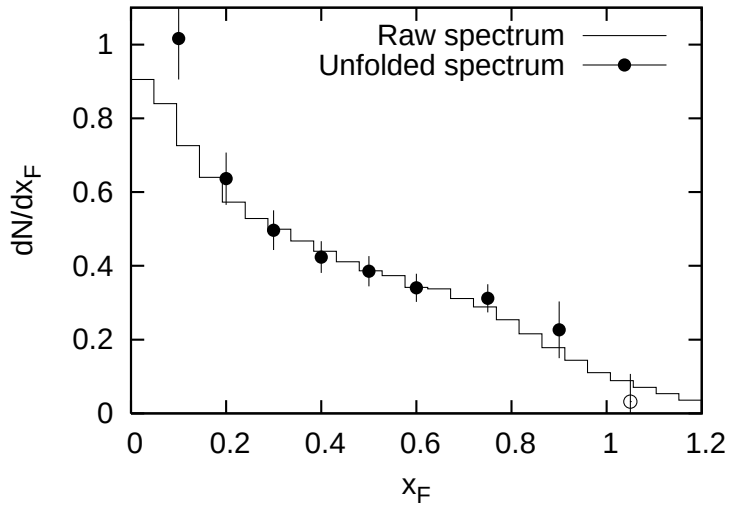

Figure 7: Raw measured energy distribution of neutrons compared with the unfolded neutron distribution. The increase of the latter at $x_F < 0.1$ is due to reduction in transverse acceptance. The open circle indicates the consistency of the unfolded spectra with zero beyond the kinematic limit

Indeed the unfolded spectrum is consistent with zero at x_F beyond 1 and the corrected distribution is increased over the measured one above $x_F \sim 0.7$ in accordance with the width of the RCal energy resolution.

3.2.4 Transformation to x_F and acceptance correction

In the absence of resolution in transverse momentum the transformation from the neutron energy as measured in the SPS lab system to the cms variable x_F introduces a spread in x_F which depends on the range in p_T and on the energy. This spread diverges with decreasing energy assuming a fixed p_T window. Taking however account of the transverse momentum cut-off at low energy shown in Fig. 1i, and limiting the p_T range to 2 GeV/c in the high energy region, this divergence is regularized such that the actual spread in x_F varies between 0.012 and 0.024 with the maximum value at x_F = 0.5. This spread is small compared to the bin width of 0.1 in x_F. The actual transformation was performed using Monte Carlo methods under the assumption that the p_T distribution of the neutrons would be equal to the one for protons. As shown in the later Sects. 11 and 12 of this paper this assumption has been verified experimentally. The resulting systematic errors are negligible.

The same assumption concerning the neutron p_T distribution has been made concerning the correction for the p_T cut-off at low x_F. Here the correction decreases rapidly from 20% at x_F = 0.1 to less than 1% at x_F = 0.3. Allowing for a 10% variation in surface of the assumed neutron p_T distribution beyond the experimental cut-off, this leads to the systematic error estimate of less than 2% given in Table 2.

4 Acceptance Coverage and Binning

The NA49 detector acceptance allows for the extraction of baryon yields over most of the forward cms hemisphere, with a welcome extension to negative x_F which may be used for a test of the experimental forward-backward symmetry.

The available event statistics limits the transverse momentum range to $p_T < 1.9$ GeV/c for protons and $p_T < 1.7$ GeV/c for anti- protons. The strong decrease of the anti-proton yield with increasing x_F defines a further limit at $x_F < 0.4$. For protons there is an acceptance gap at $x_F > 0.6$ and $p_T < 0.4$ GeV/c. This is a result of the interaction trigger: a small scintillation counter, S4 (see Fig. 2), vetoes non-interacting beam particles and, unavoidably, also events with charged secondaries in this region.

As described in Sect. 3 the granularity of the hadron calorimeter used for neutron detection does not allow for binning in transverse momentum. In addition the size of the fiducial region in the transverse plane progressively cuts off p_T values at below 2 GeV/c with decreasing x_F. This effect, together with the uncertainties of estimating the inseparable anti-neutron and K^0_L yields at low x_F, leads to a cutoff at x_F = 0.05 for neutrons.

The accessible kinematical regions for baryons described above were subdivided into bins in the x_F/p_T plane which vary according to the available particle yields. Effects of finite bin width are corrected for in the enumeration of the inclusive cross sections, see Sect. 6.

The resulting binning schemes are shown in Fig. 8.

For protons in the forward direction, the extended acceptance region using the tracking combination of GTPC and VPC is indicated by the thick line in Fig. 8a at $x_F \sim 0.6$. This procedure is cross-checked in the region of overlap with the main TPC tracking down to the second thick line at $x_F \sim 0.4$. As particle identification via energy loss measurement (dE/dx) does not operate in the region beyond x_F = 0.6, π/p and K^+/p ratios from other experiments have been used to extract the proton cross sections, see Sect. 5.4.

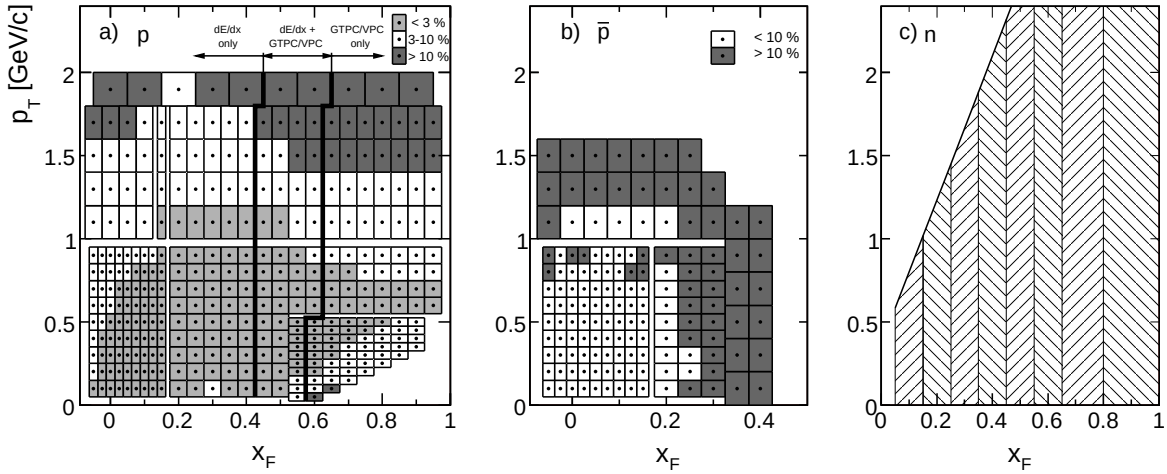

Figure 8: Binning scheme for a) protons, b) anti-protons and c) neutrons. In panels a) and b) the different regions of statistical uncertainty are indicated by different shades

5 Particle Identification

As compared to the preceding publication of pion production [1] the identification of charged particles using energy loss measurement in the TPC detector system has been further improved. In fact the extraction of pion yields by a four-parameter fit to the truncated dE/dx distribution of a track sample in a given bin, see [1], is insensitive to small imperfections of the analog response of the detectors. In addition it has been shown that the method used does not introduce additional fluctuations over and above the purely statistical error of the extracted pion sample.

This is not quite the case for the other particle species, especially for kaons and anti-protons which have generally small yields in relation to pions. Here the fit procedure introduces non-negligible additional fluctuations which are to be described by an error matrix with terms that create effective errors beyond the ones related to the particle yields proper. In this context it is mandatory to reduce the possible variation of the absolute position of the energy loss for the different particle species to a minimum in order to constrain the possible variations of the fit parameters.

5.1 Scaling of the truncated mean distributions

The distribution of truncated means as a function of $p/m = \beta\gamma$ shows non-linear deviations from the Bethe-Bloch parametrization which is formulated for the total ionization energy loss. It may be calculated using elementary photon absorption data [28] taking account of the effects of truncation using Monte Carlo methods. For the two gas mixtures used in the NA49 experiment (Ne+CO_2 91/9 and Ar+CH_4+CO_2 90/5/5) it has also been extracted experimentally by a careful re-analysis of all data. The resulting distributions show agreement on the sub-percent level as presented in Fig. 9.

The precision of the predictivity of the absolute energy deposit is exemplified in Fig. 10 on an extended scale by the ratio of the truncated means of protons and kaons to pions as a function of the lab momentum. The calibrated Bethe-Bloch references are superimposed as full lines.

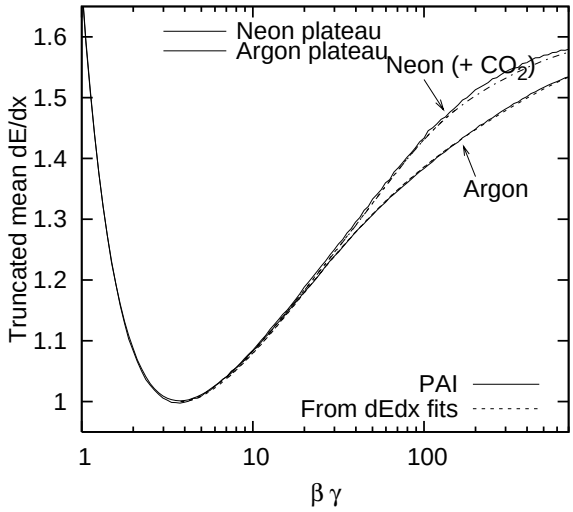

Figure 9: Truncated mean Bethe-Bloch functions for Ar+CH_4+CO_2 (90:5:5) and Ne+CO_2 (91:9) from the Photon Absorption Ionization (PAI) model and from direct dE/dx fits

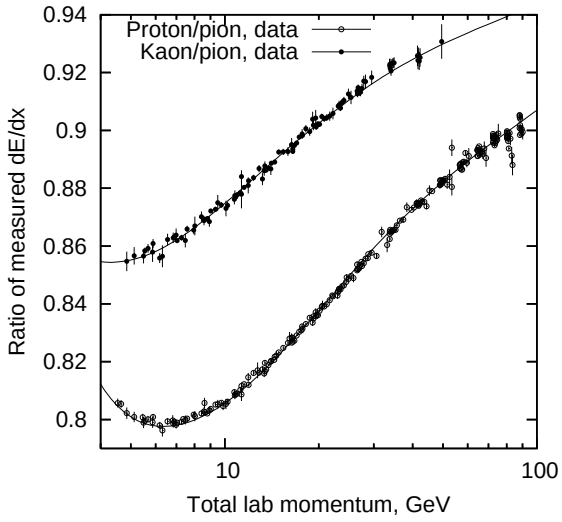

Figure 10: Ratios of the measured truncated mean dE/dx, protons and kaons relative to pions. The lines correspond to the calibrated Argon Bethe-Bloch curve, the data points are individual fits on the p+p data

5.2 Control of the analog detector response

A thorough re-analysis of the particle identification methods compared to the earlier work on pion extraction [1] has been performed. This concerns a re-calibration of time dependences, detector edge effects and the various corrections due to track length variations at the pad plane including the influence of $E \times B$ effects in the inhomogeneous magnetic fields. It results in an improvement of the predictivity of the mean dE/dx position relative to the Bethe-Bloch parametrization, in particular for kaons and baryons with respect to pions. An example is shown in Fig. 11 for the dE/dx shifts of pions, kaons and protons in a bin at x_F = 0.1, as a function of transverse momentum together with the variation of the relative width of the fitted dE/dx distribution.

It is evident that the local variation as well as the difference in energy deposit for the

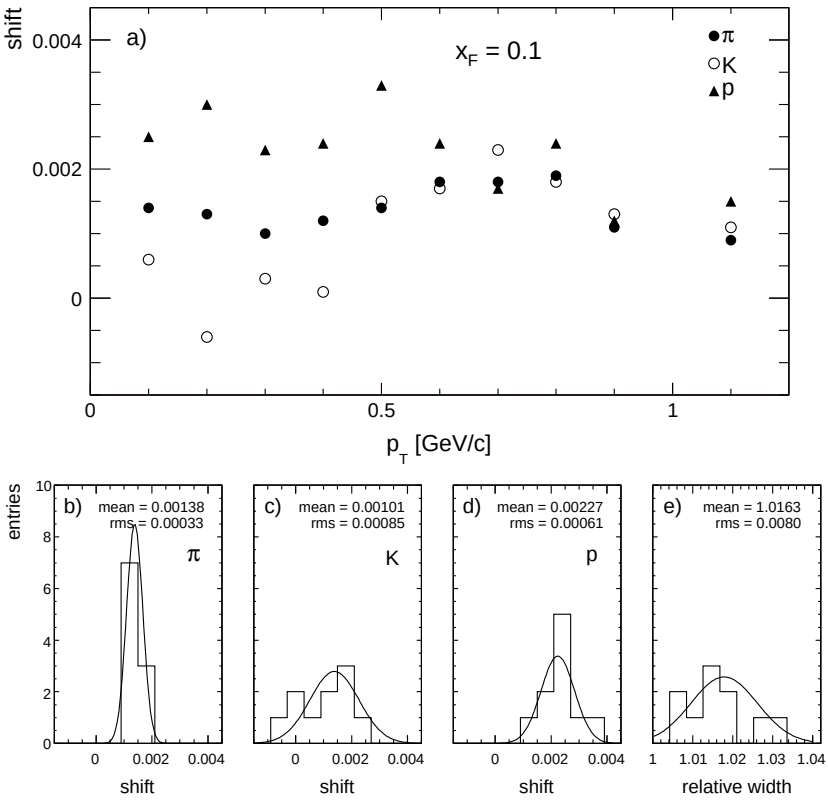

Figure 11: a) Mean dE/dx position relative to the Bethe-Bloch parametrization (shift) as a function of p_T at fixed x_F and distribution of b) π shift, c) K shift, d) p shift and e) relative width

different particle species stay at the permille level of absolute energy loss, and in the percent level for the width relative to the absolute prediction.

5.3 Error estimation

Particle identification proceeds, in each chosen bin of phase space, via a χ^2 optimization procedure between the measured truncated energy loss distribution and the sum of four single particle dE/dx distributions of known shape but a priori unknown positions and widths for electrons, pions, kaons and protons, respectively. Due to the small fraction of electrons and their position on the density plateau of the energy loss function, and due to the known dependence of the dE/dx resolution on the dE/dx value of each particle species [1], the problem reduces in practice to the determination of eight quantities: three positions, one width parameter and four yield parameters which correspond to the predicted number of particles. The statistical error of the four particle yields thus obtained may be determined from the dependence of χ^2 on all parameters (covariance matrix). It is to be noted that the inverse square root of the predicted numbers for each particle species is only a first approximation to the relative statistical error of the yields. The fluctuations of the fitted particle positions, Fig. 11, and their contributions to the error of the yield parameters are intercorrelated with the particle ratios and with the relative distances of the energy deposits in the dE/dx variable. The proper evaluation of the covariance matrix thus gives the effective statistical fluctuation of the yield parameters to be quoted as the experimental statistical error.

The method may be cross-checked using Monte Carlo methods by creating, in a given bin,

statistically independent samples using the yield parameters fitted to the experimental dE/dx distribution as input and allowing for their proper statistical fluctuation. Thus the assumption of a Gaussian parameter distribution used in the covariance matrix approach has been justified in particular also for phase space bins of small statistics or strongly correlated fit parameters.

It is interesting to compare the predicted relative statistical error of the yield parameters to the inverse square root of the fitted particle numbers. In case of "perfect" identification the two figures should be equal; the square of their ratio determines how much more statistics the real detector should collect in order to achieve the same precision as a "perfect" one. As an example in Table 1 the fitted yields, N, of pions, kaons and protons in one bin at x_F = 0.1 and p_T = 0.5 GeV/c are given together with the effective statistical error and the $1/\sqrt{N}$ value. The ratio of these two numbers is very close to one for the prevailing pion samples. In contrast it amounts to 1.44 and 1.23 for kaons and protons, respectively. For negative particles and in accordance with the inverted particle ratios, it is larger for anti-protons (1.4) than for negative kaons (1.25). Concerning the present work on proton and anti-proton cross sections the mean factors are, averaged over all phase space bins, about 1.1 for protons and 1.3 for anti-protons. The statistical errors given in the data tables, Sect. 7.1, correspond to the error evaluation described above.

	π^+	p	K^+	π^-	$\overline{p}$	K^-
number of entries N	28 388	6786	3088	20 851	1019	1917
$1/\sqrt{N}$ [%]	0.594	1.21	1.80	0.693	3.13	2.28
σ_{stat} [%]	0.605	1.50	2.60	0.701	4.38	2.80

Table 1: Yields and statistical errors for protons, kaons and pions at x_F = 0.1 and p_T = 0.5 GeV/c

Another, independent cross check of the validity of the evaluation of the statistical errors is given by the two dimensional interpolation of the final cross sections described in Sect. 7. As this interpolation reduces the local statistical uncertainty by a factor of between 3 and 4, the deviations of the data points from the interpolated value in each bin should measure the real point by point statistical fluctuation. In fact the compatibility of the distribution of the relative deviations shown in Fig. 19 with an rms of unity confirms the correctness of the error estimate given above.

5.4 Estimation of K^+ and π^+ contributions in the extreme forward direction

As the GTPC and VPC combination does not allow for particle identification via energy loss measurement, the proton extraction in the region $x_F > 0.6$, see in Fig. 8, has to rely on the measurement of π^+/p and K^+/p ratios from other experiments. In fact there are sufficient and mutually consistent data sets available to establish a reliable data base. The problem is alleviated by the fact that particle ratios are relatively stable against systematic errors of the different experiments and that their absolute values decrease rapidly to a few percent margin in the phase space region in question. The situation is shown in Fig. 12 in detail for π^+/p, K^+/p and (π^++K^+)/p for different x_F values as a function of transverse momentum. In both cases the ratios obtained by NA49 [1, 29] overlap consistently with the other data sets.

The interpolated lines shown in Fig. 12 have been used for the determination of proton cross sections from the total positive particle yields. The uncertainties connected with this procedure have been taken into account by an increase of the given statistical errors for the bins in question.

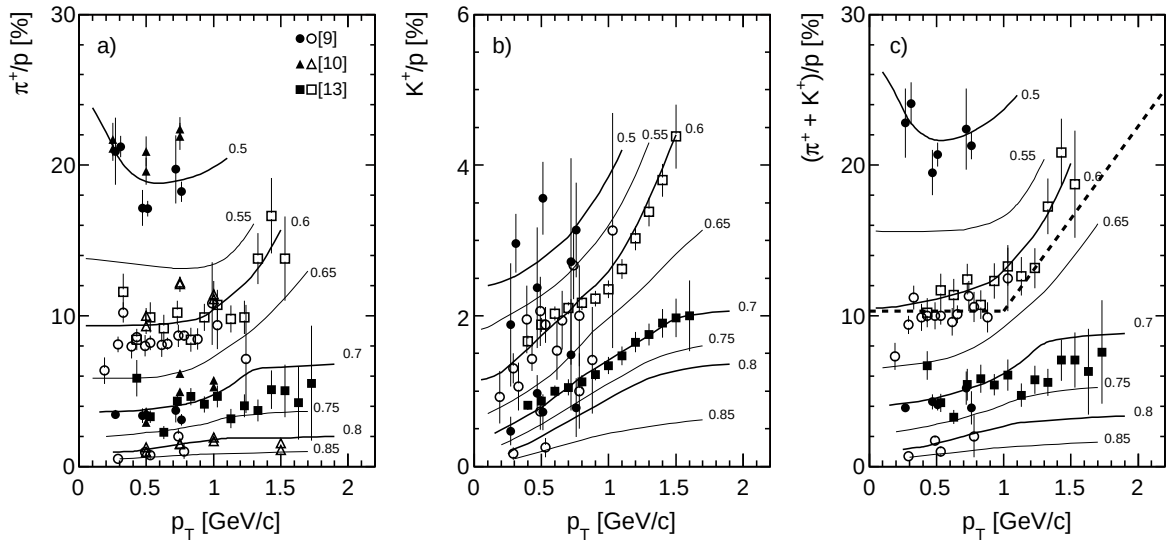

Figure 12: Ratios a) π^+/p, b) K^+/p and c) (π^++K^+)/p as a function of p_T in the forward direction. The x_F values are indicated in the figure. Below the thick dashed line in panel c) the tracking combination of GTPC and VPC was used

6 Evaluation of Invariant Cross Sections and Corrections

The experimental evaluation of the invariant cross section

$$f(x_F, p_T) = E(x_F, p_T) \cdot \frac{d^3\sigma}{dp^3}(x_F, p_T) \tag{7}$$

follows the methods described in [1]. The normalization and the corrections are discussed below, concentrating on those issues specific for baryon measurements.

6.1 Empty target correction

The empty target background is treated as a correction factor as described in [1] by determining the baryon yields in the full and empty target samples and establishing their normalized difference relative to the full target sample. The resulting correction factor is shown in Fig. 13.

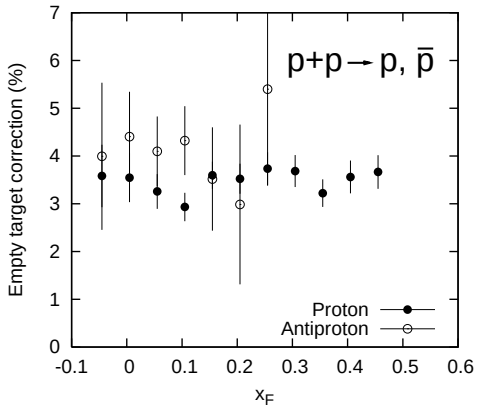

Figure 13: Empty target correction for protons and anti-protons (averaged over all p_T)

It is, within the statistical errors, p_T and x_F independent and is compatible with the one given for pions [1]. The correction for neutrons is equal to the one for protons.

6.2 Trigger bias correction

The interaction trigger uses a circular scintillator of 2 cm diameter placed at a distance of 4 m from the target in anti-coincidence (S4 counter in Fig. 2). It accepts 89% of the total inelastic cross section. The majority of the vetoed events contain one fast proton in the small S4 acceptance. As explained in detail in [1] this event loss creates an x_F and eventually p_T dependent bias for the extracted data which has to be carefully examined as it depends on short range and long range correlations in the hadronic final state.

This trigger bias is determined by an off-line increase of the S4 radius. With this method the limiting value of each measured cross section at zero radius may be obtained. The S4 radius increase is possible as all tracks in the corresponding momentum region are detected via the GTPC+VPC+RCal combination (Sect. 3).

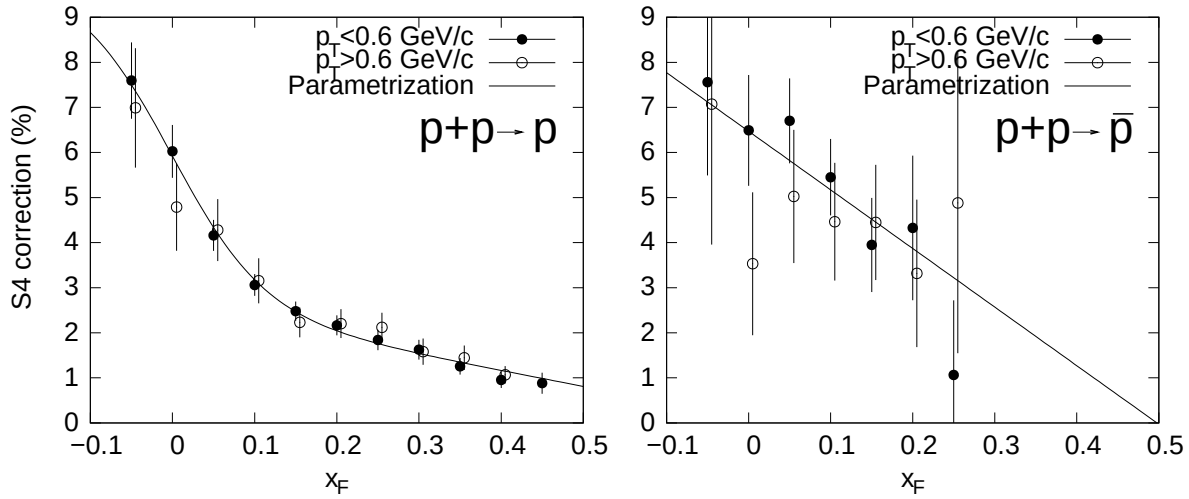

Figure 14: Trigger bias correction for protons (left) and anti-protons (right)

Figure 14 shows the size of the correction as a function of x_F for protons and anti-protons. The results for two p_T regions demonstrate that the correction is within errors independent of p_T. Anti-protons exhibit a different x_F dependence, again p_T independent within the (larger) statistical errors in this case. The correction varies from the one for pions in the forward hemisphere due to the different correlation between leading protons and secondary baryons in the projectile fragmentation. For neutrons, the trigger bias correction is equal to the one for protons.

6.3 Re-interaction and absorption

The re-interaction of baryons in the hydrogen target has been evaluated, as in the case of pions [1], using the PYTHIA event generator. The corresponding corrections are shown in Fig. 15.

The absorption of baryons by interaction with the detector material has been elaborated based on the results for pions, modifying the absorption length in accordance with the higher baryonic interaction cross section.

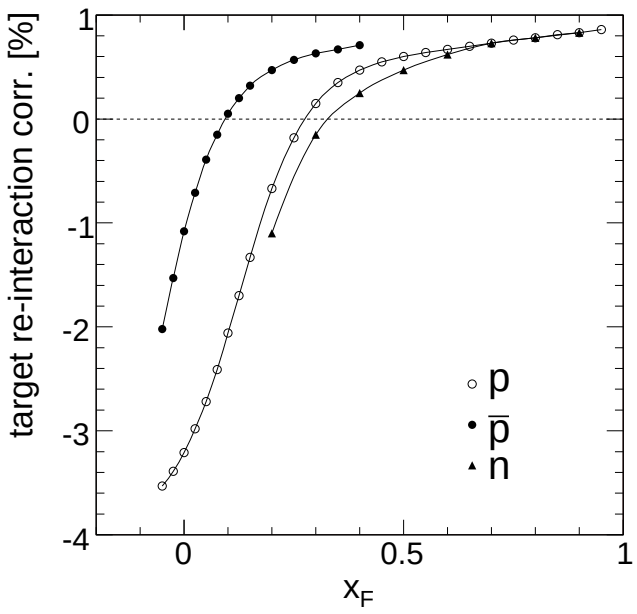

Figure 15: Target re-interaction correction

6.4 Feed-down from weak decays

The determination of the contribution from weakly decaying baryons (Λ, Σ and their anti-particles) is based on the methods discussed in [1]. The parent particle input distributions are taken from published data and a subsequent Monte Carlo simulation is used to estimate the on-vertex reconstruction efficiency for baryonic daughters.

As the decay baryons are close in mass to the parent hyperons, they take up most of the parent momentum. Their distribution over the measured phase space is therefore much wider than the one for decay pions and extends over the complete x_F and p_T ranges. As shown in Fig. 16 this correction amounts to up to 15% for protons and 20% for anti-protons with p_T dependences which are different for protons and anti-protons. For protons at large x_F, where the Σ^+ contribution dominates the feed-down, it even increases at large p_T.

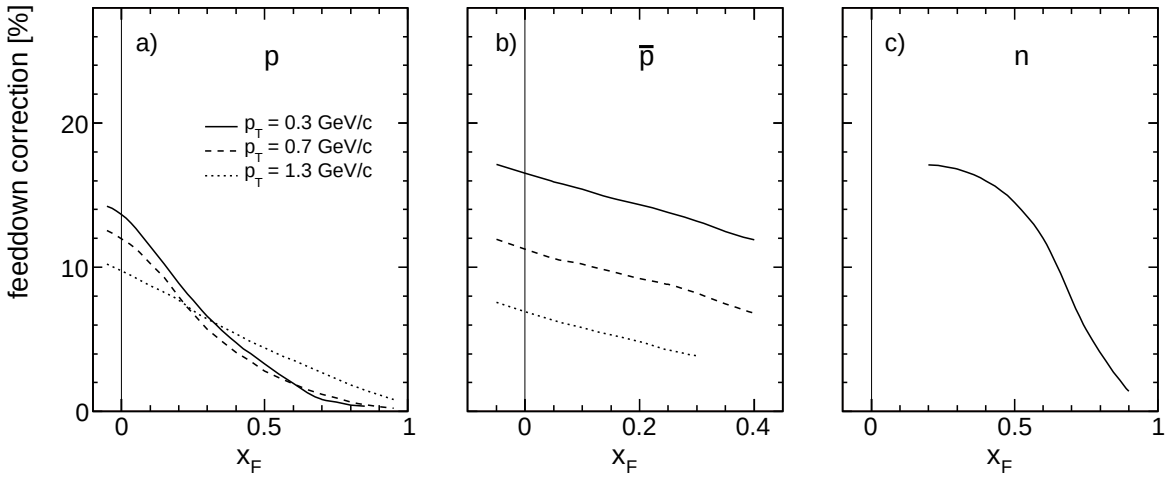

Figure 16: Relative size of the feed-down correction for a) protons, b) anti-protons and c) neutrons

The main systematic error source is the uncertainty of earlier measurements, especially for Σ^+. For anti-protons, besides the $\overline{\Lambda}$ also $\overline{\Sigma}^-$ contributes for which there are no existing measurements. The yield of this particle was estimated from general anti-baryon/ baryon ratio and isospin arguments. To first order it was assumed that the x_F and p_T shapes are the same as for $\overline{\Lambda}$, and that the $\overline{\Sigma}^-$ to Σ^+ ratio is 80% of the $\overline{\Lambda}/\Lambda$ ratio. For neutrons the feed-down correction corresponds to the full relative yield from Λ and Σ decays, as shown in Fig. 16c.

6.5 Binning correction

The effect of finite bin sizes on the extracted inclusive cross sections was discussed in detail in [1] and shown to depend on the second derivative of the x_F or p_T distributions. Due to the approximately linear rather than exponential x_F distribution of protons, the binning effects can in fact be neglected in longitudinal direction for the modest bin widths chosen. Also in transverse direction, due to the larger mean transverse momentum of baryons, the effect is smaller than for pions. As shown in Fig. 17 it reaches values in excess of 1% only at large p_T due to the bin width of 0.2 GeV/c in this region.

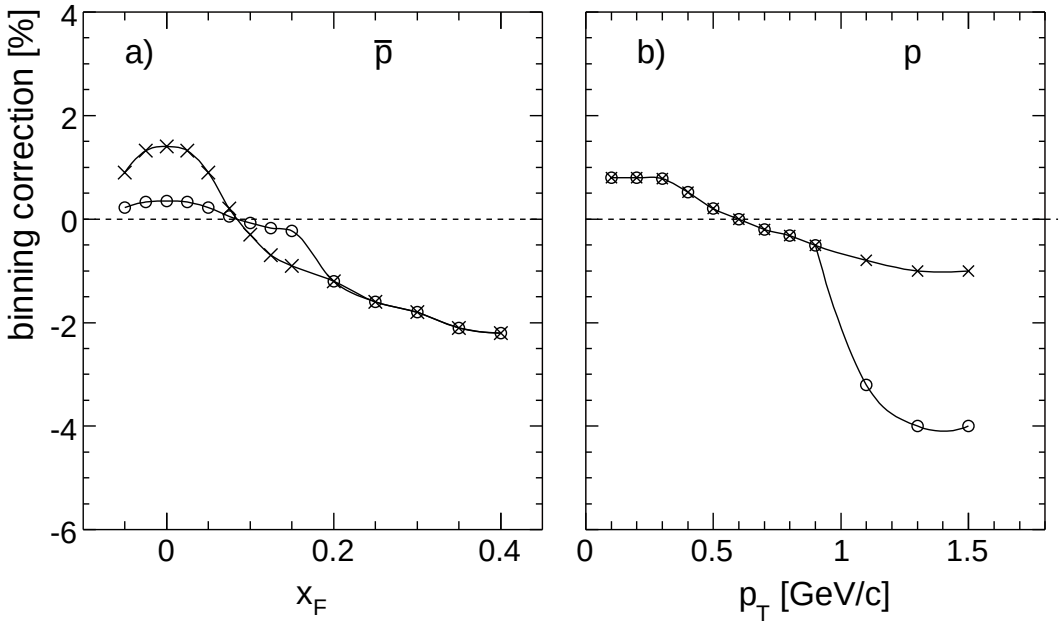

Figure 17: Correction due to the binning in a) x_F for $\overline{p}$ and b) p_T for p. The crosses represent the correction at fixed bin widths of Δx_F = 0.05 and Δp_T = 0.1 GeV/c, respectively, and the open circles describe the correction for the bins actually used

6.6 Systematic errors

The systematic errors of the extracted cross sections are given by the normalization procedure and the uncertainties of the applied corrections. These contributions are estimated in Table 2. They are governed by the fluctuation of the detector absorption, feed-down and trigger bias corrections which are shown in Fig. 18 over all phase space bins, for protons and anti-protons.

With a linear sum of 5.0% and 6.5%, respectively, for protons and anti-protons, and quadratic sums of 2.5% and 3.3% they are only slightly larger than the ones estimated for pion

	p	$\overline{\text{p}}$		n
Normalization	1.5%	1.5%	Normalization	1.5%
Tracking efficiency	0.5%	0.5%		
Trigger bias	0.5%	1.0%	Trigger bias	1%
Feed-down	1.5%	2.5%	Feed-down	3%
Detector absorption	0.5 – 1.5%	1.0%	Detector absorption	0.5 – 1.5%
Target re-interaction			Target re-interaction	
Binning correction			Binning correction	
			Acceptance	0 – 2%
			Energy scale error	4 – 8%
			Energy resolution unfolding	3 – 8%
			Charged veto efficiency	2 – 3%
			Cluster overlap	2%
			Hadron identification	2 – 5%
			K_L^0 contribution	0 – 3%
Total (upper limit)	5.0%	6.5%	Total (upper limit)	28%
Total (quadratic sum)	2.5%	3.3%	Total (quadratic sum)	10%

Table 2: Summary of systematic errors

production [1]. The larger systematic uncertainty of the neutron yields reflects the difficulties inherent in hadronic calorimetry as compared to charged track detection.

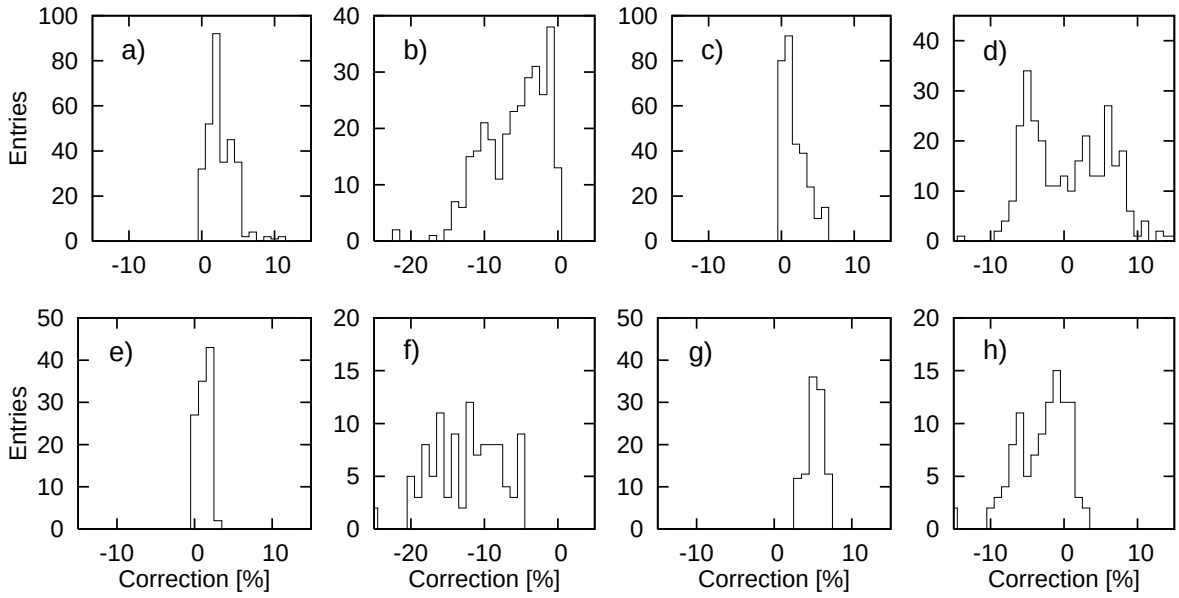

Figure 18: Distribution of corrections for protons (upper four panels) and anti-protons (lower four panels); a) and e) detector absorption, b) and f) feed-down, c) and g) trigger bias and d) and h) total

7 Results on double differential cross sections

7.1 Data tables

The binning scheme presented in Sect. 4 results in 333 and 143 data values for protons and anti-protons, respectively. These are presented in Tables 3 and 4.

$f(x_F, p_T), \Delta f$																		
$p_T \backslash x_F$	-0.05		-0.025		0.0		0.025		0.05		0.075		0.1		0.125		0.15	
0.1	2.349	2.76	2.161	1.90	2.121	1.78	2.128	1.75	2.224	1.69	2.340	1.76	2.620	1.83	3.039	1.55	3.479	1.76
0.2	2.158	3.53	1.921	1.60	1.837	1.46	1.854	1.42	1.901	1.44	2.095	1.49	2.349	1.50	2.666	1.36	2.998	1.49
0.3	1.664	3.72	1.570	2.63	1.631	1.81	1.575	1.41	1.664	1.26	1.750	1.31	1.935	1.33	2.179	1.34	2.549	1.28
0.4	1.297	4.24	1.286	2.74	1.287	2.26	1.238	1.71	1.334	1.37	1.379	1.43	1.486	1.52	1.742	1.49	1.880	1.52
0.5	1.094	3.96	0.951	3.25	0.977	2.45	0.929	1.98	0.973	1.47	1.057	1.45	1.161	1.52	1.224	1.56	1.353	1.72
0.6	0.707	4.38	0.689	3.62	0.645	3.24	0.688	2.46	0.712	1.98	0.709	1.78	0.807	1.67	0.884	1.74	0.948	1.91
0.7	0.493	5.38	0.451	4.31	0.449	4.07	0.494	2.76	0.482	2.47	0.533	2.15	0.526	1.93	0.601	1.78	0.654	2.11
0.8	0.378	6.13	0.357	5.10	0.314	4.45	0.322	3.52	0.329	3.19	0.3386	2.95	0.3686	2.42	0.3984	2.42	0.430	2.48
0.9	0.244	6.33	0.203	6.38	0.233	5.44	0.2196	4.49	0.2274	3.90	0.2399	3.46	0.2572	3.19	0.2503	3.33	0.2694	2.71
1.1	0.0956	4.75			0.0899	4.28			0.0927	3.14			0.0988	2.76			0.1078	2.42
1.3	0.0445	7.71			0.0366	6.10			0.0384	4.67			0.0410	4.15			0.0398	3.64
1.5	0.0199	9.72			0.0173	8.74			0.0188	6.90			0.0161	6.48			0.0163	6.46
1.7	0.0087	14.2			0.00640	13.4			0.00617	11.3			0.00705	9.45			0.00607	9.60
1.9					0.00284	14.3							0.00296	10.3				
$p_T \backslash x_F$	0.2		0.25		0.3		0.35		0.4		0.45		0.5		0.55		0.6	
0.05															17.1	7.46	16.8	14.6
0.1	4.654	1.53	5.71	1.83	6.64	3.44	7.749	1.28	8.92	1.58	10.02	1.57	11.68	1.65	14.38	4.31	15.07	6.53
0.15															13.64	3.21	13.67	4.24
0.2	4.086	1.24	5.132	1.44	6.10	2.54	6.958	0.96	7.500	1.21	8.52	1.22	9.59	1.24	11.92	2.96	12.80	2.94
0.25															9.95	2.37	11.55	2.76
0.3	3.265	1.18	4.231	1.63	5.016	1.70	5.876	0.83	6.261	1.08	6.766	1.14	7.232	1.16	8.78	2.30	9.61	2.25
0.35															7.30	2.34	7.67	2.33
0.4	2.518	1.29	3.145	1.74	3.904	1.87	4.561	0.89	4.863	1.06	5.098	1.10	5.350	1.14	6.09	2.06	6.21	2.11
0.45															4.84	2.19	5.03	2.21
0.5	1.815	1.28	2.292	1.58	2.783	1.57	3.341	0.93	3.609	1.08	3.772	1.17	3.781	1.21	3.908	2.31	3.938	2.36
0.6	1.247	1.43	1.516	1.96	1.957	2.27	2.224	1.10	2.544	1.18	2.628	1.31	2.649	1.34	2.709	1.80	2.738	1.84
0.7	0.798	1.65	0.989	2.09	1.252	2.01	1.489	1.32	1.652	1.35	1.771	1.40	1.753	1.53	1.741	2.08	1.692	2.17
0.8	0.5092	1.71	0.620	1.94	0.756	2.35	0.894	1.59	1.021	1.61	1.140	1.61	1.127	1.71	1.128	2.43	1.028	2.61
0.9	0.3201	2.08	0.3672	2.38	0.458	2.63	0.548	1.92	0.605	1.94	0.676	1.97	0.689	2.11	0.672	2.91	0.614	3.12
1.1	0.1197	2.26	0.1388	2.42	0.1535	2.83	0.1657	2.22	0.1970	2.14	0.2071	2.25	0.2172	2.29	0.2124	3.43	0.1944	3.67
1.3	0.0439	3.72	0.0485	3.71	0.0527	4.54	0.0584	3.48	0.0587	3.63	0.0602	3.78	0.0629	3.94	0.0590	6.28	0.0567	6.57
1.5	0.0176	5.77	0.0156	6.43	0.0177	8.02	0.0207	5.42	0.0187	6.07	0.0182	6.38	0.0165	7.05	0.0153	11.4	0.0142	12.1
1.7	0.00578	8.75	0.00614	8.95	0.00628	9.37	0.00653	9.44	0.00709	9.45	0.00592	10.3	0.00549	17.8	0.0059	17.5	0.00235	27.6
1.9	0.00313	7.98			0.00245	10.6			0.00242	10.8			0.00161	21.2			0.00082	29.4
$p_T \backslash x_F$	0.65		0.7		0.75		0.8		0.85		0.9		0.95					
0.05																		
0.1	18.5	10.1																
0.15	14.09	5.64	14.0	9.72														
0.2	12.68	3.88	14.74	4.94	15.0	8.35												
0.25	11.26	3.20	11.75	3.70	14.9	7.49	10.61	9.23										
0.3	9.74	2.83	10.86	3.06	9.76	5.11	10.00	8.62	12.5	8.11								
0.35	8.09	2.34	7.34	3.09	7.93	3.42	8.48	4.52	10.18	4.94	12.39	7.76						
0.4	6.55	2.42	6.19	2.58	6.47	3.53	6.46	3.67	7.71	4.64	9.00	5.07						
0.45	5.13	2.24	5.03	2.70	4.93	2.82	5.08	3.20	5.43	3.91	6.78	4.80						
0.5	4.028	2.41	3.930	2.52	3.752	2.65	4.05	2.63	3.55	3.36	4.98	3.21						
0.6	2.592	1.95	2.507	2.04	2.322	2.18	2.247	2.28	2.238	2.35	2.464	2.28	4.954	1.81				
0.7	1.619	2.28	1.581	2.38	1.436	2.57	1.288	2.78	1.278	2.86	1.324	2.87	2.339	2.20				
0.8	0.984	2.75	0.973	2.84	0.886	3.06	0.768	3.35	0.686	3.66	0.711	3.68	1.130	2.97				
0.9	0.609	3.22	0.557	3.45	0.506	3.72	0.455	4.05	0.396	4.44	0.368	4.74	0.544	3.97				
1.1	0.1942	3.77	0.1757	4.07	0.1618	4.36	0.1334	4.92	0.1338	5.05	0.1185	5.50	0.1292	5.42				
1.3	0.0442	7.55	0.0392	8.24	0.0463	7.87	0.0350	9.24	0.0364	9.32	0.0404	9.08	0.0447	8.89				
1.5	0.0147	12.3	0.0136	13.0	0.0109	14.9	0.0084	17.4	0.0108	15.9	0.0131	14.8	0.0147	14.3				
1.7	0.00437	20.9	0.00421	22.1	0.00295	26.1	0.0045	22.4	0.00293	28.0	0.00379	25.9	0.0051	23.0				
1.9			0.00076	32.3			0.00119	28.4			0.00083	36.1						

Table 3: Invariant cross section, $f(x_F, p_T)$, in mb/(GeV^2/c^3) for protons in p+p collisions at 158 GeV/c beam momentum. The relative statistical errors, Δf, are given in %

$f(x_F, p_T), \Delta f$														
$p_T \backslash x_F$	-0.05		-0.025		0.0		0.025		0.05		0.075		0.1	
0.1	0.563	6.71	0.590	4.28	0.581	3.66	0.545	3.67	0.499	3.87	0.489	4.24	0.391	4.52
0.2	0.508	6.15	0.505	3.55	0.509	2.98	0.518	2.92	0.473	3.12	0.405	3.69	0.379	4.04
0.3	0.391	6.75	0.450	5.52	0.450	3.88	0.404	2.99	0.401	2.79	0.353	3.12	0.320	3.56
0.4	0.287	7.61	0.338	6.23	0.324	4.90	0.311	3.61	0.2848	3.17	0.2918	3.38	0.237	4.38
0.5	0.222	8.16	0.260	6.77	0.230	5.48	0.262	4.31	0.2324	3.22	0.2031	3.52	0.1761	4.38
0.6	0.163	8.52	0.178	8.99	0.178	6.67	0.1587	5.37	0.1511	4.82	0.1211	4.82	0.1255	4.72
0.7	0.117	9.82	0.103	10.4	0.1102	8.17	0.1168	6.29	0.1141	5.46	0.0929	5.56	0.0830	4.71
0.8	0.0534	15.7	0.0862	9.83	0.0845	8.84	0.0773	7.93	0.0637	7.22	0.0614	7.24	0.0600	6.58
0.9	0.0432	15.5	0.0427	13.9	0.0481	12.2	0.0409	10.7	0.0385	9.07	0.0441	8.11	0.0363	8.59
1.1	0.0155	12.3			0.0194	8.12			0.0153	7.39			0.0142	7.32
1.3	0.0095	14.7			0.00532	16.9			0.00515	13.3			0.00521	12.6
1.5	0.00272	27.1			0.00258	23.8			0.00241	20.2			0.00179	21.4
$p_T \backslash x_F$	0.125		0.15		0.2		0.25		0.3		0.35		0.4	
0.1	0.355	4.98	0.260	7.36	0.194	7.09	0.115	11.5	0.074	18.1	0.0418	18.9	0.0173	55.1
0.2	0.300	4.49	0.275	5.57	0.183	7.15	0.0900	9.63	0.0613	14.4				
0.3	0.255	4.53	0.199	5.84	0.1654	4.69	0.0941	8.96	0.0429	14.7	0.0270	13.8	0.0137	29.5
0.4	0.203	4.98	0.165	6.14	0.1154	7.52	0.0645	10.5	0.0425	12.5				
0.5	0.1350	5.55	0.1231	5.73	0.0860	5.76	0.0463	10.3	0.0266	13.9	0.0161	13.6	0.0082	25.9
0.6	0.1005	6.69	0.0787	6.64	0.0578	8.62	0.0427	8.40	0.0190	14.9				
0.7	0.0705	5.72	0.0596	8.66	0.0443	9.05	0.0191	14.2	0.0162	14.7	0.0092	16.4	0.0062	21.8
0.8	0.0382	9.29	0.0346	10.8	0.0235	8.27	0.0151	14.8	0.0132	15.0				
0.9	0.0275	10.9	0.0242	10.0	0.0190	11.5	0.0141	11.7	0.0061	21.7	0.00435	20.6	0.00189	38.0
1.1			0.01008	9.15	0.00796	8.63	0.00447	16.1	0.00230	22.1	0.00182	27.0	0.00073	54.0
1.3			0.00403	15.5	0.00255	15.2	0.00152	21.7	0.00128	27.1				
1.5			0.00127	22.8	0.00068	30.4	0.00057	34.5						

Table 4: Invariant cross section, $f(x_F, p_T)$, in mb/(GeV^2/c^3) for anti-protons in p+p collisions at 158 GeV/c beam momentum. The relative statistical errors, Δf, are given in %

7.2 Extension of the data to high $\mathbf{x_F}$ and low $\mathbf{p_T}$

As shown in Sect. 3 the NA49 detector acceptance is limited at large x_F and low p_T by the necessity of using an interaction trigger, vetoing through-going beam tracks. The corresponding acceptance gap extends from $p_T < 0.05$ at $x_F = 0.65$ to $p_T < 0.6$ at $x_F = 0.95$, see Fig. 1. In order to maintain the possibility of precise p_T integration in this phase space region it is mandatory to use data from other experiments to supplement the NA49 results. Fortunately there are data from seven different experiments, all conducted at Fermilab in the years 1973 to 1982 [3–9] in exactly this region which also partially overlap with the NA49 data. These data come from internal target [3–6] and bubble chamber experiments [7, 8], all performed in the target region at low proton lab momenta, and from a spectrometer experiment [9] in the forward hemisphere. If applicable the data have been transformed from the coordinate pair momentum transfer t and missing mass into the p_T and x_F coordinates, interpolated to the x_F values defined by the NA49 binning scheme and corrected for s-dependence. This latter correction will be quantified in section 10 below. In total 123 data points are thus available as given in Table 5.

The data are well consistent within their statistical errors, both between the different experiments and with the NA49 results in the overlap region. The only exception is given by the bubble chamber experiment [8] where at x_F below 0.9 the cross sections deviate from all other experiments by +20% to +30% independent of p_T. This difference cannot be understood by eventual mis-identification nor by binning effects. Data from [8] are therefore only used at $x_F \geq 0.9$.

7.3 Interpolation scheme

As in the preceding publications concerning pions [1, 30] a two-dimensional interpolation is applied to the data which reduces the local statistical fluctuations given by the errors of

p_T	f	Δf	ref	p_T	f	Δf	ref	p_T	f	Δf	ref	p_T	f	Δf	ref	p_T	f	Δf	ref
x_F = 0.6				x_F = 0.65				x_F = 0.7				x_F = 0.75				x_F = 0.8			
0.224	14.10	15.0	7	0.224	15.30	15.0	7	0.224	16.60	15.0	7	0.224	16.90	15.0	7	0.478	4.70	2.0	3
0.381	5.89	15.0	7	0.381	6.46	15.0	7	0.381	6.56	15.0	7	0.381	6.94	15.0	7	0.570	2.70	2.0	3
0.540	3.61	15.0	7	0.540	3.80	15.0	7	0.540	3.89	15.0	7	0.540	3.71	15.0	7				
0.707	1.35	15.0	7	0.707	1.23	15.0	7	0.707	1.25	15.0	7	0.707	1.24	15.0	7	0.224	16.20	15.0	7
																0.381	7.41	15.0	7
0.200	13.34	3.3	9					0.300	10.45	2.0	9					0.540	3.52	15.0	7
0.300	9.43	2.0	9					0.500	4.04	2.4	9					0.707	1.14	15.0	7
0.400	6.31	2.6	9					0.750	1.32	4.4	9								
0.500	4.14	2.3	9					0.500	4.06	1.0	9					0.300	11.67	1.4	9
0.625	2.42	2.7	9					0.750	1.26	1.6	9					0.500	4.10	1.5	9
0.750	1.41	3.3	9													0.750	1.00	2.9	9
0.300	8.82	5.4	9													0.500	3.90	1.3	9
0.400	5.93	1.0	9													0.750	1.00	2.0	9
0.500	4.03	1.6	9																
0.625	2.40	1.2	9																
0.750	1.41	1.0	9																
x_F = 0.85				x_F = 0.9				x_F = 0.95				x_F = 0.975							
0.511	4.18	2.0	3	0.537	3.91	2.0	3	0.182	34.10	5.0	4	0.188	44.51	5.0	4				
0.602	2.33	2.0	3	0.629	2.12	2.0	3	0.246	23.35	5.0	4	0.253	31.24	5.0	4				
								0.299	21.15	5.0	4	0.302	30.31	5.0	4				
0.190	20.83	5.0	4	0.157	28.41	5.0	4	0.337	18.94	5.0	4	0.344	28.09	5.0	4				
0.245	16.73	5.0	4	0.225	20.83	5.0	4	0.375	14.52	5.0	4	0.384	21.79	5.0	4				
0.290	15.47	5.0	4	0.275	17.68	5.0	4	0.409	12.15	5.0	4	0.416	20.20	5.0	4				
0.328	12.00	5.0	4	0.318	16.10	5.0	4												
0.363	9.63	5.0	4	0.355	12.31	5.0	4	0.224	33.30	15.0	7	0.224	53.20	15.0	7				
				0.389	10.10	5.0	4	0.381	14.44	15.0	7	0.381	25.18	15.0	7				
0.224	17.20	15.0	7					0.540	6.84	15.0	7	0.540	12.16	15.0	7				
0.381	7.80	15.0	7	0.224	21.40	15.0	7	0.707	1.60	15.0	7	0.707	3.14	15.0	7				
0.540	3.32	15.0	7	0.381	9.12	15.0	7												
0.707	1.05	15.0	7	0.540	3.52	15.0	7	0.179	43.10	2.0	5	0.186	69.80	2.0	5				
				0.707	1.06	15.0	7	0.263	24.20	2.0	5	0.269	41.30	2.0	5				
0.210	16.70	5.0	5					0.350	17.90	2.0	5	0.357	30.20	2.0	5				
0.302	11.80	5.0	5	0.154	29.50	6.0	5	0.430	11.00	2.0	5	0.438	19.70	2.0	5				
0.384	7.47	5.0	5	0.244	17.70	6.0	5												
				0.330	12.80	4.0	5	0.110	41.30	5.9	6	0.119	58.20	5.0	6				
				0.410	7.87	4.0	5	0.212	30.20	5.8	6	0.220	49.10	4.0	6				
				0.190	25.70	4.0	6	0.160	46.23	15.0	8	0.160	67.60	15.0	8				
								0.316	19.50	15.0	8	0.316	42.65	15.0	8				
				0.160	29.17	15.0	8	0.447	10.07	15.0	8	0.447	14.79	15.0	8				
				0.316	14.96	15.0	8	0.548	7.24	15.0	8	0.548	10.47	15.0	8				
				0.447	7.32	15.0	8	0.632	4.07	15.0	8	0.632	6.03	15.0	8				
				0.548	5.01	15.0	8												
				0.632	2.72	15.0	8												
				0.500	4.55	1.1	9												
				0.750	1.01	1.0	9												

Table 5: Invariant cross section in mb/(GeV^2/c^3) for protons at very forward region ($x_F \geq 0.6$) in p+p collisions measured by [3–9]

the data points by a factor of 3-4. As there is no possibility to describe the detailed x_F and p_T distributions by simple functions and as any algebraic approximation risks to dilute the data quality by introducing systematic biases, the interpolation scheme relies on a multi-step recursive method using eyeball fits. The quality of this procedure may be controlled by plotting the differences between data points and interpolation, normalized to the statistical errors. The resulting distribution should be a Gaussian centered at zero with variance unity. This is demonstrated in Fig. 19 for protons and anti-protons as far as the NA49 data points are concerned, and separately for the extension to higher x_F at low p_T described above.

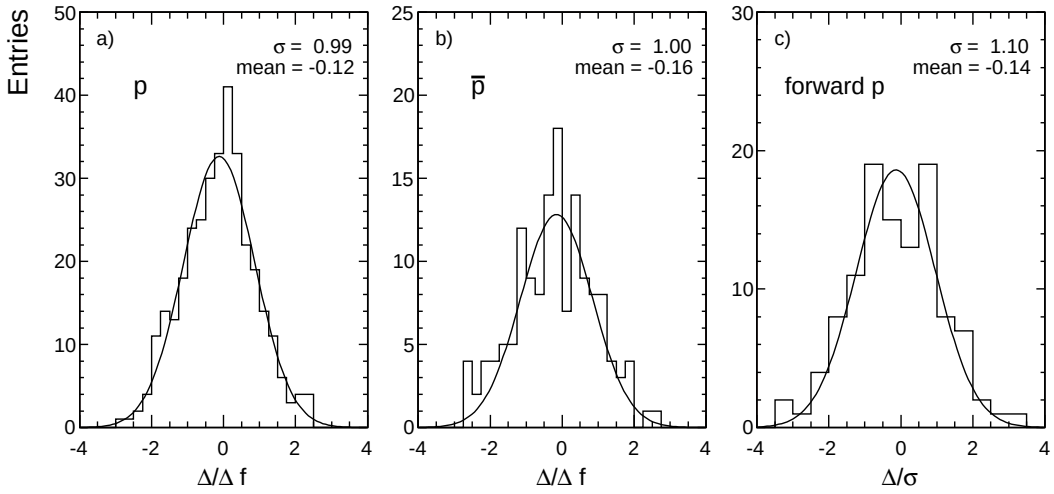

Figure 19: Normalized difference plots between data and interpolation for a) protons, b) anti-protons and c) protons at high x_F

As, in this latter region, there are practically no measurements below p_T = 0.2-0.3 GeV/c the extrapolation to p_T = 0 has to be independently quantified. In this limited range of transverse momentum and at $x_F > 0.6$ a parametrization of the form

$$f = Ae^{-b|t|}, \tag{8}$$

with $p_T^2 \sim |t|x_F$ has been applied. The parameters A and b are shown in Fig. 20 as a function of x_F.

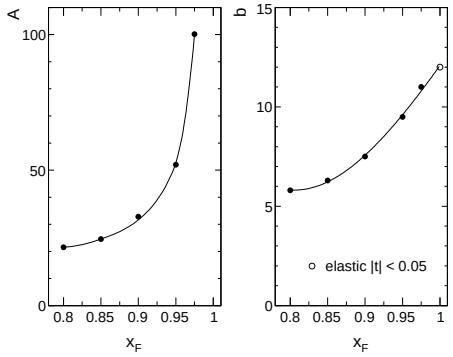

Figure 20: Parameters A and b as a function of x_F

The slope b extrapolates well to the value for low-t elastic scattering at SPS energy also shown in Fig. 20

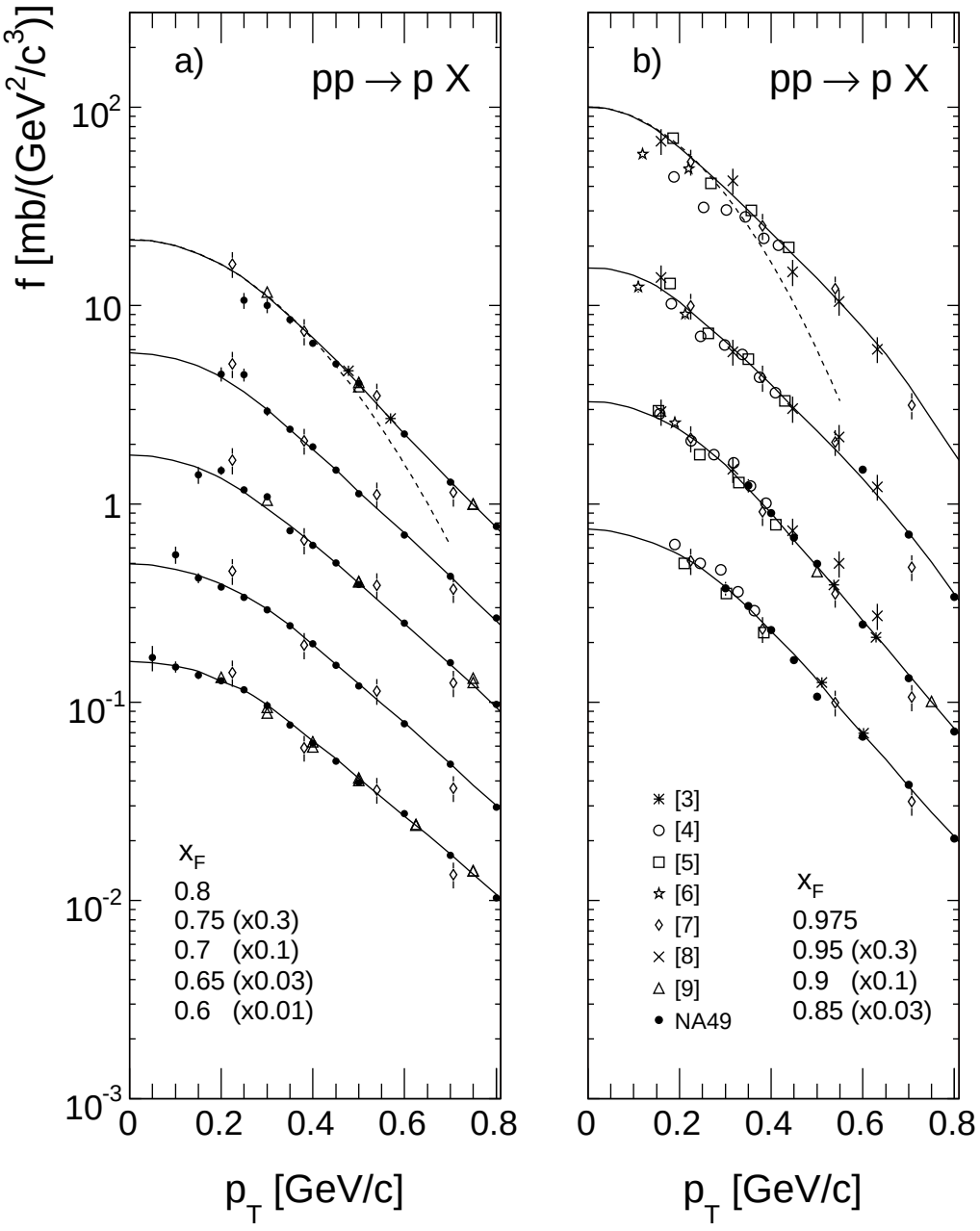

Figure 21: Invariant cross section as function of p_T at fixed x_F taken from [3–9] and NA49. The full lines represent the data interpolation, the dashed lines the exponential parametrization [8]

The internal consistency of the data sets used and their compatibility with the interpolation scheme as well as with the extrapolation to very low p_T is presented in Fig. 21.

It should be noted that the measured cross sections deviate rapidly from the low-t parametrization, Eq. 8, already at p_T values of $\sim$0.4 GeV/c. This is exemplified by the dashed lines in Fig. 21 for two x_F values. Fits over larger regions of p_T^2 therefore result systematically in smaller values of b [8], see also the discussion in Sect. 12.

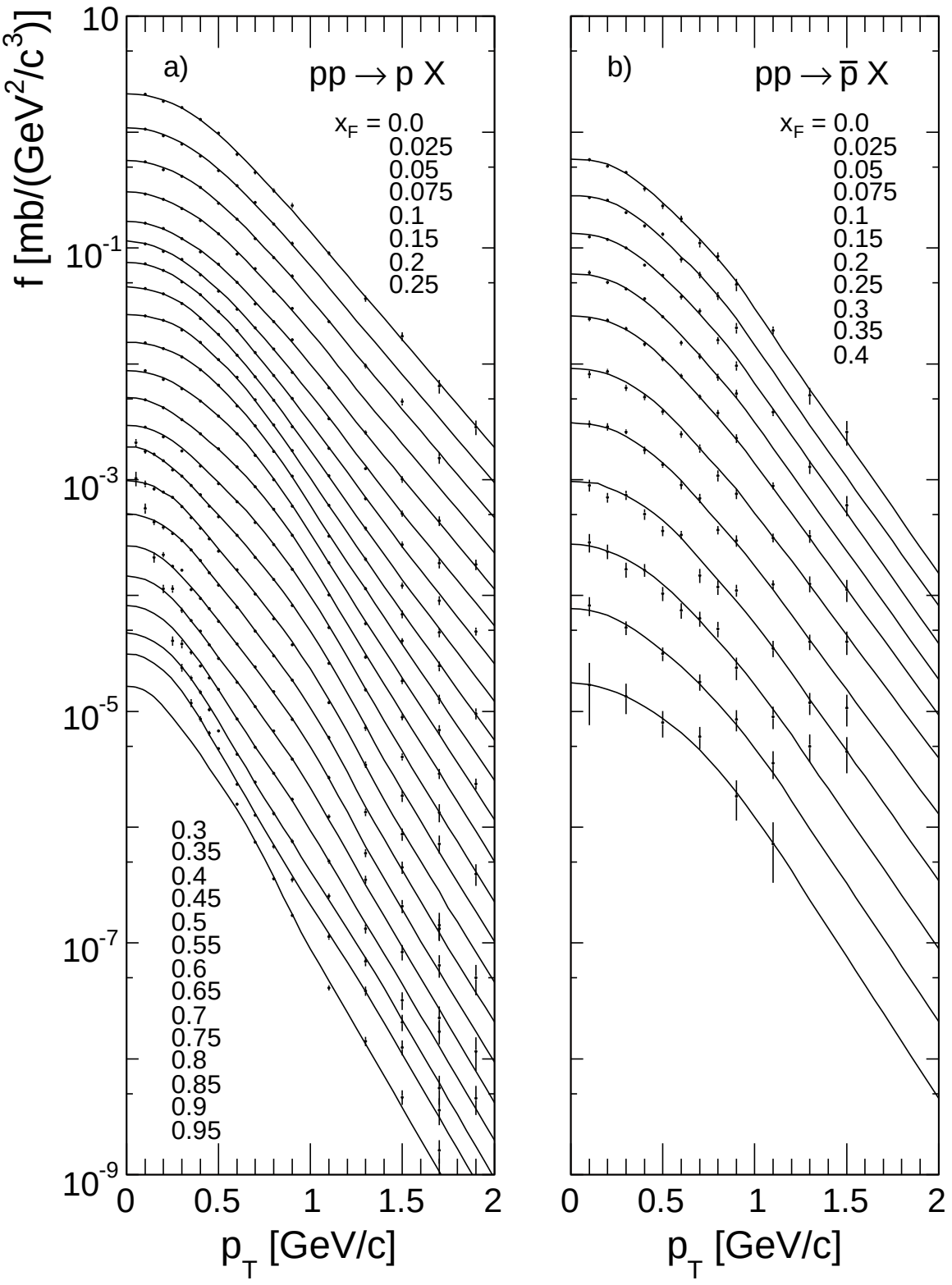

Figure 22: Double differential invariant cross section $f(x_F, p_T)$ [mb/(GeV^2/c^3)] as a function of p_T at fixed x_F for a) protons and b) anti-protons produced in p+p collisions at 158 GeV/c beam momentum. The distributions for different x_F values are successively scaled down by 0.5 for better separation

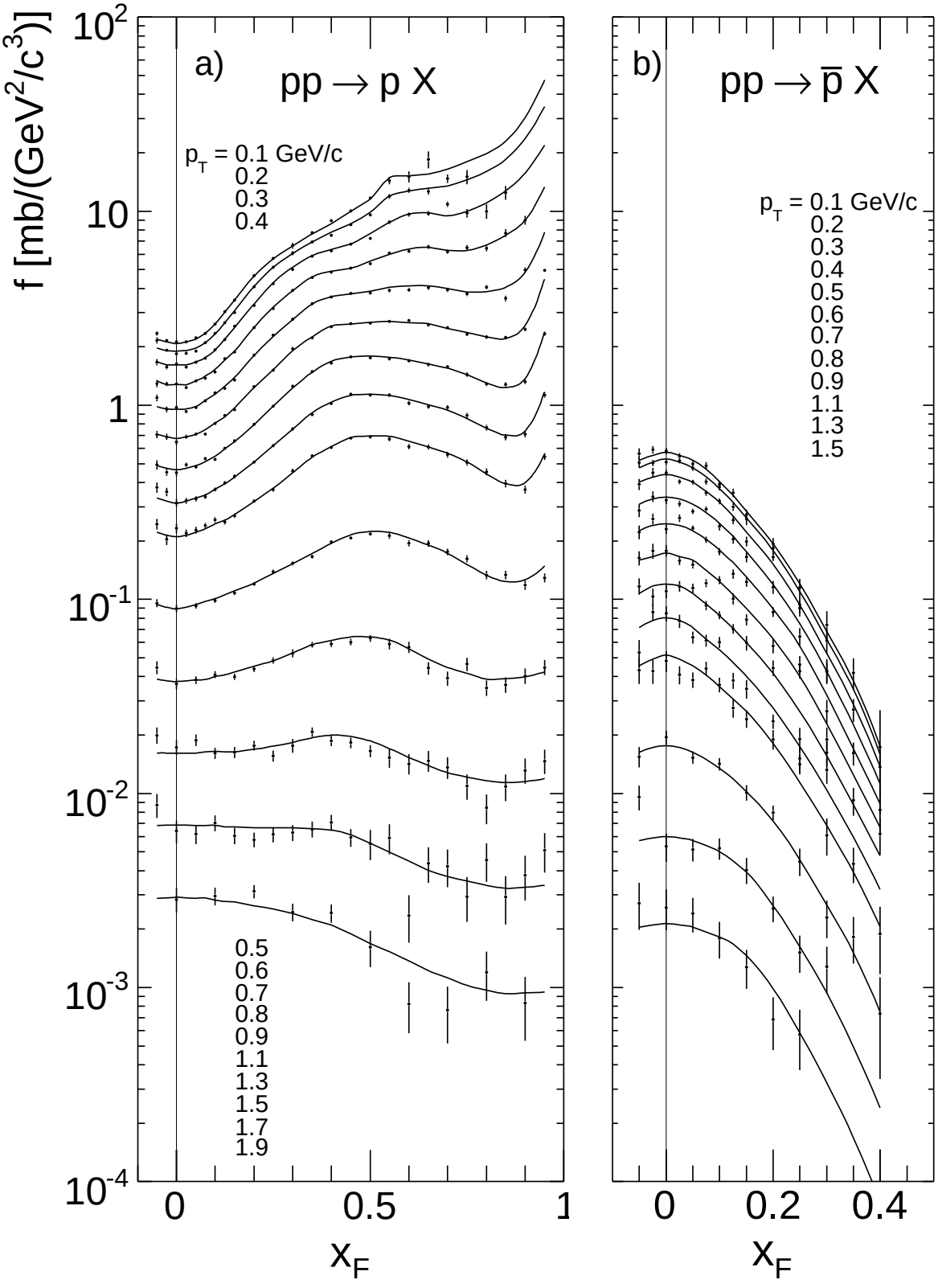

Figure 23: Double differential invariant cross section $f(x_F, p_T)$ [mb/(GeV^2/c^3)] as a function of x_F at fixed p_T for a) protons and b) anti-protons produced in p+p collisions at 158 GeV/c beam momentum

7.4 Dependence of the invariant cross sections on p_T and x_F

The shape of the invariant cross section as functions of p_T and x_F is shown in Figs. 22 and 23. These Figures include the data interpolation discussed above. In order to clearly demonstrate the shape evolution and to avoid the overlap of the interpolated curves and of the error bars, subsequent p_T distributions have been multiplied by factors of 0.5 (Fig. 22).

7.5 $\overline{p}$/p ratios

The phase space distributions of protons and anti-protons are rather similar in transverse momentum, Fig. 22, but they show important differences in longitudinal momentum, Fig. 23.

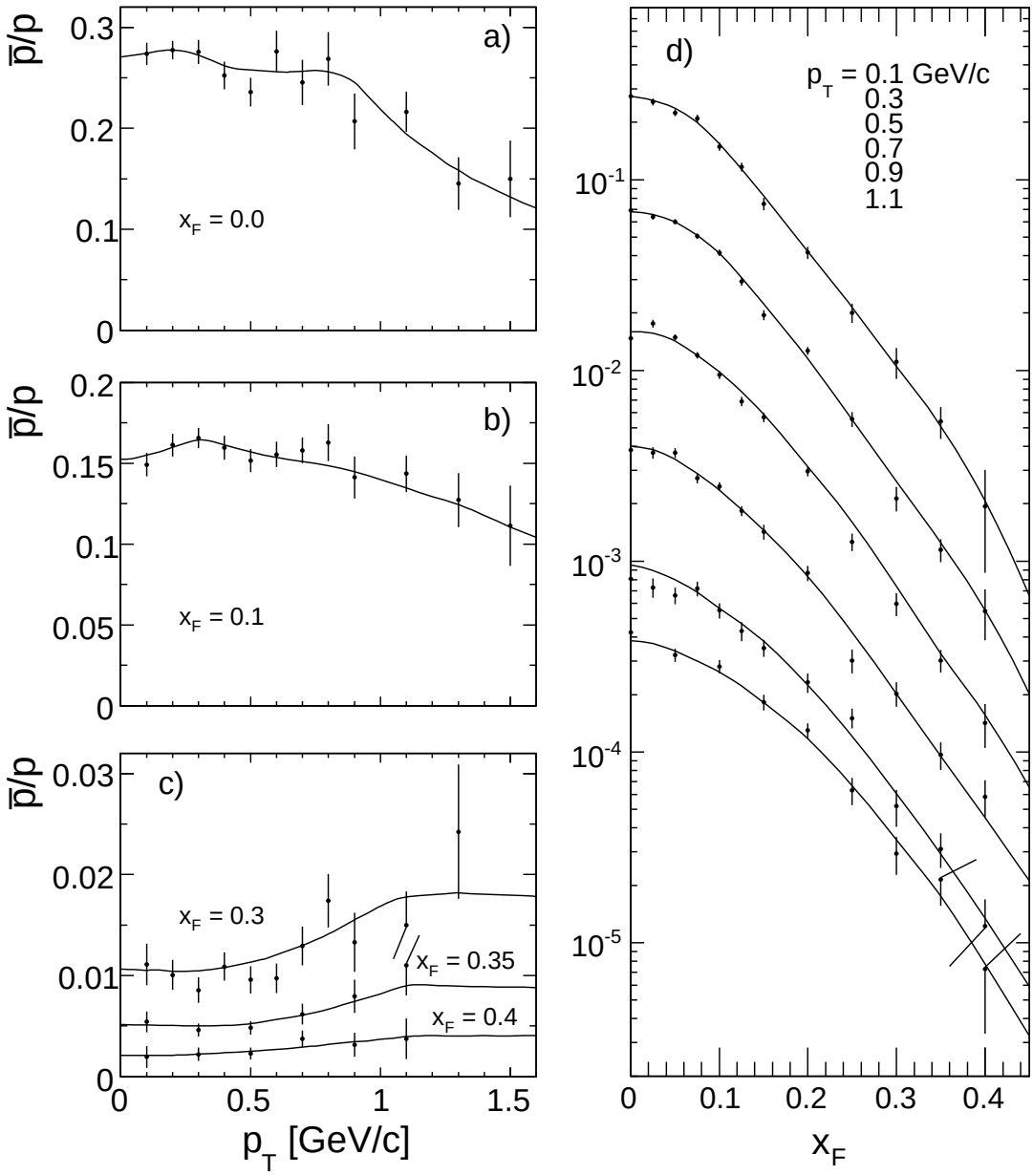

Figure 24: Ratio of invariant cross section for anti-protons and protons ($\overline{p}$/p) as a function of a), b) and c) p_T at fixed x_F and d) x_F at fixed p_T. The data in panel d) were successively divided by 4 for better separation

Here the invariant proton cross sections increase with x_F whereas the anti-protons fall off steeply with x_F similar to mesonic production [1]. It is therefore interesting to scrutinize the $\overline{\text{p}}$/p ratios quantitatively in both co-ordinates. This is presented in Fig. 24 which shows this ratio as a function of p_T for fixed x_F (left panels) and as a function of x_F for fixed p_T (right panel). In all plots the results from the two-dimensional interpolation discussed above are shown as lines through the data points.

Several features emerge from this comparison. The $\overline{\text{p}}$/p ratio falls with increasing p_T at $x_F \leq 0.1$ and increases with p_T at $x_F > 0.15$. The ratio between p_T = 0.1 and p_T = 1.5 GeV/c is about 2 at low x_F and about 0.5 at high x_F. This means that the p_T distribution of the anti-protons flattens out with increasing x_F until it becomes significantly broader than the one for protons at $x_F > 0.3$.

The $\overline{\text{p}}$/p ratio as a function of x_F at fixed p_T also shows distinctive trends. Here the steep x_F dependence at low p_T (a factor of about 130 between x_F = 0 and x_F = 0.4) flattens out at higher p_T (a factor of only 30 over the same x_F range).

The situation is clarified by the summary plots of Fig. 25 where only the interpolated lines are shown as functions of p_T and x_F, respectively.

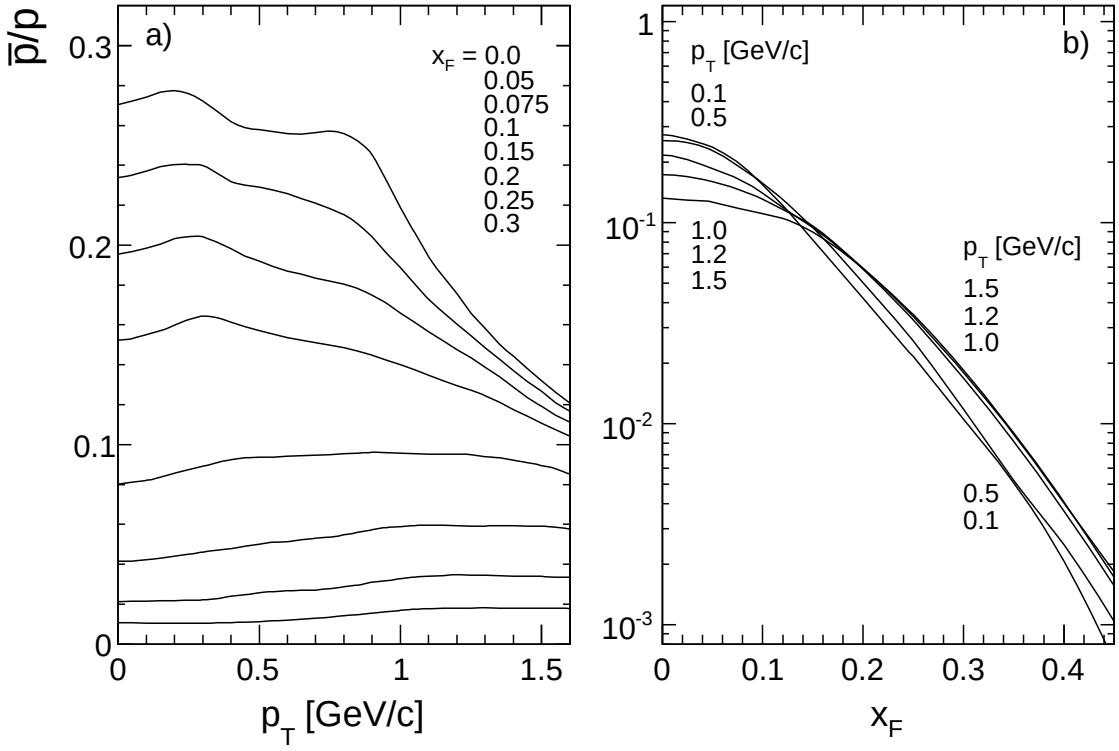

Figure 25: Interpolated ratios for anti-protons and protons ($\overline{\text{p}}$/p) as a function of a) p_T at fixed x_F and b) x_F at fixed p_T

7.6 Rapidity and transverse mass distributions

As in references [1, 30] the invariant cross sections are also presented, for convenience, as a function of rapidity at fixed p_T in Fig. 26. Here the absence of a "rapidity plateau" both for protons (with the exception of the region at $p_T > 1.5$ GeV/c) and for anti-protons should be noted.

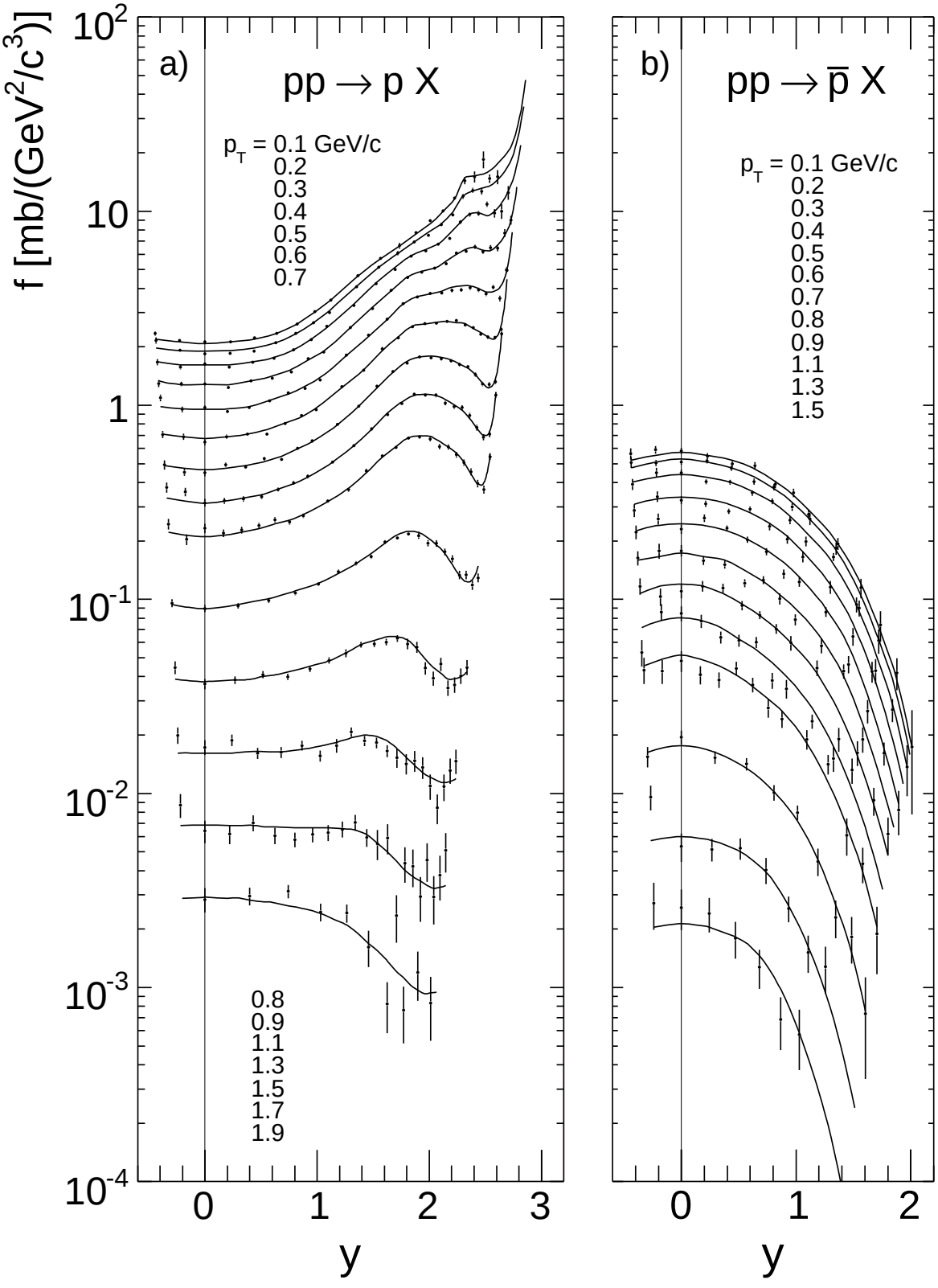

Figure 26: Double differential invariant cross section $f(x_F, p_T)$ [mb/(GeV^2/c^3] as a function of y at fixed p_T for a) protons and b) anti-protons produced in p+p collisions at 158 GeV/c beam momentum

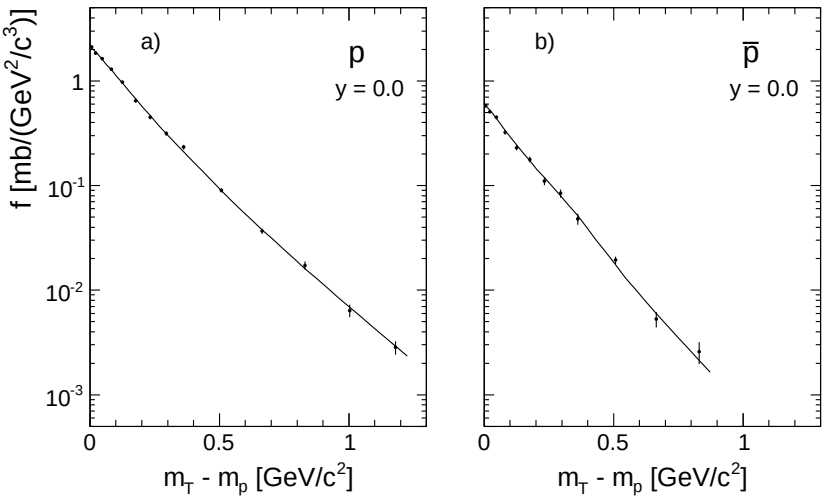

Figure 27: Invariant cross section as a function of $m_T - m_p$ for a) p and b) $\overline{p}$ produced at y = 0.0

Transverse mass distributions, with $m_T = \sqrt{m_p^2 + p_T^2}$, are shown in Fig. 27 for $x_F = y = 0$. In accordance with the $\overline{p}$/p ratios discussed above, a systematic difference between p and $\overline{p}$ is visible. The proton distribution is clearly not compatible with simple exponential shape, whereas the anti-proton distribution happens to be close to exponential up to the experimental limit of $m_T - m_p$ = 0.8 GeV/c^2.This is quantified by the dependence of the local logarithmic inverse slopes of $m_T - m_p$ given in Fig. 28. Here the slope defined by three successive data points has been used. In Fig. 28 also the inverse slopes obtained from the data interpolation, Sect. 7.3, are shown.

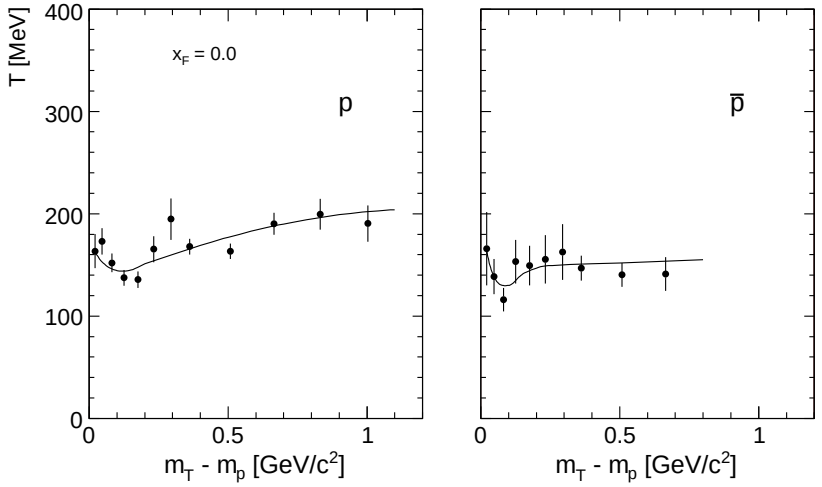

Figure 28: Local slope of the m_T distribution as a function of $m_T - m_p$ for p and $\overline{p}$. The lines corresponds to the data interpolation, Sect. 7.3

7.7 Baryon to pion ratios

The NA49 data on charged pions [1] offer a phase space coverage which is comparable in completeness, density and statistical accuracy to the results on baryons presented here. It is therefore indicated to compare the respective cross sections. This is done in the following

section by inspecting the corresponding ratios of invariant inclusive cross sections as functions of x_F and p_T.

For protons, the ratio $R = f_p/\langle f_\pi \rangle$, where $\langle f_\pi \rangle$ indicates the mean pion cross section $0.5 \cdot (f_{\pi^+} + f_{\pi^-})$, is presented in Fig. 29a as a function of p_T at fixed x_F and in Fig. 29b as a function of x_F for fixed p_T. For each data sample the corresponding interpolated cross section ratios are superimposed as full lines.

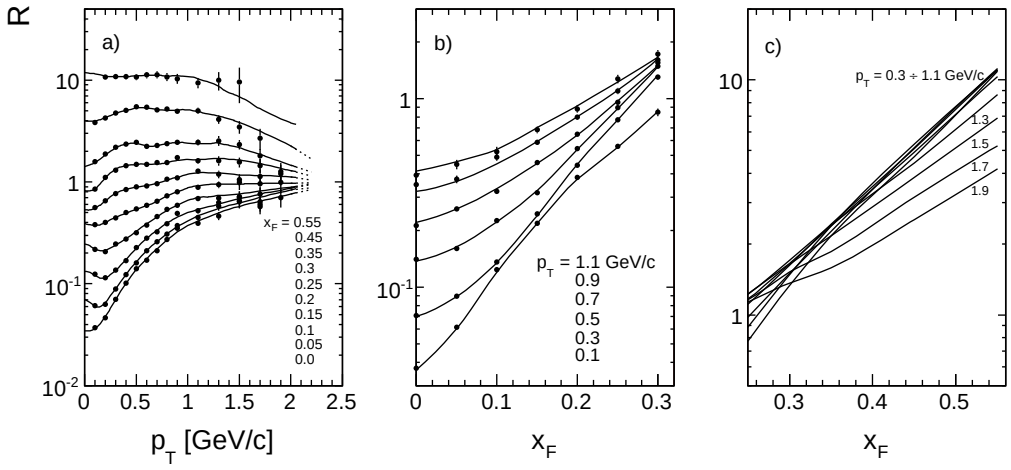

Figure 29: $R = f_p/\langle f_\pi \rangle$: a) as a function of p_T at fixed x_F, b) and c) as a function of x_F at fixed p_T. The full lines represent ratios of interpolated cross sections. Due to the close similarity of the p_T distributions in the range $0.3 < p_T < 1.1$ GeV/c only the interpolated lines are shown in panel c)

The p_T dependence, Fig. 29a, reveals structure at low p_T which has been shown in [1] to result from resonance decay, together with a strong increase of the ratio by almost three orders of magnitude between x_F = 0 and x_F = 0.5. This increase is progressively reduced with increasing p_T to less than an order of magnitude at $p_T \sim 2$ GeV/c. In fact R approaches unity in the high p_T region for all x_F values shown, and the extrapolation of the data interpolation (full lines) beyond the measured p_T range indicates a convergence point at $R \sim 1$ for $p_T \sim 2.5$ GeV/c. This is again an indication of resonance decay. A study of the pion cross sections resulting from the decay of an ensemble of 13 known resonances [42, 44] has indeed shown that the inclusive pion yields are saturated in the range $1.5 < p_T < 3$ GeV/c, at SPS energy, by two-body resonance decays. The high p_T pions originate either from high mass resonances or from the high mass Breit-Wigner tails of lower mass states. In both cases the available momentum q in the resonance cms becomes high enough so that the dependence on the mass m of the decay particle induced by the energy term

$$E_{\text{cms}} = \sqrt{q^2 + m^2} \tag{9}$$

in the Lorentz-transformation from the resonance cms to the experimental system becomes small. This means, always considering two-body decays, that the yield dependence on the kinematical variables x_F and p_T should become similar for pions and protons and therefore their ratio should tend to be stable against these variables. The actual limiting value of p/$\langle \pi \rangle$ depends however on the details of the isospin structure of the baryonic and mesonic resonances contributing to the proton and pion production in this section of phase space [42, 44].

The x_F dependence at fixed p_T, Fig. 29b, shows again the strong increase of R with x_F in the low p_T region, with a progressive tendency to flatten out with increasing p_T. This results, at p_T up to about 1 GeV/c, in a convergence point at $x_F \sim 0.5$ where R becomes practically p_T independent predicting the equality of mean p_T for pions and protons in this x_F region shown in Sect. 10.1, Fig. 56. At $p_T > 1.1$ GeV/c and $x_F > 0.3$, see Fig. 29c, the p_T distribution of protons becomes steeper than the one for pions. The ratio R thus approaches unity from above, whereas at $x_F < 0.3$, Fig. 29b, the opposite trend is visible as discussed above.

Concerning the relation of anti-protons to pions it is indicated to rather study the $\overline{\mathrm{p}}/\pi^-$ ratios. This is due to the similar isotriplet structure of both the baryon-pair and the pion production [33], see also Sect. 11.1. The $\overline{\mathrm{p}}/\pi^-$ ratios are shown in Fig. 30 both as a function of p_T at fixed x_F and as a function of x_F at fixed p_T.

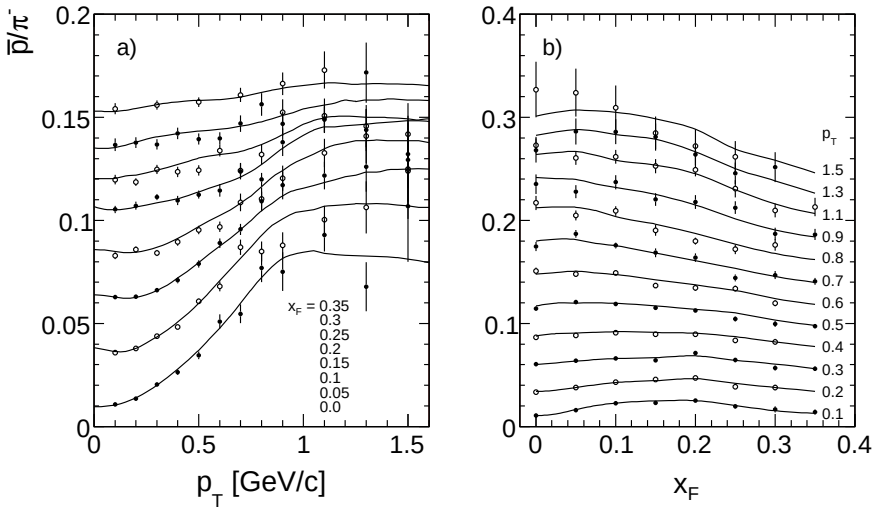

Figure 30: $\overline{\mathrm{p}}/\pi^-$ as a function of a) p_T at fixed x_F, b) x_F at fixed p_T. The full lines represent data interpolation. Data points and interpolated lines of subsequent x_F (p_T) values are shifted upwards by 0.02 in $\overline{\mathrm{p}}/\pi^-$

Due to the larger error bars for $\overline{\mathrm{p}}$ production together with the smaller range of variation, data points and interpolated lines of subsequent x_F (Fig. 30a) and p_T (Fig. 30b) values are shifted upwards by 0.02 in $\overline{\mathrm{p}}/\pi^-$. The full lines correspond again to the two-dimensional interpolation of the invariant cross sections.

Similar to what has been shown for $\mathrm{p}/\langle\pi\rangle$, the $\overline{\mathrm{p}}/\pi^-$ ratios increase strongly with p_T at low x_F by about one order of magnitude, Fig. 30a. And similarly, this increase reduces for larger x_F to a factor of only ~ 2 at the limit of the measurements at x_F = 0.35. In contrast there is a general flattening of the p_T dependence for p_T beyond about 1.2 GeV/c.

As far as the x_F dependence is concerned, Fig. 30b, the strong increase observed for $\mathrm{p}/\langle\pi\rangle$ with x_F is inverted to a general modest decrease which amounts to a factor of about four between x_F = 0 and 0.35 at the highest p_T values. At p_T below 0.4 GeV/c however the ratios show a distinct maximum at $x_F \sim 0.2$ and little if any difference comparing the values at x_F = 0 and 0.35.

In order to bring out the trends described above more clearly, the ratios of the interpolated cross sections are shown, without scale shift, separately in Figs. 31a and 31b.

Here again, it is worth to note the flattening of the p_T dependence above 1.2 GeV/c and the convergence of the ratios for the higher x_F range where the mean p_T for $\overline{\mathrm{p}}$ and pions becomes comparable.

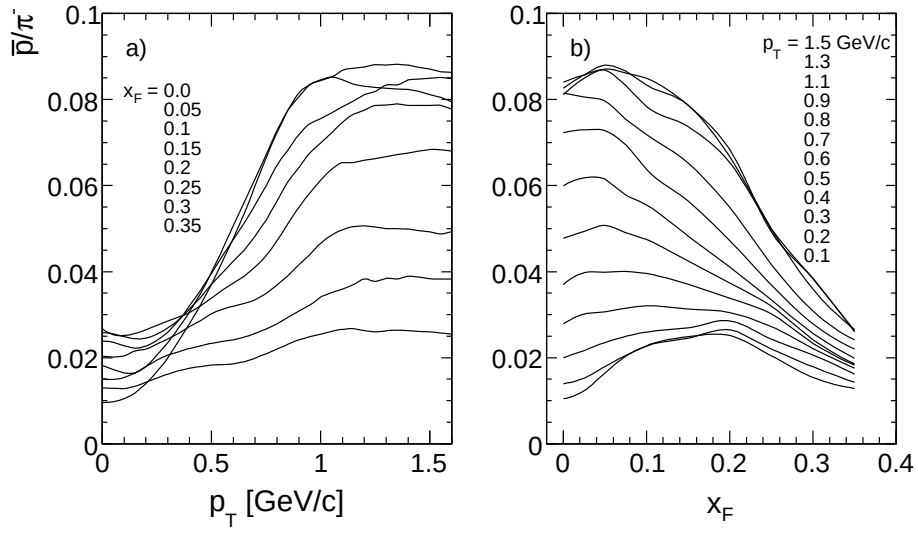

Figure 31: $\overline{\mathrm{p}}/\pi^-$ from data interpolation as a function of a) p_T at fixed x_F, b) x_F at fixed p_T

8 Comparison to Fermilab data

8.1 The feed-down problem

Before proceeding to a detailed comparison with the data sets specified in Sect. 2, the general problem of baryon feed-down from weak decays of strange hyperons has to be discussed. In the case of the NA49 data a feed-down correction has been performed (Sect. 6.4). It amounts to typically 5-20% of the measured baryon yields, with specific x_F and p_T dependences. This is only a fraction of the total hyperon decay contribution as the TPC tracking system of the NA49 detector has a resolution of the primary vertex position sufficient to reject a major part of the decay baryons. This is not a priori true for the reference data. As most of the corresponding experiments date from the 1970's to the early 1980's, micro-vertex detection or precision tracking was not available and therefore a large fraction if not all of the decay baryons contributed to the measured cross sections. What counts here is the distance of the first tracking elements from the primary vertex in relation to the typical hyperon decay length.

For the CERN ISR collider it may be stated that, given the different detector layouts for the x_F and p_T ranges covered, and given the large dimension of the interaction diamond, practically all baryonic decay products are included in the published data. A correction for this feed-down has not been attempted by any of the quoted experiments.

For fixed-target experiments the situation is somewhat more complicated as the range of lab momenta covered shows a much larger variation. Measurements in the target hemisphere with lab momenta comparable to the range at colliders are definitely prone to feed-down contamination. But even in the forward direction with momenta in the range of several tens of GeV/c, in many cases the first active detector elements are many meters away from the primary vertex, not to mention the general absence of precision tracking. A precise simulation of trajectories through the detectors and the aperture-defining collimators would be mandatory to come to a quantitative determination of the feed-down contributions.

A feeling for the size of the corresponding corrections may be obtained from Fig. 32 where the total yield of decay products is given in percent of the direct baryon cross section for protons and anti-protons at $\sqrt{s}$ = 17.2 GeV/c.

Whereas this fraction tends to decrease below the 10% level at $x_F > 0.4$ for protons, it

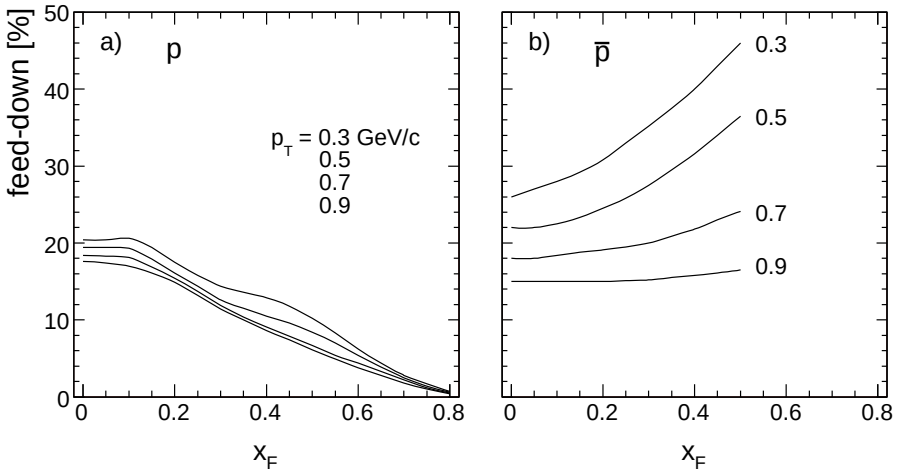

Figure 32: Total feed-down for a) protons and b) anti-protons as function of x_F for different p_T values

stays constant or even increases with x_F for anti-protons, with a sizeable p_T dependence. The data comparisons carried on below will therefore attempt to address this problem on a case-to-case basis.

8.2 The Brenner et al. data, [9]

This experiment offers 90 overlapping data points for protons and 19 points for anti-protons at the two beam momenta of 100 and 175 GeV/c. If the statistical errors of the proton sample are typically on the 1-10% level, the ones for anti-protons are considerably larger and vary between 20 and 50%. The situation is quantified in Fig. 33 which shows the distribu-

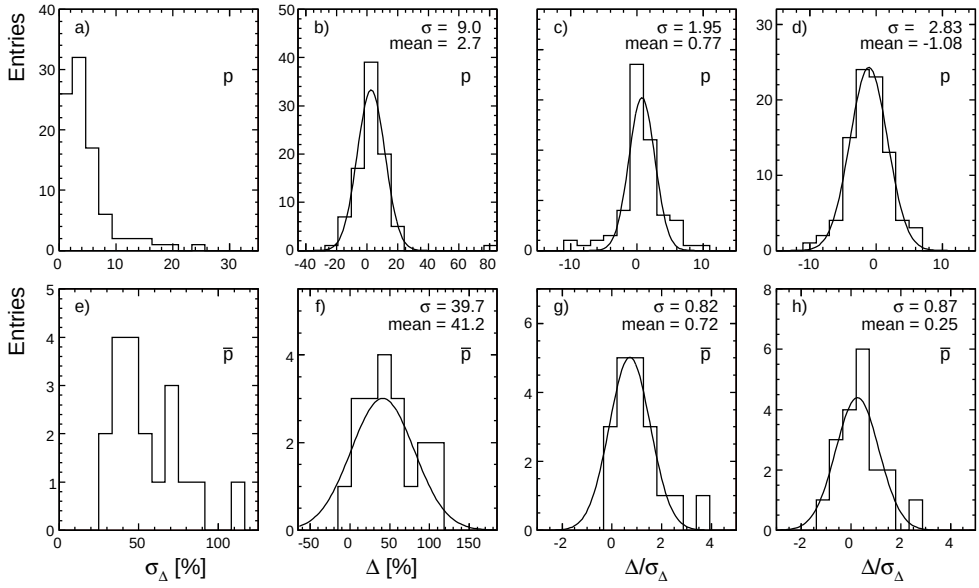

Figure 33: Statistical analysis of the difference between the measurements of [9] and NA49 for protons (upper four panels) and anti-protons (lower four panels): a) and e) error of the difference of the measurements; b) and f) difference of the measurements; c) and g) difference divided by the error; d) and h) difference divided by the error after feed-down correction of data from [9]

tions of the statistical errors, the differences to the interpolated NA49 data and the differences normalized to the statistical errors for protons and anti-protons, with and without feed-down correction of [9]. This latter distribution should be centered at zero with variance unity if the two measurements are compatible on an absolute scale.

Evidently the feed-down correction helps to reduce the almost 50% average difference for anti-protons, but over-corrects for protons. It should however be realized that the mean differences are for protons on the $\pm 4\%$ level which signals good agreement if compared to the quoted absolute normalization errors. This result verifies the excellent agreement found in [1] for pions.

The distribution of the comparison data over phase space may be judged from Fig. 34 where the x_F and p_T distributions of the data points from [9] are given against the interpolated NA49 data.

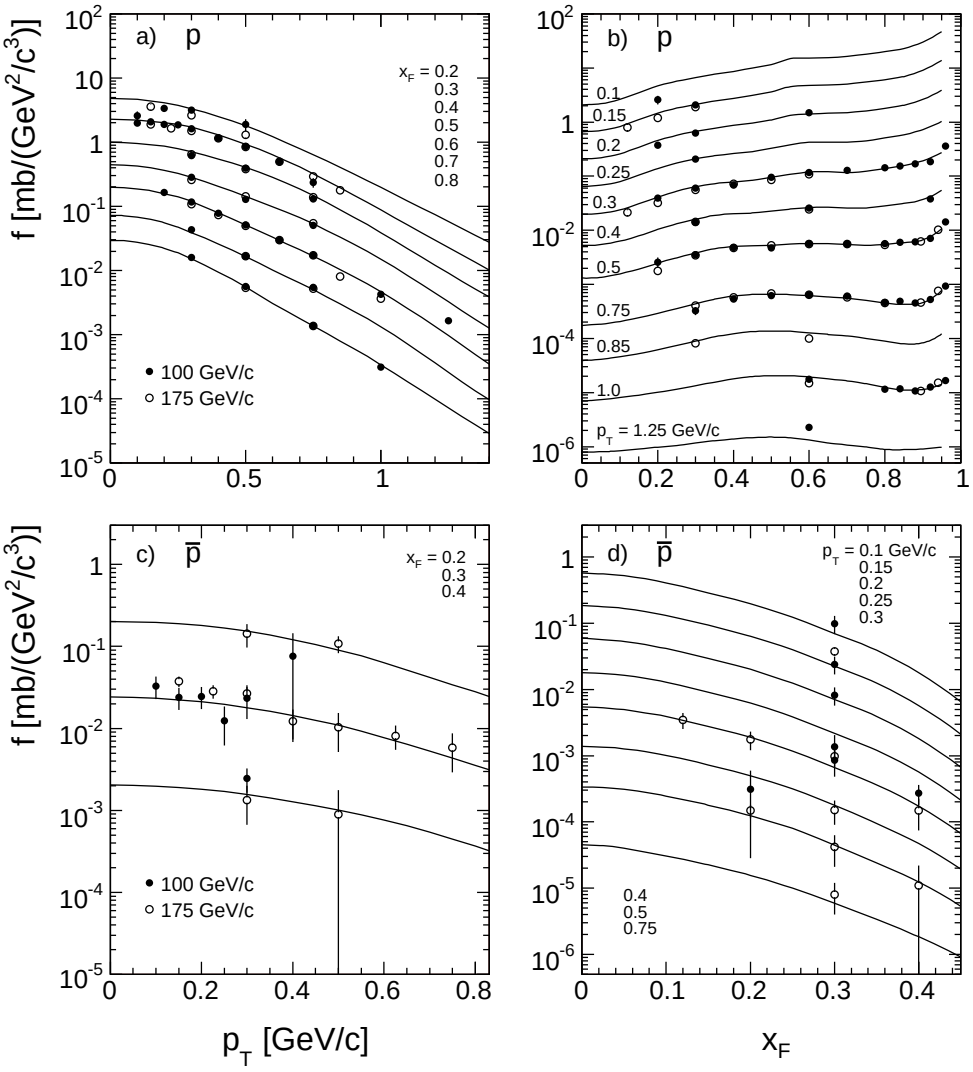

Figure 34: Comparison of invariant cross section between NA49 (lines) and measurements from [9] at 100 (full circles) and 175 GeV/c (open circles) for protons as a function of a) p_T at fixed x_F and b) x_F at fixed p_T, and for anti-protons as a function of c) p_T at fixed x_F and d) x_F at fixed p_T. The data were successively divided by 3 for better separation

8.3 The Johnson et al. data, [10]

From this experiment 54 and 26 data points for protons and anti-protons, respectively, may be used for comparison. The data were obtained at 100, 200 and 400 GeV/c beam momentum. As in the Brenner experiment, there is a large difference between the statistical errors of protons (2-6%) and anti-protons (10-30%).

As the measurements were done in the backward hemisphere up to maximum lab momenta of 2.3 GeV/c and as the aperture defining first magnet is placed at about 7 decay lengths for the maximum contributing hyperon momentum, a major fraction of the feed-down baryons must be expected to be contained in the data sample. This is visible in Fig. 35 where again the distributions of the statistical error, of the difference and the relative difference to the NA49 data with and without feed-down correction are presented.

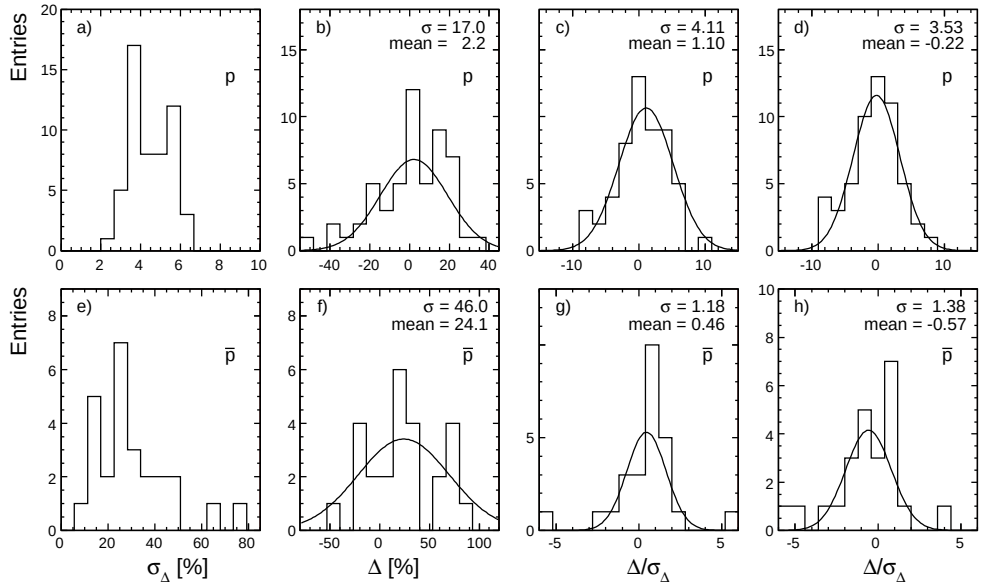

Figure 35: Statistical analysis of the difference between the measurements of [10] and NA49 for protons (upper four panels) and anti-protons (lower four panels): a) and e) error of the difference of the measurements; b) and f) difference of the measurements; c) and g) difference divided by the error; d) and h) difference divided by the error after feed-down correction of data from [10]

Particularly for protons an improvement of the experimental differences is visible with feed-down correction, with mean deviations on the few percent level. The large rms values of the relative differences are, however, noteworthy. As was already the case for the pion comparison [1], this speaks for additional fluctuations beyond those from counting statistics proper in this experiment. Why the mean relative deviations are below one standard deviation for the baryons and about 3 standard deviations for pions [1] remains however an open question.

The phase space distribution of the Johnson data, compared to the NA49 data interpolation, is shown in Fig. 36.

8.4 The Antreasyan et al. data, [2]

This so-called "Cronin" experiment represents the only measurement near $x_F = 0$ in the SPS energy range. As it is overlapping with the lower ISR energy range there is a long standing problem with an unresolved discrepancy of the proton yields by about a factor of 1.3–1.4 and of the anti-proton yields by a factor of 2, whereas there is reasonable agreement of the pion cross

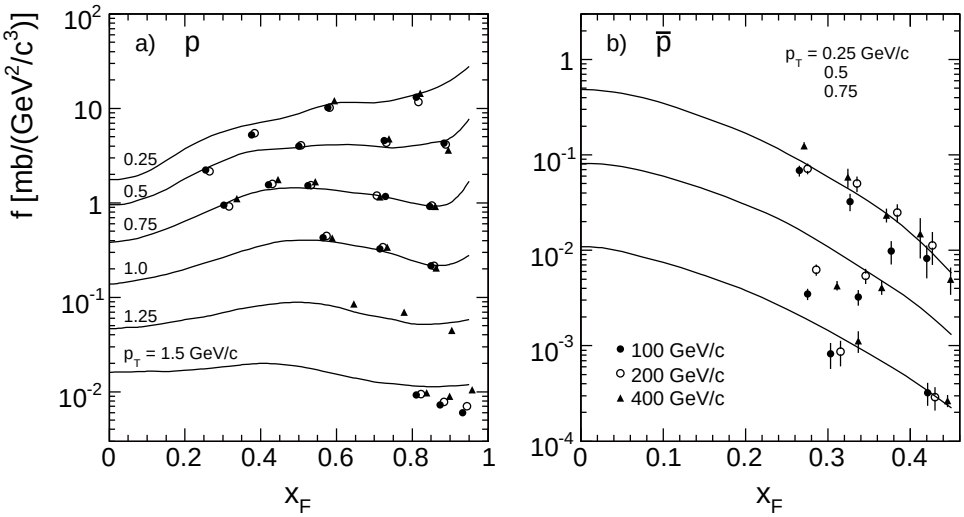

Figure 36: Comparison of invariant cross section between NA49 (lines) and measurements from [10] at 100 (full circles), 200 (open circles) and 400 GeV/c (full triangles) as a function of x_F at fixed p_T for a) protons and b) anti-protons. The anti-proton data were successively divided by 3 for better separation

sections [18]. The experiment which was aiming at high p_T production contributes just a couple of cross sections at the p_T values of 0.77 and 1.54 GeV/c in the NA49 p_T range.

A first problem is connected with the fact that the spectrometer was set to a constant lab angle of 77 mrad at all energies and for all particle masses. This results in an $\sqrt{s}$ and p_T dependent offset in x_F which introduces non-negligible variations of the cross sections. This is quantified in Table 6 which gives the corresponding deviations in x_F and of proton and anti-proton cross sections Δf, referred to x_F = 0.

p_T	p_{beam}	200	300	400
	$\sqrt{s}$	19.3	23.7	27.3
0.77	x_F	-0.028	-0.045	-0.053
	$\Delta f_{\bar{\text{p}}}$ [%]	-3.5	-8.9	-12.0
	Δf_{p} [%]	1.2	3.1	4.2
	$R_{\bar{\text{p}}}$	0.713±0.081	0.972±0.097	0.956±0.101
	R_{p}	0.726±0.084	0.797±0.082	0.760±0.081
1.54	x_F	0.013	-0.020	-0.037
	$\Delta f_{\bar{\text{p}}}$ [%]	-0.3	-0.8	-2.2
	Δf_{p} [%]	–	–	–
	$R_{\bar{\text{p}}}$	0.756±0.058	1.230±0.059	1.540±0.059
	R_{p}	0.728±0.044	0.824±0.044	0.809±0.074

Table 6: Offset in x_F and difference Δf in the cross section due to this offset at different $\sqrt{s}$ and p_T. The cross section ratio R between the data from [2] and NA49.

A second problem is also here connected to feed-down. As the first, aperture-defining collimators of the spectrometer are about 18 m downstream of the target, a good fraction of the feed-down baryons may enter into the acceptance. Following Fig. 32 this may well give downward corrections of up to 18% for protons and 13 to 16% for anti-protons in the given p_T range.

The cross section ratios R between the data from [2] and NA49 are also presented in

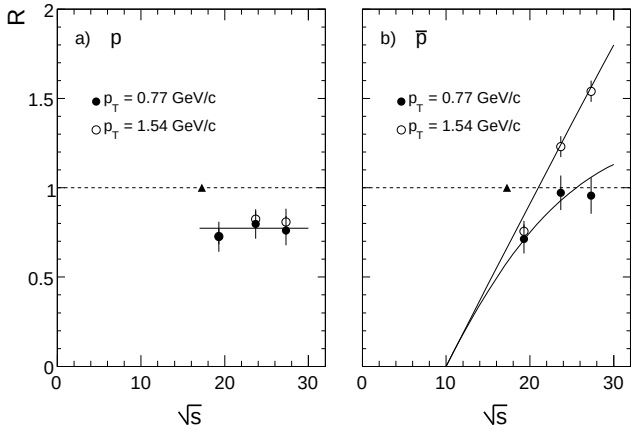

Figure 37: The cross section ratios R between the data from [2] and NA49 as a function of $\sqrt{s}$ for two values of p_T for a) protons and b) anti-protons. In both of the panels the NA49 point is indicated with full triangle

Table 6. They are shown in Fig. 37a for protons and Fig. 37b for anti-protons as a function of $\sqrt{s}$. For protons there is to first order an s-independent offset at 0.75, whereas for anti-protons the expected strong s-dependence of anti-baryon production is evident. In this case however, when extrapolating this dependence to $\sqrt{s}$ = 17.2 GeV, there is a discrepancy of about a factor of two as compared to the NA49 data. Similar discrepancies have been mentioned above with respect to the ISR data.

In order to clarify this experimental situation one may take reference to data at lower $\sqrt{s}$ and at ISR energies. In Table 7 the cross section ratios between the PS experiment of [31] at $\sqrt{s}$ = 4.9 and 6.8 GeV, the Serpukhov experiment of [32] at $\sqrt{s}$ = 11.5 GeV and the ISR measurements [18, 19] at $\sqrt{s}$ = 23 and 31 GeV, and NA49 are given. These data ratios are presented in Fig. 38 as a function of $\sqrt{s}$.

$p_T/\sqrt{s}$		4.9	6.8	11.5	23.0	31.0
0.77	$R_{\bar{p}}$			0.338±0.05	1.34 ±0.15	1.68±0.22
	R_p	3.13±0.30	1.99±0.22	1.37 ±0.18	1.02 ±0.10	1.07±0.10
1.54	$R_{\bar{p}}$			0.270±0.05	2.40 ±0.40	3.50±0.60
	R_p	2.35±0.60	1.76±0.60	0.970±0.15	0.992±0.15	1.13±0.15

Table 7: The cross section ratios R between the data from [18, 31, 32] and NA49

In Fig. 38a the very strong decrease of the central invariant proton cross section up to SPS energies is evident. This decrease is compensated by the comparatively strong increase of pair produced protons from Serpukhov through SPS up to ISR energies which produces an effective flattening of the s-dependence between $\sqrt{s}$ = 17.2 and 31 GeV followed by a steady increase at higher energies. As explained in detail in [33] the proper subtraction of the yield of pair-produced protons results in a continued decrease of the net proton yield to about zero at the highest ISR energies.

As shown in Fig. 38b the increase of the anti-proton cross sections from threshold through Serpukhov and SPS to ISR energies gives a consistent picture in the comparison of the experiments quoted in Table 7. The difference in the s-dependence between the lower p_T range at 0.77 GeV/c and the p_T of 1.54 GeV/c should be noted. It is evident also in the Cronin data, Fig. 37b.

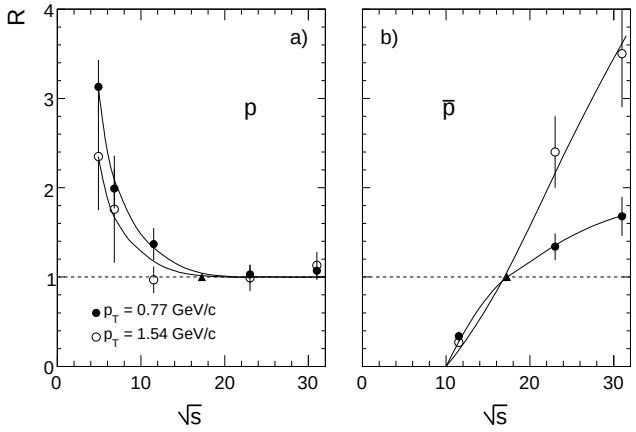

Figure 38: The cross section ratios R between the data from [18, 19, 31, 32] and NA49 as a function of $\sqrt{s}$ for two values of p_T for a) protons and b) anti-protons. In both of the panels the NA49 point is indicated with full triangle

In conclusion it appears that the data from [2] seem to be low for baryons in comparison to all other available data, by $\sim$ 25% for protons and $\sim$ 50% for anti-protons.

9 Comparison to ISR and RHIC data

As shown in Fig. 1 the ISR data on baryons cover the x_F/p_T plane quite extensively with a series of different spectrometer experiments in the range of $\sqrt{s}$ from 23 to 63 GeV. The present paper will limit the detailed comparison to the forward region at $x_F > 0.1$, with the exception of the preceding chapter where a few points at x_F = 0 were included in order to clarify the experimental situation. The reason for this limitation lies in the rapid evolution of both the proton and anti-proton yields at central rapidity and in the difficulties of defining "net" protons as the difference between proton and pair-produced proton cross sections. Here, the use of data from the isospin-reflected reaction n+p $\rightarrow$ p, $\overline{\text{p}}$ is mandatory in order to fully understand the isospin structure of baryon pair production [33]. The central area will therefore be treated in a subsequent publication including the neutron beam data available to NA49.

The main interest in regarding the forward ISR region of baryon production lies in a detailed study of s-dependence both of the proton and anti-proton cross sections, especially in relation to scaling concepts and to the question of form stability of the p_T and x_F distributions. Two collaborations [11–17] have contributed data in forward direction, with more than 1200 data points for protons and a comparatively rather limited set of only about 100 points for anti-protons.

It should be remarked that all ISR data are corrected by us for baryon feed-down from hyperon decay as described in Sect. 8.1.

9.1 Proton data [12–14] from ISR

The rich data set of [12–14], if compared directly and as a whole to the NA49 data, reveals a discouragingly wide distribution of differences, Fig. 39, with an rms of twice the mean statistical error and a full width at base of more than $\pm$50%. It will be demonstrated below that this may be understood as the combination of two effects, namely an apparent normalization uncertainty of about 10% rms and a very sizeable shape change of the x_F distributions in the

region $x_F > 0.7$ which introduces systematic deviations of up to 30%. In order to bring this out clearly the comparison will be conducted in several steps.

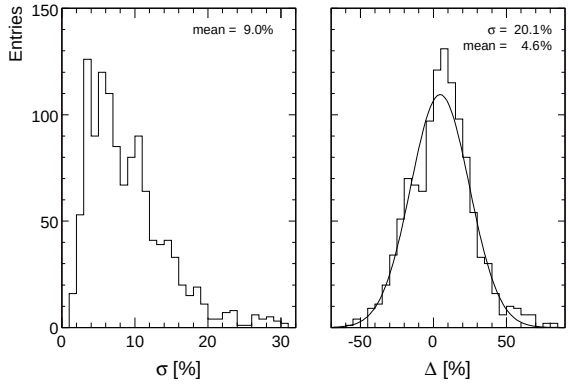

Figure 39: Statistical analysis of the difference of the ISR measurements [11–15] with respect to NA49: a) error of the difference and b) difference of the measurements

A first step regards the data [12] at $\sqrt{s}$ = 31 GeV (118 points), covering a range from 0.5 to 1 in x_F and from 0.47 to 1.08 GeV/c in p_T. The necessary feed-down correction to these data is relatively small, ranging from 8% at the lowest x_F to zero for $x_F > 0.85$. The overall distribution of differences against NA49 is shown in Fig. 40a where again the large width and a considerable offset are evident. When however plotting the differences for each of the 25 available x_F values separately, Fig. 40b, a sizeable depletion of the ISR data above x_F = 0.7 becomes visible, followed by a rapid increase towards the diffractive peak at $x_F > 0.97$. The mean values over p_T at each x_F, Fig. 40c, indicate this trend with good precision. When plotting the point-by-point differences to this curve, Fig. 40d, the rms width is reduced to the expected

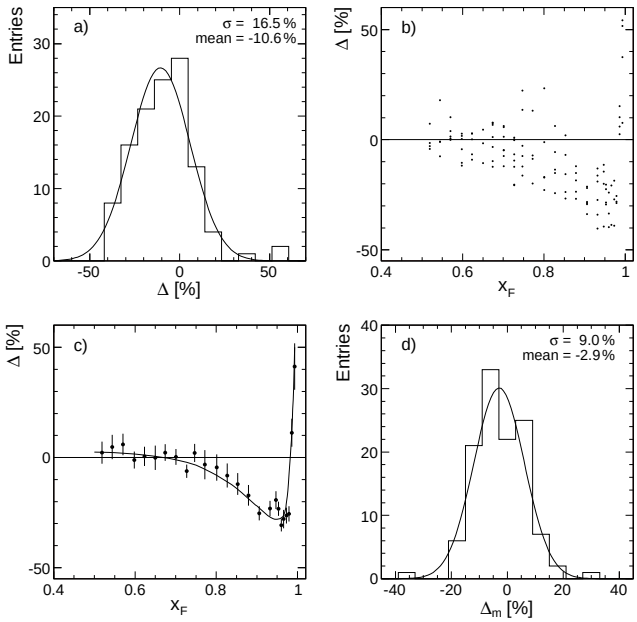

Figure 40: Comparison between [12] and NA49: a) distribution of differences, b) scatter plot of differences vs. x_F, c) mean values of differences over p_T as a function of x_F, d) distribution of point-by-point difference to the mean value Δ_m

mean value of the statistical errors.

It should be pointed out that in the region below x_F = 0.7 the mean difference is flat and close to zero with an offset of about +2.5% with respect to the NA49 data. This is a first indication of approximate scaling.

In a second step the data [13] are compared to NA49. This data set (134 points) covers a wide p_T range from 0.17 to about 2 GeV/c with x_F ranging from 0.3 to 0.7. These data are therefore below the region of depletion discussed above. The $\sqrt{s}$ ranges from 31 to 53 GeV.

A first look at the 9 available p_T distributions at the different $\sqrt{s}$ and x_F values as compared to the interpolated NA49 data, Fig. 41, shows good agreement as far as the shape over the full range of p_T is concerned.

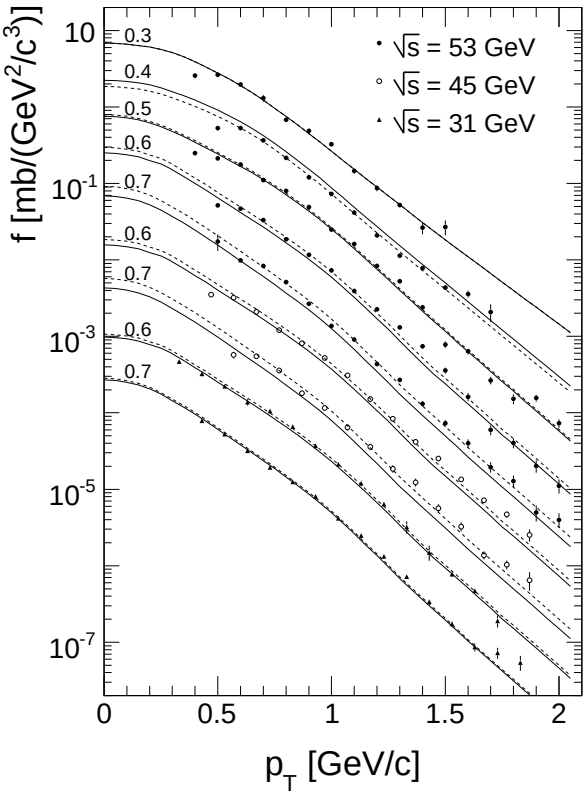

Figure 41: Comparison of p_T distribution at fixed x_F values (indicated in the plot) from [13] to interpolated NA49 data (full lines) and to interpolated NA49 data corrected with factors from Table 8 (dashed lines)

There are however noticeable offsets with respect to NA49 which may be described by multiplicative factors as shown in Table 8.

$x_F/\sqrt{s}$	31	45	53
0.3			1.00
0.4			0.83
0.5			1.05
0.6	1.09	1.18	1.18
0.7	1.05	1.33	1.33

Table 8: Offset factors with respect to NA49

Applying these factors to the ISR data the distribution of differences to NA49 becomes centered at zero with a variance which corresponds to the mean of the given statistical errors, Fig. 42.

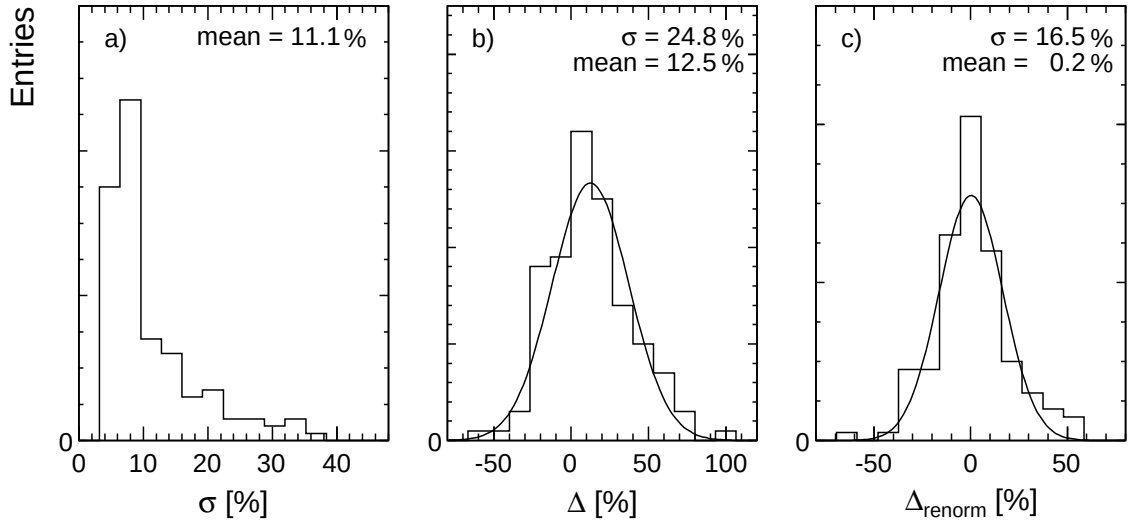

Figure 42: Statistical analysis of the difference of the ISR measurement [13] with respect to NA49: a) error of the difference, b) difference of the measurements and c) difference of the measurements after renormalization using the factors of Table 8

The mean of the offset factors, including the first data set discussed above, amounts to 1.10. This might indicate a general increase of the proton cross sections at ISR energies compared to the SPS by this amount. The sizeable fluctuation of the offset with both x_F and $\sqrt{s}$ shown in Table 8 indicates however at least an additional normalization problem.

This problem can be quantified in a third step by comparing the large data set [14] with about 1000 data points spread over 9 different values of $\sqrt{s}$ from 23 to 62 GeV, with p_T and x_F ranges of 0.3–1.7 GeV/c and 0.64–0.96, respectively. It should be mentioned that this experiment did not have particle identification so that in the lower x_F range a correction for π^+ and K^+ had to be applied (see Sect. 5.4).

A first impression of the evolution of the invariant cross section in the region above x_F = 0.65 may be obtained from Fig. 43 which shows the p_T averaged deviations from the NA49 data as a function of x_F for the nine $\sqrt{s}$ values. Although the depletion at $x_F > 0.8$ is generally similar to the one shown at $\sqrt{s}$ = 31 GeV (Fig. 40c) rather important overall deviations from unity in the flat region below x_F = 0.7 are visible, similar to the ones given in Table 8 for $\sqrt{s}$ = 45 GeV.

Tentatively normalizing this lower x_F region to the NA49 data one obtains the normalization factors given in Fig. 44 as a function of $\sqrt{s}$,including also the ones from Table 8. The projection of this distribution on the vertical axis shows a wide spread with an rms of about 14% and a mean of 1.16.

The variance is in agreement with the normalization uncertainty given by the experiment. The offset might indicate a general increase of the invariant cross section over the ISR energy range by about this amount. This will be discussed in more detail below.

As visible from Fig. 43 the depletion at high x_F develops in a characteristic fashion as a function of $\sqrt{s}$. In order to bring this evolution out more clearly the ISR data are normalized to NA49 using the low-x_F correction factors of Fig. 44 and the mean ratios plotted as a function

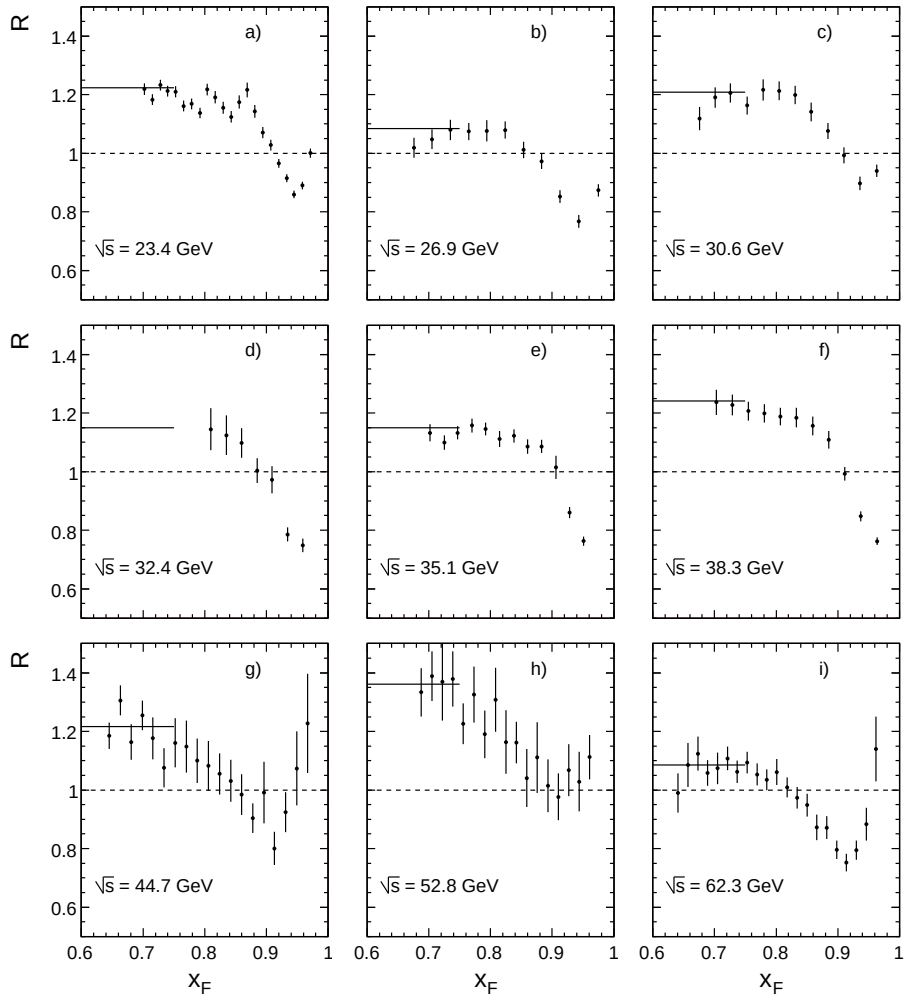

Figure 43: The p_T averaged ratio R of results from [14] to NA49 as a function of x_F for 9 different values of $\sqrt{s}$. The full lines denote the normalization factors shown in Fig. 44

of $\sqrt{s}$ at fixed x_F in Fig. 45.

In this Figure, the data from [3] have been included. Their slope against $\sqrt{s}$ has been used

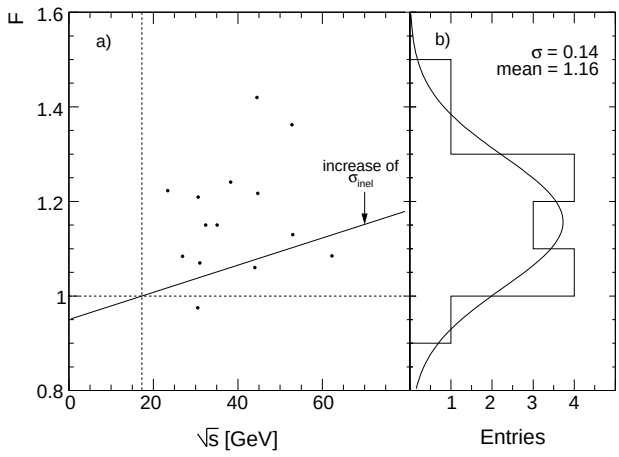

Figure 44: a) Normalization factors as a function of $\sqrt{s}$, b) distribution of normalization factors

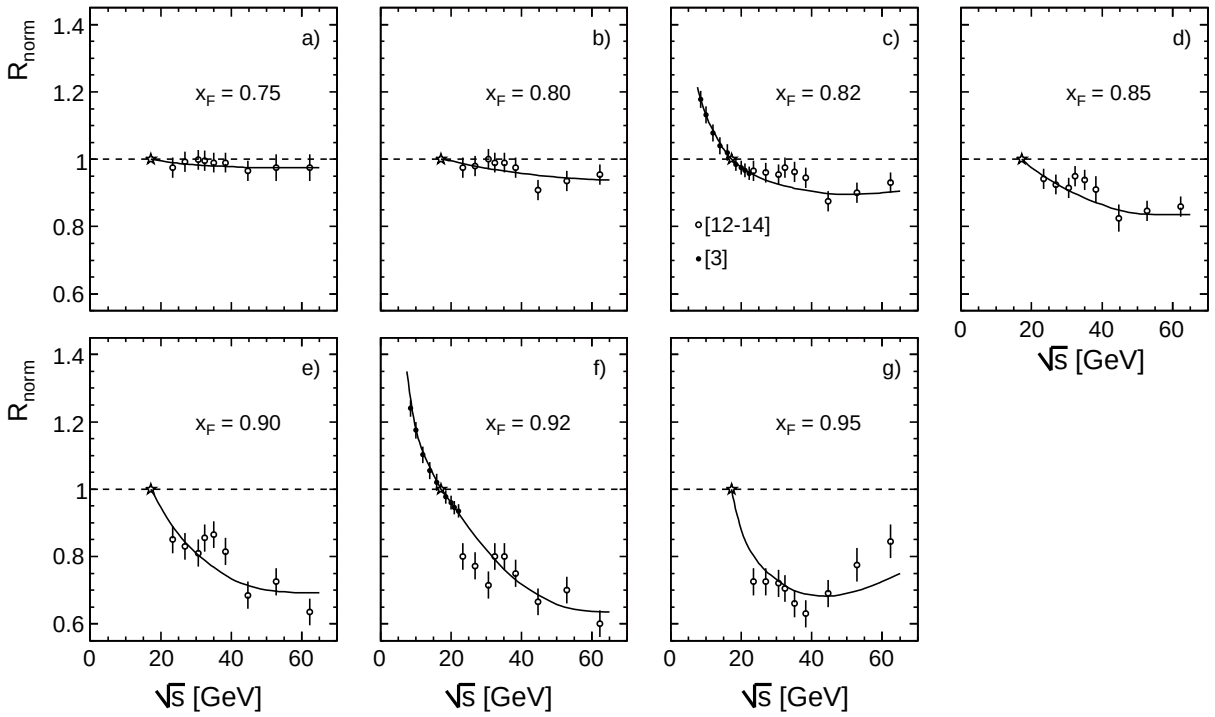

Figure 45: Normalized mean ratios $R_{\rm norm}$ as a function of $\sqrt{s}$ at fixed x_F. The star indicates the NA49 point

in Sect. 7.2 to correct the high-x_F Fermilab data for s-dependence. As is visible from Fig. 45 a consistent, smooth decrease of the invariant cross sections from $\sqrt{s}$ = 8 to $\sqrt{s}$ = 63 GeV/c is experimentally established. It continues to lower $\sqrt{s}$ with the data from [31] not shown here. Seen as a function of x_F this decrease starts at $x_F \sim 0.75$ with a few percent depletion and reaches its maximum at $x_F \sim$ 0.90–0.95 with an almost 40% effect.

In this context it is of course interesting to look at the higher $\sqrt{s}$ range of the p+$\overline{\rm p}$ colliders. Only one data set from the UA4 experiment [34] is available here which covers the x_F range from 0.92 to 1 with four p_T values between 0.74 and 1.07 GeV/c. Applying the same method described above by averaging over p_T and normalizing to the NA49 data, the $\sqrt{s}$ dependence shown in Fig. 46 is obtained.

Although the compatibility of the UA4 data with ISR results has been noted in [34] the strong s-dependence from lower energies implies a minimum of the invariant cross section at about RHIC energy and a subsequent rise towards p+$\overline{\rm p}$ collider energy, Fig. 46. This raises another question concerning baryon number conservation. As the total inelastic cross section rises by 13% at the highest ISR energy and by 48% at $\sqrt{s}$ = 540 GeV as compared to SPS energies, the proton density at high x_F will decrease faster than the invariant cross section with increasing s. This is indicated by the dashed line in Fig. 46 which shows the evolution of proton density rather than invariant cross section. In this case a flattening of the s-dependence up to collider energy is not excluded. As at the same time the central net proton density decreases at the higher ISR energy range [33] the eventual scaling of the invariant cross section in the intermediate x_F range has to be questioned. Unless the whole decrease of proton density at low and high x_F plus the increase of the inelastic cross section is absorbed into increased neutron or heavy flavour (mostly strangeness) production, there should be problems with baryon number conservation. In this sense the mean increase by about 20% of the invariant proton cross section

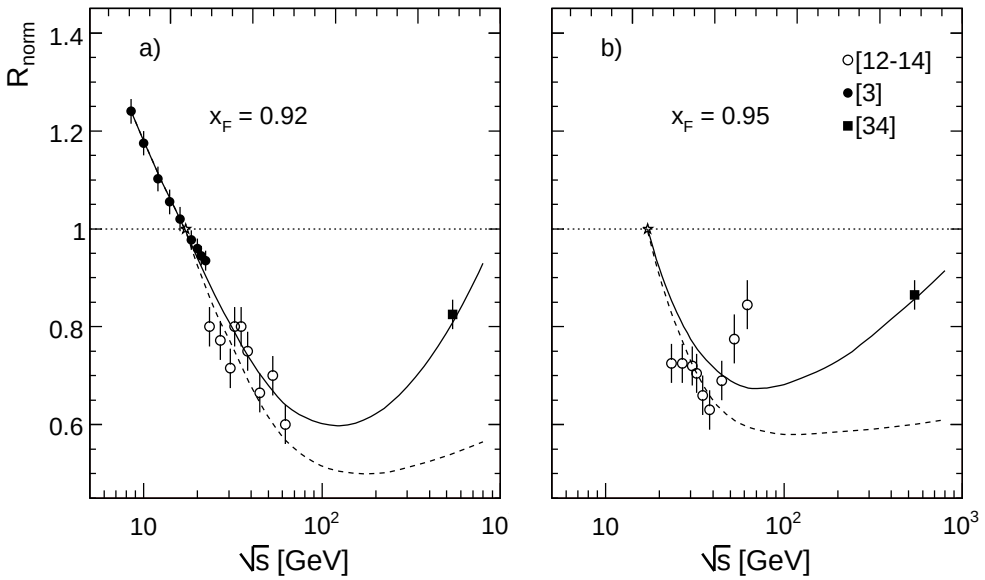

Figure 46: Normalized mean ratio $R_{\rm norm}$ as a function of $\sqrt{s}$ at fixed x_F including the UA4 measurement. The star indicates the NA49 point, full lines: invariant cross sections and dashed lines: proton density per inelastic event

which is visible in the average cross section ratios of Fig. 44 might be real. In fact the percentage rise of the inelastic cross section over the ISR energy range is also indicated in this Figure. Although of course the large systematic uncertainties in the ISR data do not allow for a definite statement, an upwards scaling violation of the invariant proton cross section of 10-20% over the ISR region cannot be excluded at this stage. The interesting intermediate $\sqrt{s}$ region at RHIC energy is only covered in the interval $0.1 < x_F < 0.3$ by the BRAHMS experiment [43] in two rapidity windows, see Sect. 9.5. However, recent data from deep inelastic leptoproduction at HERA [38, 39] help to fill the gap in x_F up to the kinematic limit at $\sqrt{s} \sim 130$ GeV, see Sect. 12.

9.2 Proton data [17] from ISR

The data of Capiluppi et al. [17] offer an additional set of proton cross sections with 184 points at four ISR energies and p_T and x_F ranges of 0.16–1.38 GeV/c and 0.05–0.6 respectively. This coverage has some overlap with the data [12–14] discussed above.

Plotting again, after feed-down correction, the point-by-point differences to the NA49 data, Fig. 47, a picture similar to Fig. 39 emerges with an average offset of +6% and an rms of 17%.

Given a mean statistical error of the data [17] of 13%, Fig. 48, this variance indicates again additional normalization and/or x_F and $\sqrt{s}$ dependences which are however much smaller than the ones found in the forward data of [12–14]. The distributions of the differences Δ with respect to the NA49 data plotted separately for the four $\sqrt{s}$ values, Fig. 48, indicate only a small if any s-dependence. There is also, within the statistical uncertainties, no discernible x_F dependence as shown by the mean differences as a function of x_F in Fig. 48.

It should however be mentioned that in this x_F region there are two counteracting phenomena to be taken into account. Firstly there is the decrease of central net proton density with increasing $\sqrt{s}$ in the approach to baryon transparency [33]. Secondly there is the strong increase of pair produced protons with $\sqrt{s}$, see Sect. 9.3 below. Both phenomena extend over the

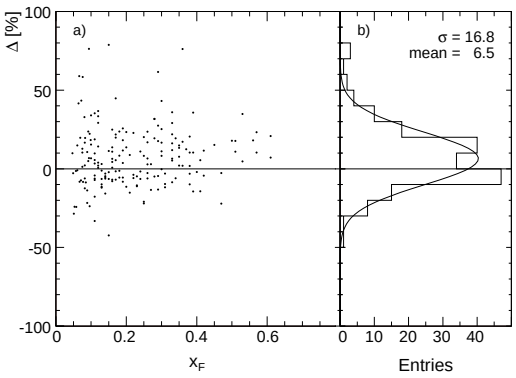

Figure 47: Comparison of the ISR measurement [17] to the NA49 results: a) difference Δ as a function of x_F and b) distribution of the differences

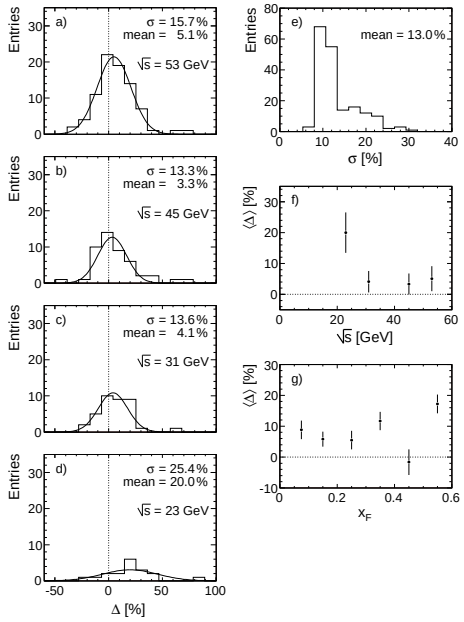

Figure 48: Distributions of the differences Δ for different energies: a) $\sqrt{s}$ = 53 GeV, b) $\sqrt{s}$ = 45 GeV, c) $\sqrt{s}$ = 31 GeV, d) $\sqrt{s}$ = 23 GeV; e) Distribution of the errors of [17]; Mean difference as a function of f) $\sqrt{s}$ and g) x_F

region of x_F studied here. A detailed discussion has to take into account, as already mentioned in Sect. 8.4 above, the isospin structure of baryon pair production. This will be elaborated in a subsequent publication. The observed overall offset of about +6% indicates again a possible upwards scaling violation of the invariant cross section in the ISR energy range on the 10% level.

9.3 Anti-proton data [15, 16] from ISR

The data of Albrow et al. [16] have been obtained at fixed angle and for three ISR energies of 31, 45 and 53 GeV. They cover a range of 0.12 to 0.6 in x_F and 0.16 to 0.8 GeV/c in p_T. The comparison to the NA49 data is shown in Fig. 49a without and 49b with feed-down subtraction.

The difference distributions of Fig. 49 show an offset of 34% for the non-subtracted case which reduces to 2% applying the feed-down correction. The variance of the distributions

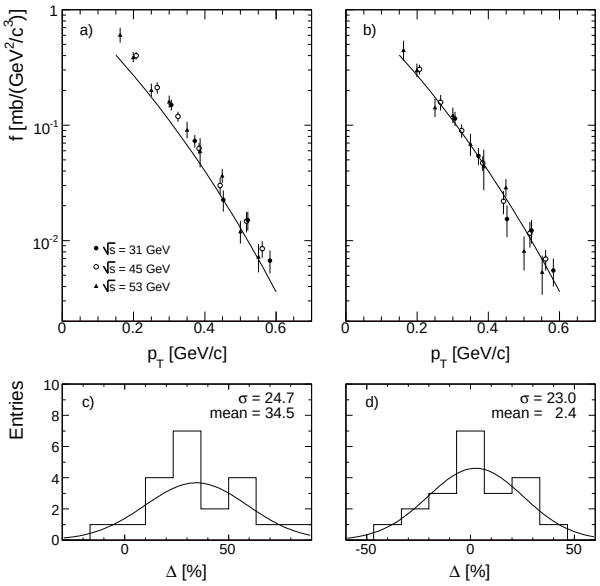

Figure 49: Comparison between data from [16] (points) and NA49 results (lines) as function of p_T: a) without feed-down correction of data [16] and b) with feed-down correction. Distribution of the differences: c) without feed-down correction and d) with feed-down correction

is again somewhat larger than the mean statistical error of 17% necessitating an additional fluctuation of the normalization of about 13% rms which complies with the estimated margin. There is no discernible s-dependence in the ISR data itself, and no s-dependence up from SPS energy after feed-down subtraction. This somewhat surprising result is verified by the second measurement [15] which provides 14 data points at fixed x_F = 0.19 and p_T ranging from 0.14 to 0.92 GeV/c and $\sqrt{s}$ = 53 GeV/c, Fig. 50.

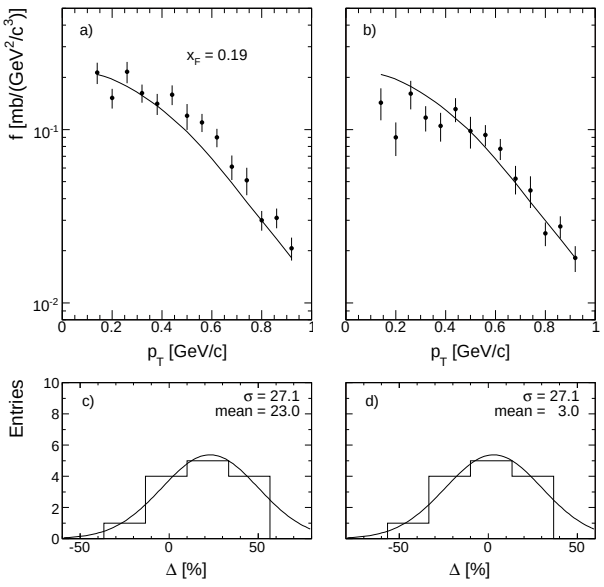

Figure 50: Comparison between data from [15] (points) and NA49 results (lines) as function of p_T: a) without feed-down correction of data [15] and b) with feed-down correction. Distribution of the differences: c) without feed-down correction and d) with feed-down correction

Again there is an offset of +23% without feed-down correction which reduces to +3% after subtraction. In this case the rms fluctuation of the differences is about a factor of 1.8 above the given statistical errors.

Taken at face value these results would establish a perfect scaling of the anti-proton cross sections from $\sqrt{s}$ = 17 to $\sqrt{s}$ = 53 GeV in the overlapping x_F range between 0.1 and 0.4.

9.4 Anti-proton data [17] from ISR

The anti-proton data from Capiluppi et al. [17] cover, for the four ISR energies 23, 31, 45 and 53 GeV, the x_F range from 0.05 to 0.42 and the p_T range from 0.18 to 1.29 GeV/c. Hence there is almost complete overlap with the data [15, 16]. Contrary to [15, 16] however, the data comparison with NA49 shows a large positive offset, see Fig. 51, with means of +100% without and +60% with feed-down subtraction.

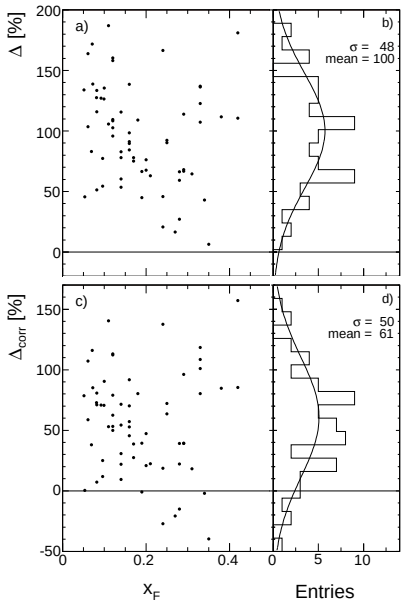

Figure 51: Comparison of the ISR measurement [17] to the NA49 results without feed-down correction of [17]: a) difference Δ as a function of x_F and b) distribution of the differences, and with feed-down correction: c) difference Δ_{corr} as a function of x_F and d) distribution of the differences

When plotting the difference distributions separately for the different $\sqrt{s}$ values, Fig. 52a-d, a clear s-dependence becomes evident, with mean values varying from +19% at $\sqrt{s}$ = 23 GeV to +74% at $\sqrt{s}$ = 53 GeV. A small x_F dependence cannot be excluded as shown in Fig. 52e. In Fig. 52f the different s-dependences treated in this paper, [19] at x_F = 0 and p_T = 0.77 GeV/c and [16] overlapping with [17] at $\langle x_F \rangle$ = 0.19 and $\langle p_T \rangle$ = 0.56 GeV/c are shown for comparison. Given the apparent strong s-dependence of the central anti-proton yields [18, 19], see Fig. 38, and the eventual decrease with x_F, Fig. 52, the results from [18, 19] and [17] may be regarded as compatible within the sizeable systematic errors. The results from Albrow et al. [15, 16] can however not be reconciled with the observed dependences. This discrepancy remains unexplained, especially in view of the fact that the proton and pion [1] yields from the same experiment do not show deviations of comparable magnitude.

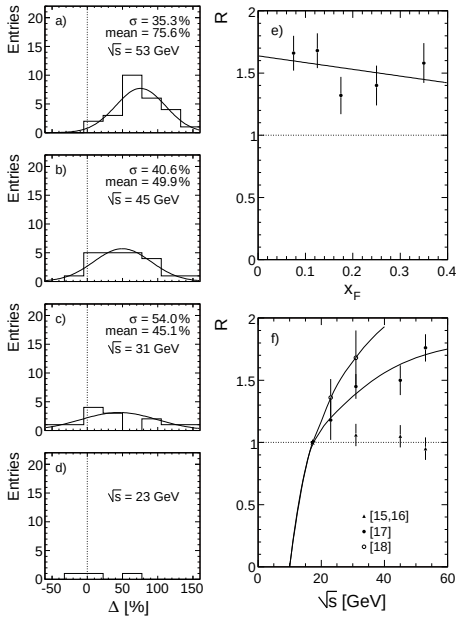

Figure 52: Distributions of the differences Δ for different energies: a) $\sqrt{s}$ = 53 GeV, b) $\sqrt{s}$ = 45 GeV, c) $\sqrt{s}$ = 31 GeV, d) $\sqrt{s}$ = 23 GeV; Mean difference as a function of e) x_F and f) $\sqrt{s}$

9.5 Proton and anti-proton data [43] from RHIC

As explained above in the beginning of Sect. 9, the present paper limits itself to the discussion and comparison of data in the range $x_F > 0.1$. In view of the discussion of s-dependence in Sects. 9.1 and 9.2 it is of particular interest to include data from RHIC into the comparison. The BRAHMS collaboration has recently presented baryonic data [43] from p+p collisions at $\sqrt{s}$ = 200 GeV at the forward rapidities of 2.95 and 3.3 and at transverse momenta larger than 0.7 and 1.3 GeV/c, respectively. Viewed in the scaling variable x_F, Fig. 53c, this corresponds

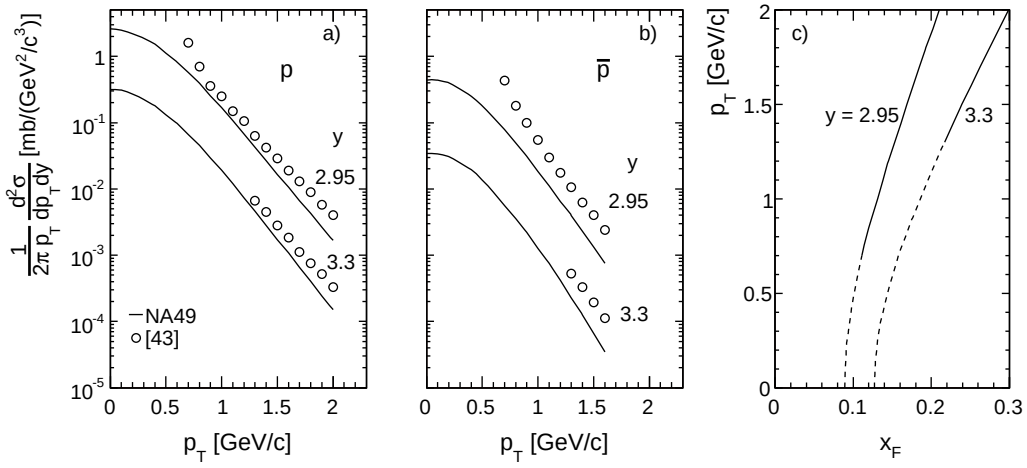

Figure 53: Comparison of data from [43] with NA49 results as a function of p_T at two rapidity values for a) protons and b) anti-protons. The measurements at y = 3.3 are multiplied by 0.1 for better separation. Panel c) values of x_F and p_T corresponding to the two rapidity windows of the BRAHMS experiment

to a range from 0.1 to 0.3 which offers considerable overlap with the NA49 experiment and the ISR data of [17].

The invariant p_T distributions of protons and anti-protons for the two rapidities are presented in Fig. 53a,b together with the NA49 data interpolated to the corresponding (x_F,p_T) values.

Several features are noteworthy in this comparison:

– the BRAHMS data for protons are very close for the two rapidity windows in the common p_T range from 1.3 to about 1.6 GeV/c, see also Fig. 54.
– the same is true for the NA49 data. In the range $p_T > 1.6$ GeV/c the cross sections at the higher rapidity are depleted by similar amounts in both experiments.
– at $p_T < 0.9$ GeV/c the BRAHMS data diverge sharply upwards from the NA49 distribution.
– a similar pattern emerges for the anti-proton data although the comparison is here limited to $p_T < 1.6$ GeV/c due to the counting statistics of NA49. There is however a general depletion of the cross sections in passing from 2.95 to 3.3 units of rapidity.

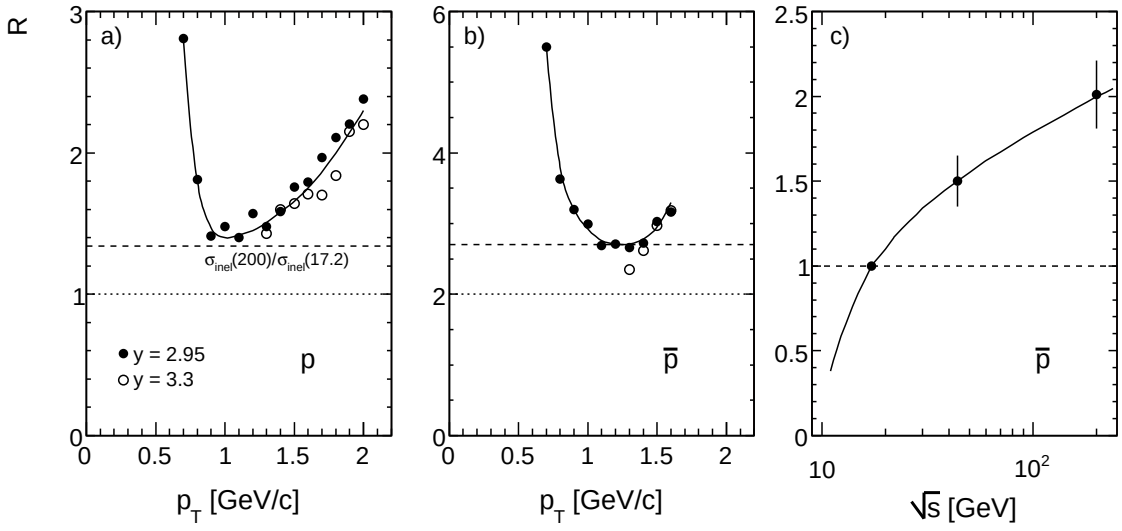

Figure 54: Ratio R between BRAHMS and NA49 cross sections as a function of p_T at two rapidity values for a) protons and b) anti-protons; c) R as function of $\sqrt{s}$ including point from ISR [17]. The ratio of inelastic cross sections $\sigma_{\text{inel}}(200)/\sigma_{\text{inel}}(17.2)$ is indicated in panel a) with a dashed line

This situation is quantified by the cross section ratios plotted in Fig. 54. The proton ratios, Fig. 54a, decrease sharply from 2.8 at the lower limit of the BRAHMS acceptance to values of about 1.4 in the range $0.9 < p_T < 1.3$ GeV/c. This ratio is close to the ratio of inelastic cross sections $\sigma_{\text{inel}}(200)/\sigma_{\text{inel}}(17.2)$ indicated as a line at 1.34 in Fig. 54a. Tentatively attributing the low-p_T divergence to an edge effect of the BRAHMS acceptance one may argue that in the region below $p_T \sim 1$ GeV/c the invariant cross sections are scaled up by just the ratio of the inelastic cross sections, see also the argumentation in Sect. 9.1 concerning s-dependence. This would mean that the proton densities in the x_F range considered here are s-independent with the exception of the high-p_T region above about 1 GeV/c where a substantial increase of R is visible. Compare also the discussion of the HERA data at $\sqrt{s}$ = 130 GeV in Sect. 12 at low $p_T < 0.6$ GeV/c.

For the anti-proton ratios, Fig. 54b, a qualitatively similar picture emerges, with the im-

portant exception that there is a general increase of the invariant yields beyond the ratio of the inelastic cross sections. The divergence at $p_T < 0.9$ GeV/c is quantitatively the same as the one observed for protons, indicating problems at the lower edge of the BRAHMS acceptance also for anti-protons. As already observed for protons the ratios for y = 2.95 and y = 3.3 are quite similar and they tend to be constant at $1.0 < p_T < 1.4$ GeV/c followed by an increase towards higher p_T. For anti-protons however, the flat part of the ratio corresponds to a value of 2.7. Repeating the argument for protons by taking into account the increase of the total inelastic cross section, an effective increase by a factor of 2 of the anti-proton density is resulting. Combining this increase with the one observed at the mean $\sqrt{s}$ of the ISR data [17], see Fig. 52e, in this x_F range, the s-dependence shown in Fig. 54c may be extracted.

In conclusion and within the x_F range of 0.1 to 0.3 the scaling of proton densities rather than inclusive cross sections may be established from SPS through ISR up to RHIC energies. For anti-protons, a smooth increase by about a factor of two is seen over the same $\sqrt{s}$ interval. For both particle types the yields increase towards higher p_T reaching for protons a factor of about 1.7 at 2 GeV/c as compared to SPS energy. This increase should be confronted with the apparent s-independence of the shape of the proton p_T dependences up to $\sqrt{s}$ = 53 GeV in this p_T range as demonstrated in Sect. 9.1, Fig. 41. Taken at face value this would mean that there is a strong evolution of the transverse momentum dependence between ISR and RHIC energies. Some basic differences between the ISR and RHIC experiments have, however, to be taken into account in this respect. If the ISR experiments were triggering on typically more than 90% of the total inelastic cross section, this is not true for the RHIC situation. The BRAHMS experiment for instance triggers on only 70% of the inelastic cross section with a trigger device which spans angles between 0.6 and 4.4 degrees with respect to the beams. In addition, a coincidence between both rapidity hemispheres is requested. This means that single as well as double diffractive events are excluded from the trigger. If this in itself might not introduce grave biases at least for proton production in the forward BRAHMS acceptance, see Sect. 6.2, it is the apparent azimuthal asymmetry of the beam-beam trigger system on the spectrometer side which might cause systematic effects. By pointing away from the spectrometer acceptance in the medium to high p_T region it will tend to increase the measured high p_T yield from simple energy-momentum conservation arguments. A strong azimuthal correlation between forward hadrons has indeed been observed in p+p interactions at the ISR [45] with trigger particles at $1 < p_T < 4$ GeV/c [46] in the x_F/p_T wedge of the BRAHMS trigger. This correlation increases strongly with p_T of both the trigger particle and the observed hadrons in the opposite azimuthal hemisphere. It is trivially explained by resonance decay governing the p_T region in question [42, 44]. In addition, comparing the forward pion yields measured by BRAHMS to the NA49 results [1] an increase of a factor of five is found at p_T = 2 GeV/c and y = 2.95, again in contrast to results at ISR energies. Also this effect is expected to follow from resonance production and decay. If extracting corrections for this trigger bias from microscopic hadronization models it must be ensured that production and decay of high mass states are properly contained in these models, see also the discussion in [42, 44].

10 Integrated data

10.1 $\mathbf{p_T}$ integrated distributions

The p_T integrated non-invariant and invariant baryonic yields are defined by:

$$dn/dx_F = \pi/\sigma_{\text{inel}} \cdot \sqrt{s}/2 \cdot \int f/E \cdot dp_T^2$$
$$F = \int f \cdot dp_T^2 \tag{10}$$
$$dn/dy = \pi/\sigma_{\text{inel}} \cdot \int f \cdot dp_T^2$$

with $f = E \cdot d^3\sigma/dp^3$, the invariant double differential cross section. The integrations are performed numerically using the two-dimensional data interpolation (Sect. 7.3). Table 9 gives the numerical values and the first and second moments of the p_T distributions, as functions of x_F and rapidity.

	p								$\overline{\text{p}}$								p	$\overline{\text{p}}$
x_F	F	Δ	dn/dx_F	Δ	$\langle p_T \rangle$	Δ	$\langle p_T^2 \rangle$	Δ	F	Δ	dn/dx_F	Δ	$\langle p_T \rangle$	Δ	$\langle p_T^2 \rangle$	Δ	y	dn/dy	dn/dy
0.0	0.7413	0.21	0.5749	0.21	0.5165	0.08	0.3601	0.16	0.1874	0.44	0.1477	0.42	0.4880	0.17	0.3156	0.31	0.0	0.07364	0.01869
0.025	0.7494	0.16	0.5696	0.16	0.5187	0.09	0.3629	0.16	0.1823	0.36	0.1407	0.35	0.4897	0.18	0.3176	0.34	0.1	0.07412	0.01860
0.05	0.7746	0.14	0.5576	0.14	0.5212	0.06	0.3658	0.13	0.1708	0.32	0.1247	0.31	0.4924	0.13	0.3216	0.27	0.2	0.07477	0.01815
0.075	0.8169	0.14	0.5439	0.14	0.5226	0.05	0.3671	0.10	0.1532	0.34	0.1031	0.33	0.4972	0.13	0.3286	0.23	0.3	0.07551	0.01759
0.1	0.8802	0.13	0.5351	0.13	0.5214	0.06	0.3655	0.12	0.1348	0.34	0.08245	0.34	0.5038	0.16	0.3378	0.31	0.4	0.07718	0.01681
0.125	0.9630	0.13	0.5321	0.13	0.5151	0.06	0.3585	0.09	0.1155	0.45	0.06394	0.45	0.5109	0.18	0.3478	0.31	0.5	0.07943	0.01587
0.15	1.0741	0.13	0.5388	0.13	0.5099	0.06	0.3510	0.11	0.09723	0.50	0.04872	0.50	0.5185	0.24	0.3581	0.42	0.6	0.08226	0.01479
0.2	1.3620	0.11	0.5682	0.11	0.4980	0.05	0.3341	0.09	0.06671	0.52	0.02772	0.52	0.5252	0.24	0.3665	0.46	0.7	0.08558	0.01360
0.25	1.6853	0.14	0.5944	0.14	0.4923	0.06	0.3242	0.10	0.04198	0.77	0.01475	0.77	0.5296	0.33	0.3710	0.62	0.8	0.09024	0.01237
0.3	2.0307	0.16	0.6165	0.16	0.4930	0.06	0.3216	0.11	0.02401	1.08	0.007262	1.08	0.5361	0.43	0.3789	0.76	0.9	0.09627	0.01103
0.35	2.3807	0.08	0.6323	0.08	0.4953	0.04	0.3220	0.07	0.01318	1.13	0.003491	1.13	0.5394	0.49	0.3826	0.82	1.0	0.10463	0.009639
0.4	2.6341	0.10	0.6205	0.10	0.4978	0.04	0.3248	0.07	0.006648	2.13	0.001562	2.14	0.5499	0.84	0.3911	1.53	1.1	0.11465	0.008296
0.45	2.8083	0.10	0.5938	0.10	0.4952	0.05	0.3237	0.08									1.2	0.12713	0.007015
0.5	3.0140	0.14	0.5778	0.14	0.4830	0.07	0.3108	0.11									1.3	0.14188	0.005733
0.55	3.2814	0.21	0.5740	0.21	0.4616	0.11	0.2891	0.18									1.4	0.15901	0.004543
0.6	3.3827	0.25	0.5458	0.25	0.4498	0.16	0.2746	0.22									1.5	0.17881	0.003424
0.65	3.3668	0.29	0.5032	0.29	0.4413	0.16	0.2645	0.25									1.6	0.20063	0.002444
0.7	3.2902	0.36	0.4577	0.36	0.4326	0.17	0.2559	0.27									1.7	0.22404	0.001646
0.75	3.3055	0.45	0.4301	0.45	0.4168	0.20	0.2402	0.32									1.8	0.24574	0.001052
0.8	3.4796	0.54	0.4252	0.54	0.3978	0.19	0.2195	0.33									1.9	0.25980	0.000615
0.85	3.7868	0.51	0.4362	0.51	0.3826	0.16	0.2032	0.29									2.0	0.26832	0.000298
0.9	4.5527	0.53	0.4877	0.53	0.3663	0.19	0.1875	0.33									2.1	0.27770	0.000110
0.95	6.8665	0.50	0.7056	0.50	0.3674	0.18	0.1859	0.31									2.2	0.29182	0.000028
																	2.3	0.30972	0.000005
																	2.4	0.31161	0.0000007
																	2.5	0.30474	
																	2.6	0.33347	
																	2.7	0.41145	
																	2.8	0.51284	
																	2.9	0.26117	

Table 9: p_T integrated invariant cross section F [mb·c], density distribution dn/dx_F, mean transverse momentum $\langle p_T \rangle$ [GeV/c], mean transverse momentum squared $\langle p_T^2 \rangle$ [(GeV/c)^2] as a function of x_F, as well as density distribution dn/dy as a function of y for p and $\overline{\text{p}}$. The relative statistical uncertainty Δ for each quantity is given in %

The corresponding distributions are shown in Figs. 55 and 56 for protons and anti-protons. The statistical errors of the integrated quantities are below the percent level with the exception of the anti-proton yields above x_F = 0.2 due to the limited size of the total data sample of 4.8 Mevents. This also sets a limit to the exploration of the interesting evolution of the mean transverse momentum of the anti-protons, Fig.56b, which rises from x_F = 0 to increase above the values for protons at $x_F > 0.2$. The similar behaviour of the mean pion transverse momentum [1] with a cross-over at x_F = 0.5 is also indicated in this Figure. The sizeable $\langle p_T \rangle$ of about

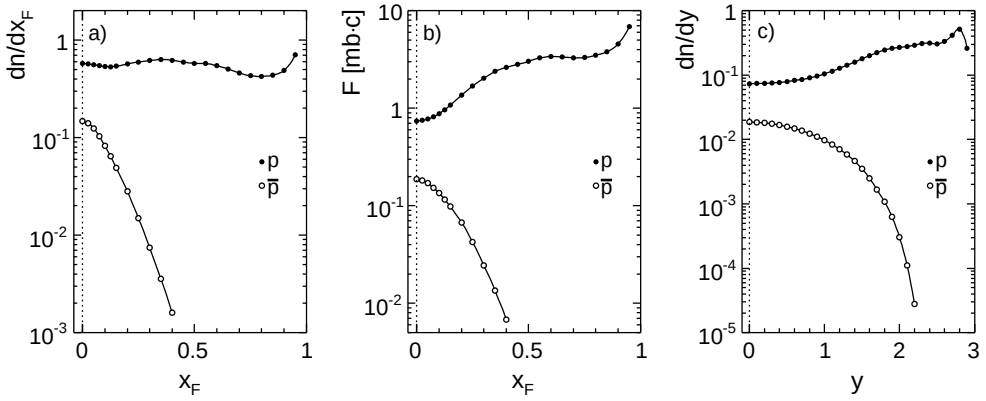

Figure 55: Integrated distributions of p and $\overline{\text{p}}$ produced in p+p interactions at 158 GeV/c: a) density distribution dn/dx_F as a function of x_F; b) invariant cross section F as a function of x_F; c) density distribution dn/dy as a function of y

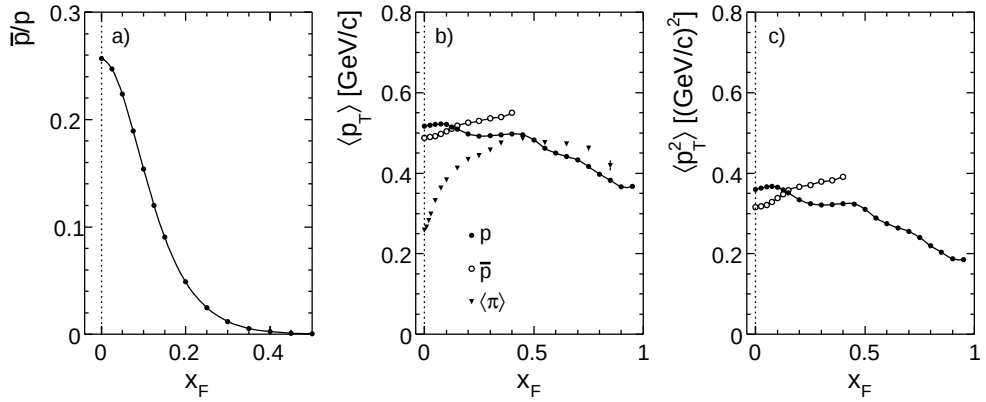

Figure 56: a) $\overline{\text{p}}$/p ratio, b) mean p_T, and c) mean p_T^2 as a function of x_F for p and $\overline{\text{p}}$ produced in p+p interactions at 158 GeV/c. In panel b) the mean p_T of $\langle\pi\rangle$ in also shown

0.5 GeV/c for all particle species at $x_F \sim 0.5$ remains a challenge to most current hadronization models.

10.2 Comparison to other data

Sufficient p_T coverage is needed to come to a bias-free evaluation of the integrated quantities defined above. The danger of using straight-forward analytic descriptions of limited data sets is illustrated in the comparison to the integrated yields of the Brenner et al. data [9]. As shown in Fig. 57 large and systematic deviations are resulting using data which are compatible on the few percent level for the measured double differential cross sections, see Sect. 8.2.

Here the apparent under-estimation of the related systematic uncertainties visible in the given error bars, Fig. 57b, is especially noteworthy. The systematic trend as a function of x_F happens to be opposite but equal in size to the one observed for pions [1].

In comparison, the EHS experiment at the CERN SPS [35] using a 400 GeV/c proton beam offers the necessary phase space coverage although this collaboration did not publish double differential data. The invariant integrated data presented in Fig. 58 show indeed a reasonable overall agreement as a function of x_F, with a few noticeable exceptions. For protons, Fig. 58, there is strong disagreement above x_F = 0.9. In fact the EHS data show no indication

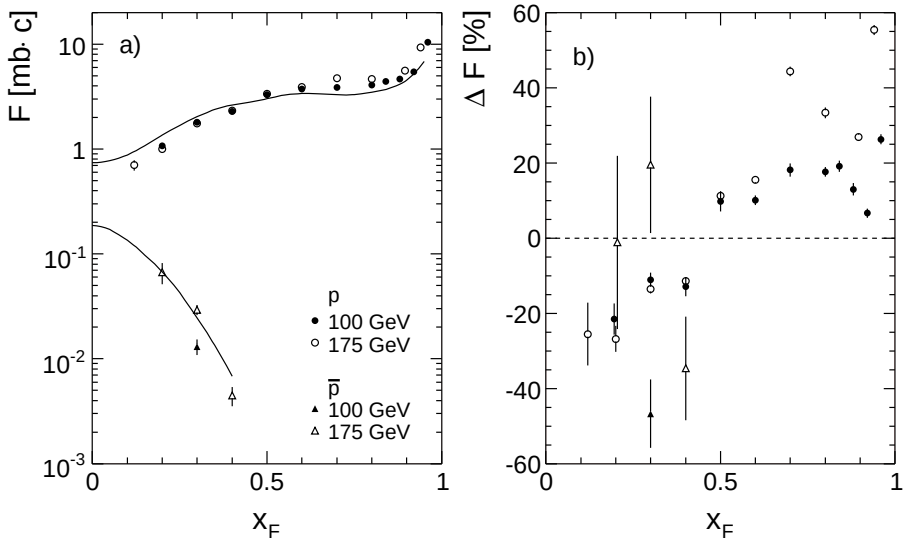

Figure 57: a) Comparison of p_T integrated invariant cross section F as a function of x_F for p and $\overline{\text{p}}$ measured by [9] to NA49 results (represented as lines); b) Deviation of the measurements of [9] from the NA49 results in percent

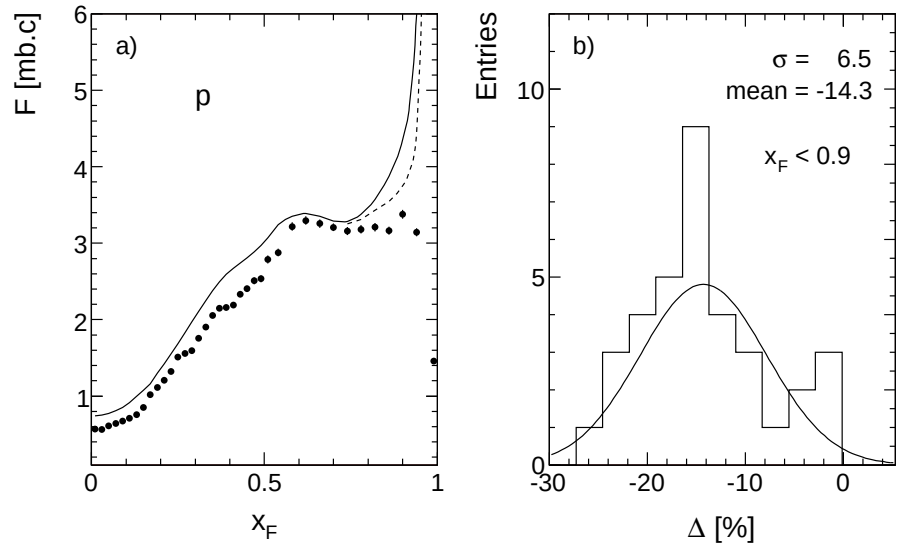

Figure 58: a) Comparison of p_T integrated invariant cross section F as a function of x_F for p measured by [35] to NA49 results (represented as lines); b) Distribution of the differences between measurements of [35] and NA49 in percent in the region of $x_F < 0.9$

at all of the presence of a diffractive peak. Even correcting the NA49 data for the s-dependent depletion in this area following Sect. 9 and also shown in Fig. 58 with a dashed line, this discrepancy remains present.

Evidently the trigger efficiency of only 77% of the total inelastic cross section (compared to 89% for the NA49 experiment) leads to uncorrected losses in the diffraction region of protons. In addition, correlated trigger bias corrections similar but sizeably bigger than in the NA49 case, see Sect. 6.2 and [1], have to be expected. This might explain part of the systematic downward shift of the invariant density by about 14% in the x_F region below 0.9, Fig. 58b, which in view

of the discussion of s-dependence in Sect. 9 is in contradiction to the accumulated ISR data.

For anti-protons, Fig. 59, an expected increase with $\sqrt{s}$ is borne out by an overall upward shift of about 12%.

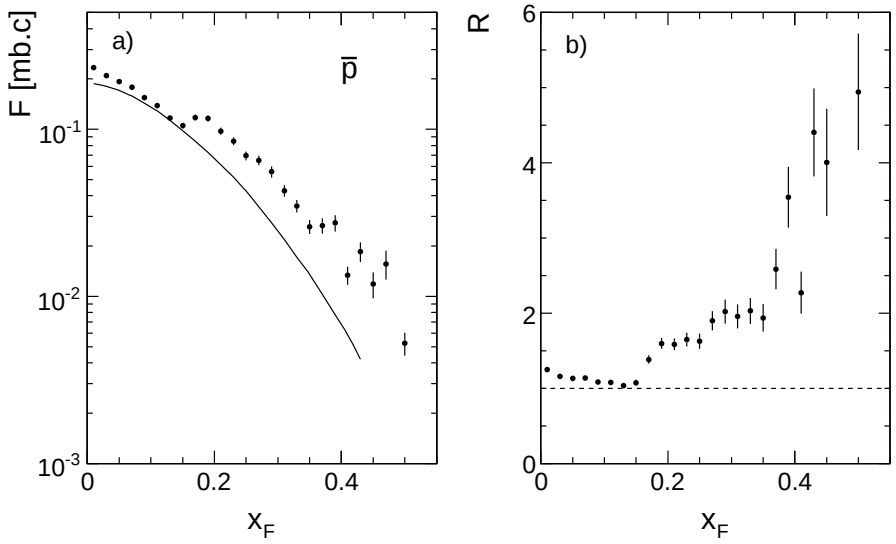

Figure 59: a) Comparison of p_T integrated invariant cross section F as a function of x_F for $\overline{\text{p}}$ measured by [35] to NA49 results (represented as lines); b) Ratio R as a function of x_F between measurements of [35] and NA49

There is however a strong local structure at x_F between 0.1 and 0.2 which is also present in the proton data (Fig. 60a) and which is in all probability due to apparatus effects. In addition the strong and apparently divergent increase of the anti-proton yields for $x_F > 0.2$, Fig. 59b, contradicts the flat x_F dependence of the $\overline{\text{p}}$ enhancement at ISR energies, Fig. 52e. This effect

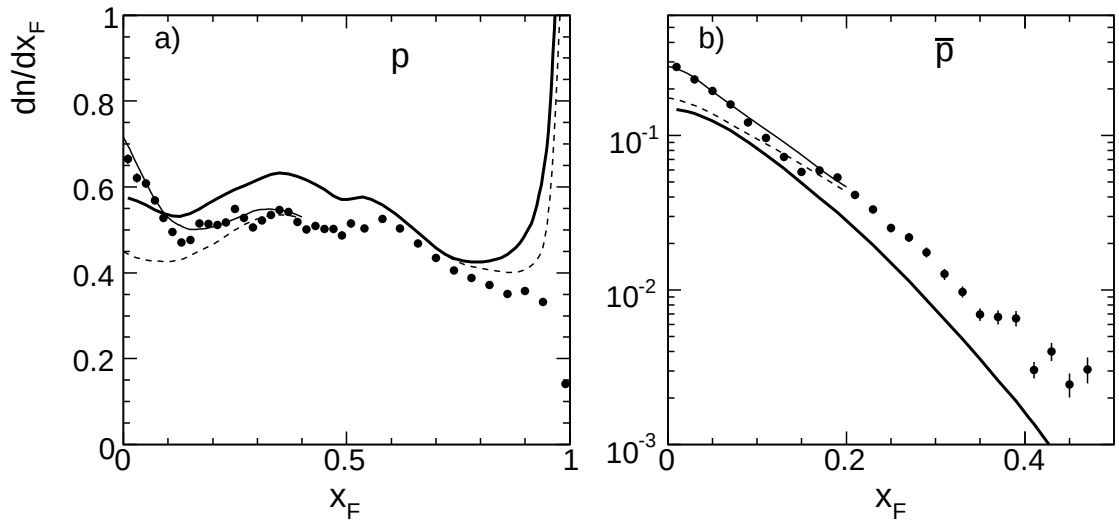

Figure 60: Comparison of p_T integrated non-invariant density dn/dx_F as a function of x_F for a) p and b) $\overline{\text{p}}$ measured by [35] to NA49 results (represented as thick lines). The difference between the thin and dashed lines shows the influence of the $\sqrt{s}/2E$ factor in Eq. 10 with respect to a scaling invariant cross section

is probably connected to the divergence of $\langle p_T^2 \rangle$ in the same x_F region, Fig. 62d. It is also to be compared to the erratic behaviour of the pion cross sections from this experiment in the same x_F region [1].

The non-invariant density distributions dn/dx_F for protons and anti-protons are shown in Fig. 60. They demonstrate the strong s dependence introduced by the factor $\sqrt{s}/E$ in Eq. 10 above. Only at $x_F > 0.2$ this factor reduces to the simple multiplicative term $1/x_F$.

The increase of particle density at $x_F \sim 0$ is practically equal to the increase of $\sqrt{s}$. This means that for an s independent invariant cross section at low x_F the total proton density will diverge with s in this region, thus creating a problem with baryon number conservation [33].

The rapidity distributions dn/dy of [35] are presented for protons and anti-protons in Fig. 61.

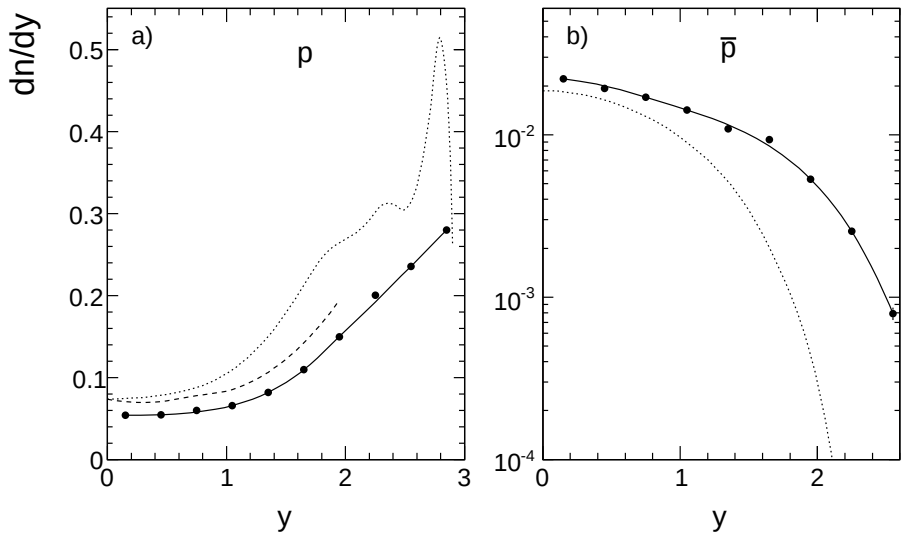

Figure 61: Comparison of p_T integrated density dn/dy as a function of y for a) p and b) $\overline{\text{p}}$ measured by [35] to NA49 results (dotted lines)

Here the extension of the y scale with increasing $\sqrt{s}$ should be noted, which is visualized in the EHS data re-normalized to NA49 at x_F = 0 also shown in Fig. 61 (dashed line). The shape comparison of hadronic rapidity distributions at different $\sqrt{s}$ hence suffers non-negligible systematic effects which are to be carefully taken into account.

Finally a comparison of the p_T integrated $\overline{\text{p}}$/p ratio and of the first and second moment of the p_T distributions as a function of x_F is presented in Fig. 62.

As there is no published $\langle p_T \rangle$ distribution available, the mean transverse momentum of Lambdas from EHS [36] is compared to protons in Fig. 62b. As far as $\langle p_T \rangle$ and $\langle p_T^2 \rangle$ are concerned, the measurements at the higher $\sqrt{s}$ follow, at increased levels, rather closely the shape of the NA49 data as a function of x_F. This has already been apparent for pions [1]. It remains however to be shown how much of the apparent increase has to be imputed to the absence of diffraction in the EHS data as opposed to a true s-dependence. In this context the even smaller fraction of the total inelastic cross section generally available for triggering at collider energies has to be mentioned. Also here the effects of this trigger bias should be evaluated before detailed conclusions may be drawn in comparison to lower energy data.

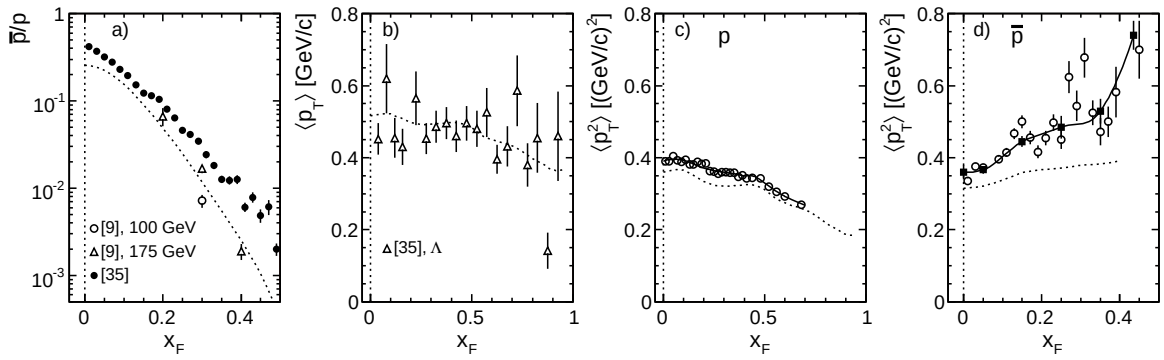

Figure 62: Comparison as a function of x_F of a) $\overline{\mathrm{p}}$/p ratio measured by [35] (full circles) and [9] (open symbols) to NA49 (dotted line) , b) mean p_T of Λ measured by [36] to mean p_T of protons measured by NA49 (dotted line); Comparison of mean p_T^2 for c) p and d) $\overline{\mathrm{p}}$ measured by [35] to NA49 results (dotted lines)

10.3 Total baryonic multiplicities

The integration over x_F of the dn/dx_F distributions presented in Table 9 results in the following total baryonic yields:

$$\begin{aligned} \langle n_{\mathrm{p}} \rangle &= 1.1623 \\ \langle n_{\overline{\mathrm{p}}} \rangle &= 0.03860 \\ \langle n_{\overline{\mathrm{p}}} \rangle / \langle n_{\mathrm{p}} \rangle &= 0.03321 \end{aligned} \tag{11}$$

The statistical errors of these quantities are negligible compared to the overall systematic uncertainty of about 2–3% given in Table 2.

10.4 Availability of the presented data

As in [1, 30] the tabulated values of NA49 data are available in numerical form on the Web Site [42]. In addition, the (x_F,p_T) distributions following from the two-dimensional interpolation, Sect. 7.3, are made available on this site.

11 Neutrons

11.1 NA49 results

The unfolded x_F distribution of the p_T integrated neutron yield has been shown in Fig. 7. In this yield there is no distinction between the different neutral hadronic particles. The measured cross section is therefore the sum of neutrons, pair produced neutrons, anti-neutrons and K_L^0 particles which are experimentally inseparable. As in the proton cross sections presented in this paper the contribution of pair produced protons has not been subtracted, the neutron yield may be defined as the total measured neutral hadron yield minus the K_L^0 and the anti-neutron contribution.

The K_L^0 cross section can be described, invoking isospin symmetry, by the average charged kaon yield which is available to the NA49 experiment [29]. The corresponding p_T integrated x_F distribution is shown in Fig. 63.

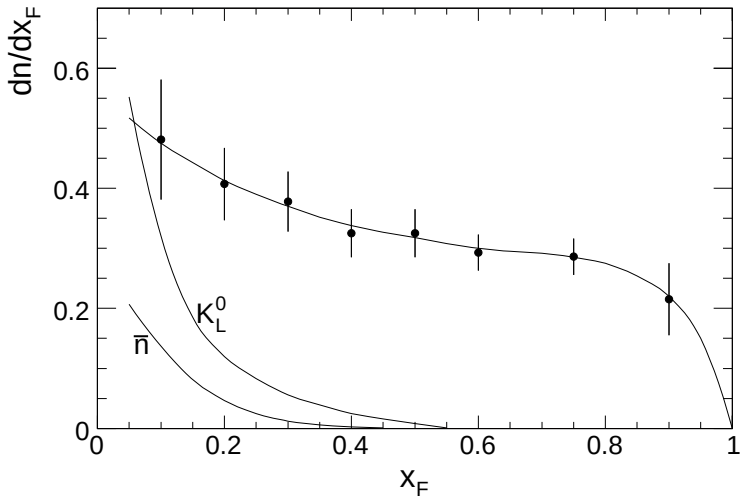

Figure 63: p_T integrated density distribution dn/dx_F as a function of x_F of neutrons produced in p+p interactions at 158 GeV/c. The subtracted K^0_L and anti-neutron distributions are also shown

The situation with pair produced neutrons is somewhat more complicated. In fact it has been shown that baryon pairs may be described as an isospin I = 1 triplet [33] with the structure given in Table 10.

I_3	-1	0	1
baryon pairs	$\overline{p}$n	$\overline{p}$p $\overline{n}$n	$\overline{n}$p
relative yield	0.5	1 1	1.5

Table 10: Isospin structure and relative yields of baryon pair production in p+p collisions

In p+p interactions it is reasonable to assume the relative yields given above which are typical of heavy isovectors with a relatively large suppression of the I_3 = -1 component with respect to I_3 = +1. From this table one gets the following predictions:

$$\begin{aligned} \text{p(pair produced)}/\overline{\text{p}} &= 1.66 \\ \text{n(pair produced)}/\overline{\text{n}} &= 0.60 \\ \overline{\text{n}}/\overline{\text{p}} &= 1.66 \end{aligned} \tag{12}$$

The first ratio is consistent with the result obtained by NA49 with a neutron beam [33]. In view of this it seems reasonable to subtract from the total neutral yield 1.66 times the anti-proton yield in order to obtain a definition of neutron production compatible with the one for proton production.

The resulting subtracted neutron dn/dx_F distribution as a function of x_F is shown in Fig. 63 together with the anti-neutron and K^0_L distributions used. Evidently these contributions represent an important background to be taken into account below $x_F \sim 0.4$.

The numerical values of the neutron yields are presented in Table 11.

x_F	dn/dx_F	Δ
0.1	0.481	20.8
0.2	0.407	14.7
0.3	0.378	13.2
0.4	0.325	11.5
0.5	0.325	12.3
0.6	0.293	10.2
0.75	0.286	10.5
0.9	0.215	27.9

Table 11: p_T integrated density distribution dn/dx_F for neutrons. The relative error Δ is given in %. It is governed by the systematic uncertainties quoted in Table 2

11.2 Comparison with other experiments

As shown in Sect. 2 there are only two available measurements of neutron production in the SPS/ISR energy range, [20–22]. Both experiments have produced double-differential cross sections measured at a set of fixed angles. The Fermilab data cover lab angles between 0.7 and 10 mrad, the ISR experiment between 0 and 119 mrad. The corresponding p_T distributions at

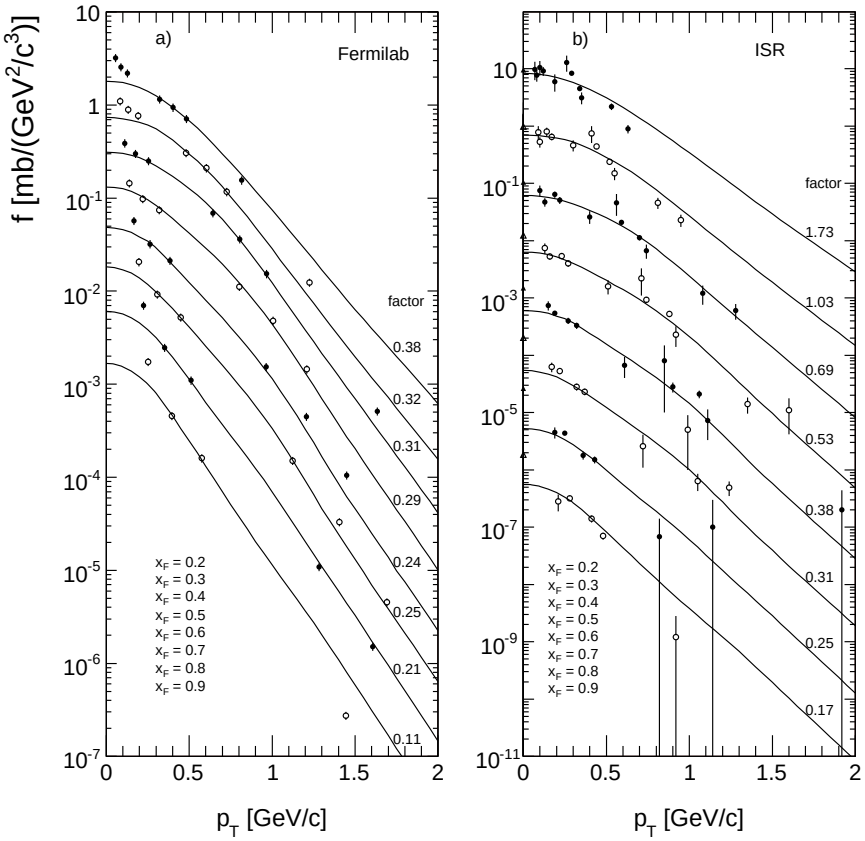

Figure 64: Neutron p_T distributions at fixed x_F for a) Fermilab [20] and b) ISR [21], superimposed with the interpolated NA49 proton data (lines) scaled with an appropriate normalization factor (indicated in figure). The data were successively divided by 3 for Fermilab distributions and by 10 for ISR distributions

fixed x_F are shown in Fig. 64 for both cases, superimposed with the NA49 proton data scaled with an appropriate normalization factor.

Evidently the proton transverse momentum distributions provide a fair description of the neutron data as a function of p_T in the range from 0.2 up to 1.7 GeV/c for [20] and from 0.1 to 1.7 GeV/c for [21]. However the "zero degree" data from both experiments with the calorimeter acceptance centered at 0.5 mrad [20] and 0 mrad [22] (triangles in Fig. 64b) respectively exhibit upward deviations which increase with x_F. This is shown in Fig. 65a,c by the n/p cross section ratio at p_T = 0, hand-extrapolated in the case of [20].

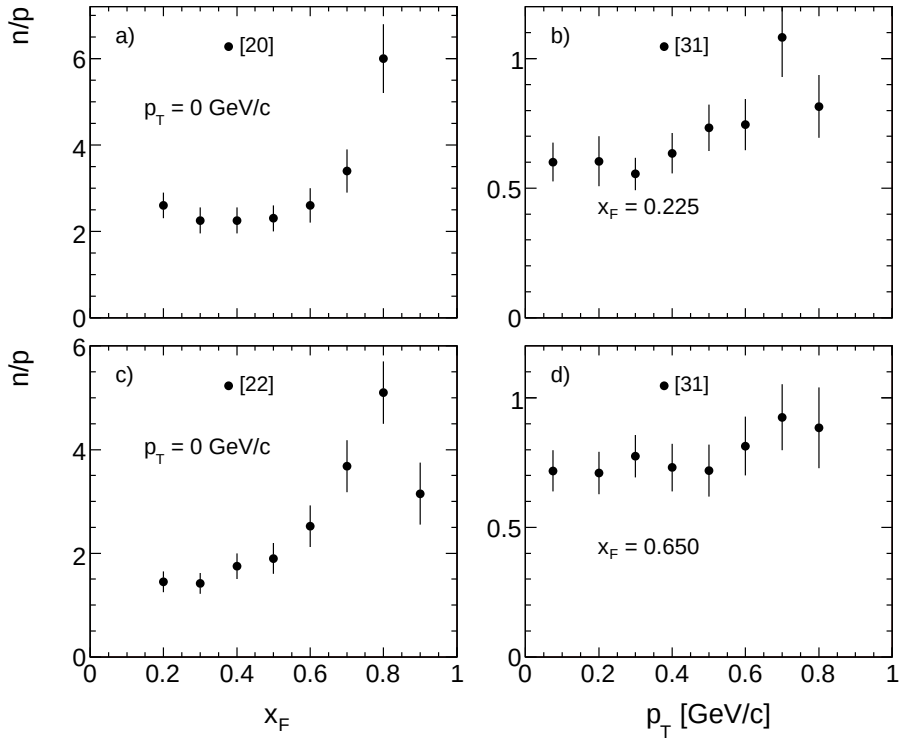

Figure 65: Neutron to proton cross section ratio: a) [20] and c) [22] at p_T = 0; b) and d) [31] at $\sqrt{s}$ = 6.8 GeV/c

Such an increase is not seen in the n/p ratio of the lower energy bubble chamber data of Blobel et al. [31] plotted in Fig. 65b,d as a function of p_T for two values of x_F. Also in the forward proton data of NA49 with neutron beam [37] which should, by isospin rotation, correspond to neutrons with proton beam, no peculiarity at low p_T is visible. On the other hand the effective p_T window covered by a finite size calorimeter acceptance increases linearly with x_F. It reaches 0.4 GeV/c at x_F = 0.9 for [20], including the singular point at p_T = 0 for the lowest angle setting. The proper evaluation of the bin center and of the binning correction to be applied can be rather involved in this case. The observed low-p_T enhancement might therefore be assumed to be a detector effect.

Under this assumption the normalization factors between neutron and proton p_T distributions, Fig. 64, may be used directly to determine the p_T integrated neutron yields of [20, 21] from the NA49 proton yields presented in Table 9. They are compared to the NA49 neutron measurement in Fig. 66a.

Evidently both measurements deviate strongly from the NA49 results. These deviations are given as relative factors in Figs. 66b and 66c. A non-trivial pattern emerges.

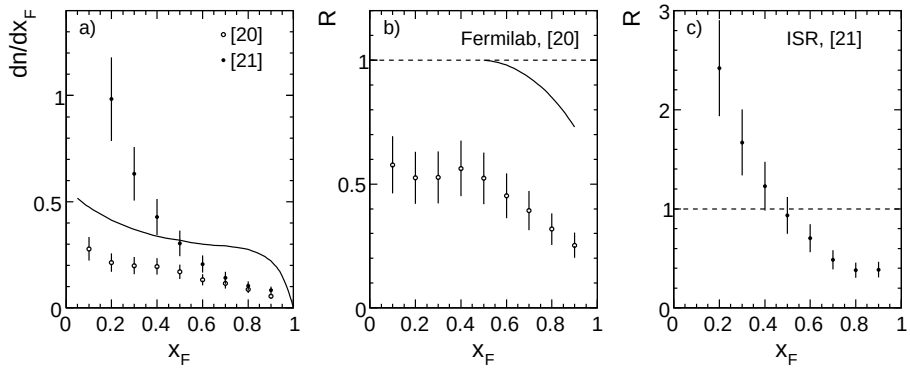

Figure 66: Comparison as a function of x_F of the NA49 results on neutron density with measurements [20, 21]; a) dN/dx_F, full line NA49, b) ratio R between [20] and NA49 and c) ratio R between [21] and NA49. The effect of calorimeter resolution is shown by the full line in panel b)

For the Fermilab data there seems to be a constant suppression of about a factor of 2 up to $x_F \sim 0.6$, followed by a sharp decrease towards larger x_F. As in [20] no mentioning is made of any calorimeter resolution unfolding this decrease is reminiscent of the ratio of raw and unfolded data of NA49 also shown in Fig. 66b. For the lower x_F range it should be mentioned that a subtraction of K^0_L has been performed.

For the ISR data the measured neutron yields are equal to NA49 in a small region between x_F = 0.4 and x_F = 0.5. For lower x_F the yield ratio increases sharply. As for these data no anti-neutron and K^0_L correction has been attempted (with the exception of K^0_L subtraction for the 0 degree data), and as the fringe of the calorimeter resolution touches x_F = 0 already for the momentum setting at x_F = 0.2, sizeable contributions from anti-neutrons and K^0_L must be expected here. In the x_F region above 0.6 again a sharp drop of the ratio is observed. In this case, however, the calorimeter resolution has been unfolded at least for the lowest angle setting.

The following conclusions may be drawn from the discussion of the data sets [20–22]:

- The shape of the neutron transverse momentum distributions is well described by the respective proton distributions over the full range of x_F measured and for $p_T > 0.2$ GeV/c. In the lowest p_T bins containing p_T = 0 both experiments show an upward trend with respect to the proton distributions which is probably due to apparatus plus binning effects.
- The extracted, p_T integrated neutron yields deviate by sizeable factors from the NA49 data. For the Fermilab experiment this difference may be described by a constant factor of ∼0.52 plus an effect of the non-unfolded calorimeter resolution in the large x_F region. For the ISR experiment there are continuous and large deviations over the full x_F scale. At $x_F < 0.4$ the missing K^0_L and $\overline{n}$ subtraction certainly governs the observed pattern, with neutron densities exceeding the measured proton yields already at x_F = 0.3. In view of the unfolding procedure claimed in [20, 21] the sharp decrease towards high x_F has to remain unexplained.
- The use of these data for quantitative yield comparisons is not to be recommended.

12 Leptoproduction and hadronic factorization

Recent precision data from the ZEUS collaboration at HERA concerning proton [38] and neutron [39] production provide results at mean energies of about 130 GeV in the photon-proton cms. These data allow for a rather detailed comparison to the p+p interaction in the region above

ISR and up to RHIC energies where little if any experimental information is available from hadronic reactions.

12.1 Proton production

The ZEUS proton data [38] cover ranges from 0.1–0.7 GeV/c in p_T and from 0.6 to 0.99 in x_F. Transverse momentum distributions at 6 values of x_F are compared in shape to the renormalized NA49 data in Fig. 67.

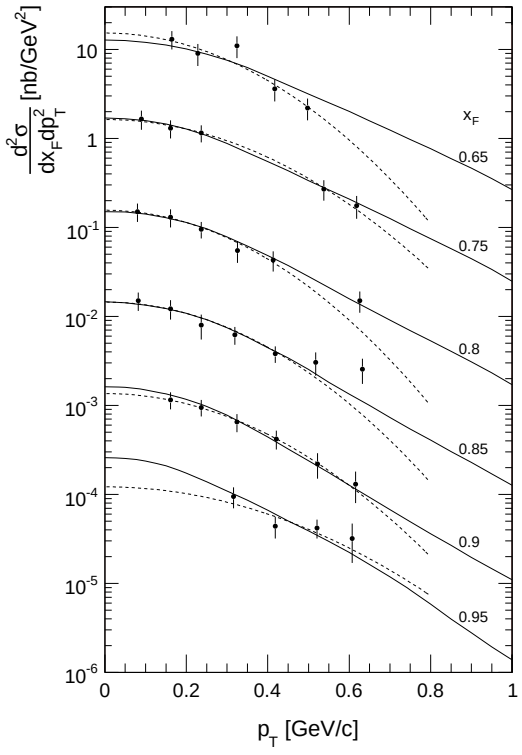

Figure 67: Comparison of the proton p_T distributions at several x_F values of the NA49 results (full lines) with measurements from [38]. The data were successively divided by 10 for different x_F values for better separation. The dashed lines represent the parametrization used in [38]

Evidently the HERA data follow the shape of the lower energy pp data rather precisely within the quoted statistical errors. This complies with the s-independence of the p_T distributions up to $\sqrt{s}$ = 53 GeV and up to p_T = 1.5 GeV/c in the same x_F range, see Fig. 41. The Gaussian fits used in [38] and shown as dashed lines in Fig. 67 describe the measured cross sections reasonably well with some exceptions in x_F. They deviate however systematically from the NA49 data already at the highest p_T values available in [38]. In fact a Gaussian approximation of the proton transverse momentum distributions is at best only valid over very restricted regions. This has been discussed in connection with the low-p_T extrapolation of the hadronic data in Sect. 7.2 and has led to the application of the two-dimensional interpolation scheme, Sect. 7.3, which does not rely on any algebraic parametrization. The extension of the p_T range of the HERA data up to and beyond the GeV/c region would of course be very interesting but has to remain on the wish list for eventual future work on leptoproduction.

A comparison of p_T integrated yields as they are given in [38] for the measured ranges of $p_T^2 < 0.04$ and < 0.5 (GeV/c)^2 to the NA49 data integrated over the same ranges is presented in Fig. 68.

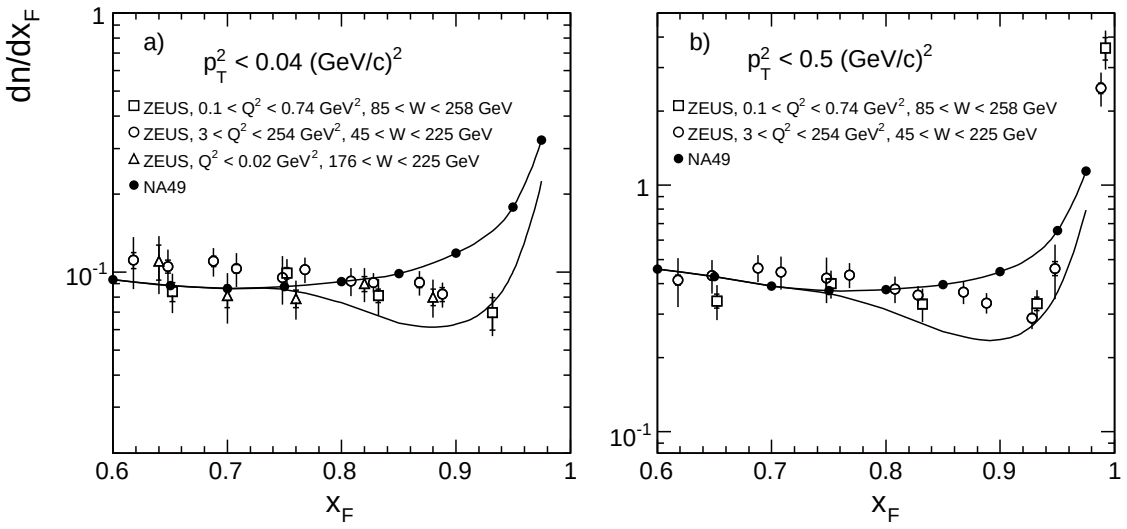

Figure 68: Comparison of the proton p_T integrated distributions as a function of x_F of the NA49 results with measurements from [38]. The integration is performed in the range of p_T^2 less than: a) 0.04 (GeV/c)^2 and b) 0.5 (GeV/c)^2. The full symbols and lines: NA49

The good quantitative agreement of the proton densities up to $x_F \sim 0.8$ in both p_T windows is noteworthy. This may shed some light on the question of scaling versus increase of total inelastic cross section in this energy regime as mentioned in Sect. 9.1. As the photonic total cross section rises at least as fast as the hadronic one with cms energy, Fig. 69, a non-scaling of the invariant cross sections as opposed to particle densities is necessarily implied by baryon number conservation.

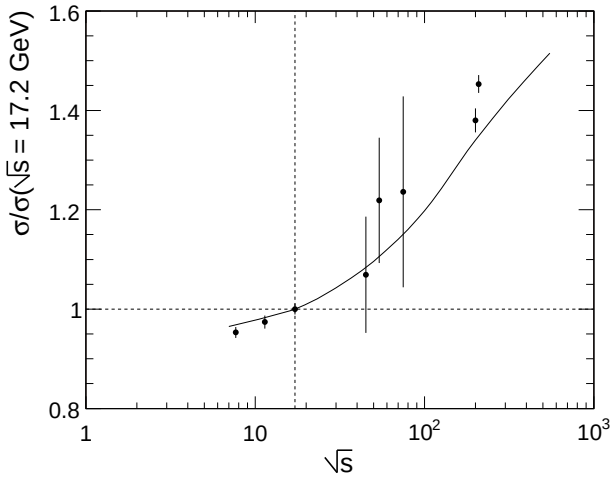

Figure 69: Total inelastic cross section normalized at $\sqrt{s}$ = 17.2 GeV as a function of $\sqrt{s}$ for p+p (line) and γ+h (circles) interactions

It is also interesting to regard the high-x_F suppression extracted in Sect.9 from ISR and collider data, Fig. 46, in connection with the HERA data. The expected decrease of proton density above $x_F \sim 0.7$ is indicated by the lower line in Fig. 68. This effect will again be discussed in relation to neutrons below.

12.2 Neutron production

The ZEUS neutron data [39] cover ranges from 0.05–0.6 GeV/c in p_T and from 0.26 to 0.97 in x_F. As already shown for protons, the relative shape of the neutron p_T distributions is well described by the NA49 proton data in the measured p_T ranges, see Fig. 70

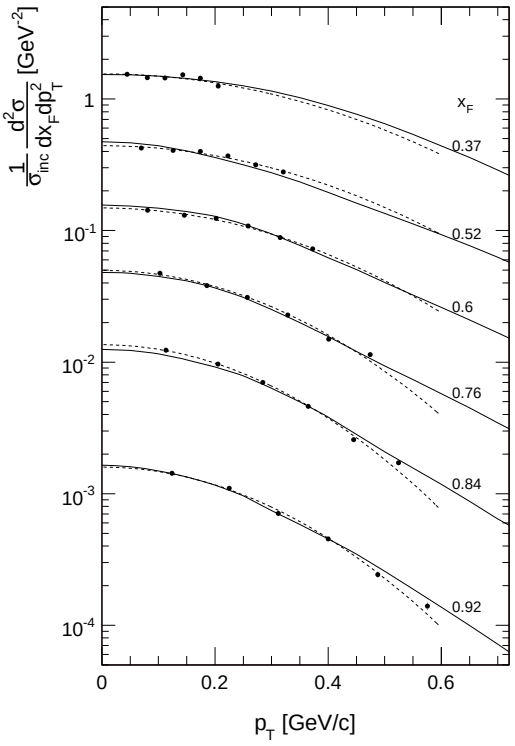

Figure 70: Comparison of the p_T distributions at different x_F values of protons from NA49 (full lines) with neutrons from [39]. The data were successively divided by 3 for different x_F values for better separation. The dashed lines represent the parametrization used in [39]

This shape similarity verifies the result for lower-energy neutron distributions, Fig. 64, where the comparison reaches up to $p_T \sim 1.5$ GeV/c. Again the Gaussian parametrization chosen by [39] is indicated by dashed lines, and again the limited applicability of such parametrization is evident especially if total p_T integrated yields are to be extracted.

An interesting comparison of the yields $dn/dxdp_T^2$ at p_T = 0 [39] with the NA49 data becomes possible under the assumption that the p_T distributions of neutrons are identical to the ones of protons in p+p interactions. This does not look unreasonable in view of the results shown above. With this assumption the total measured neutron yields of NA49, Table 11 and Fig. 63, may be converted into p_T = 0 densities using the proton p_T distributions shown in Fig. 70. The resulting absolute densities $dn/dxdp_T^2$ are presented in Fig. 71.

This Figure exhibits an interesting pattern. In the region $0.45 < x_F < 0.7$ both yields are equal to within about 7-8%. This difference is compatible with the systematic errors of the NA49 data given in Table 2. At lower x_F the ZEUS data increase, towards large x_F they decrease with respect to the p+p data. This is quantified in the yield ratio of Fig. 71b.

The enhancement of the ZEUS data for $x_F < 0.5$ may be connected to two effects. A first contribution is given by the production of K_L^0 and anti-neutrons which are experimentally not separable in the used calorimeter. This contribution appears in the x_F region in question

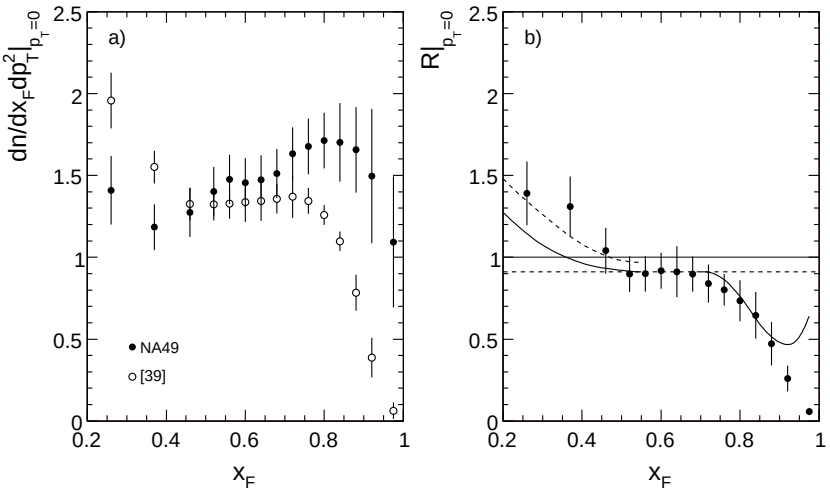

Figure 71: Comparison of the neutron data from [39] to NA49 results as a function of x_F at p_T = 0 GeV/c: a) $dn/dx_F dp_T^2$, b) ratio R between [39] and NA49 results

and has been subtracted from the NA49 data, see Sect. 11 and Fig. 63. At HERA energies the corresponding cross sections must be expected to increase over their values at $\sqrt{s}$ = 17.2 GeV. Existing measurements of K_S^0 at RHIC and p+$\overline{\text{p}}$ collider energies [40] do however not allow for a consistent analysis of this situation. An increase by up to a factor of two can nevertheless not be excluded. Allowing for the same percentage contribution to the neutron yield as in the NA49 data, the lower solid line in Fig. 71b is obtained.

A second contribution has to be expected from the feed-down of neutrons and anti-neutrons from weak decays of strange hyperons. As the ZEUS calorimeter is placed at a distance of several decay lengths of the contributing hyperons, the fraction of decays into neutrons defines the principle component. For a quantitative elaboration of this effect a detailed simulation of the experimental set-up, especially of the aperture limitations, is of course mandatory. Adding however the percentage contribution to the neutron yields as calculated for the NA49 data, Sect. 6.4, the upper dashed line in Fig. 71b is obtained. Although this procedure is of course to be seen as a mere exercise, the two effects described certainly value a more detailed scrutiny.

The decrease of the ZEUS data at $x_F > 0.7$ can on the other hand be connected to the s-dependent yield depletion observed for protons and already invoked in the preceding chapter on proton production. Indeed there is no reason why neutrons should not show a similar effect. In fact, due to the absence of a diffractive peak in the neutron hemisphere, the effect might be enhanced at $x_F > 0.9$. This is indeed seen in Fig. 71b. Here the depletion as a function of x_F has been evaluated for HERA energy and applied to the NA49 neutron data. This results in the solid line at $x_F > 0.7$ which describes the rough structure up to $x_F \sim 0.9$. The minimum at x_F = 0.92 and the subsequent increase towards the diffractive proton peak is of course not to be expected for neutron production.

As expected from the shape similarity of the transverse momentum distributions of neutrons and protons, Fig. 70, the comparison of the p_T integrated yields also given in [39] gives similar results. Two integrations, one with an x_F dependent p_T window of $p_T < 0.69 x_F$ and one with a constant window up to p_T = 0.2 GeV/c are compared in Fig. 72a and 72b, respectively.

In Fig. 72a the NA49 results are given as solid line, the ZEUS results for the full DIS sample with $\langle Q^2 \rangle$ = 13 GeV^2 as the dashed line. In addition the ZEUS data points for three

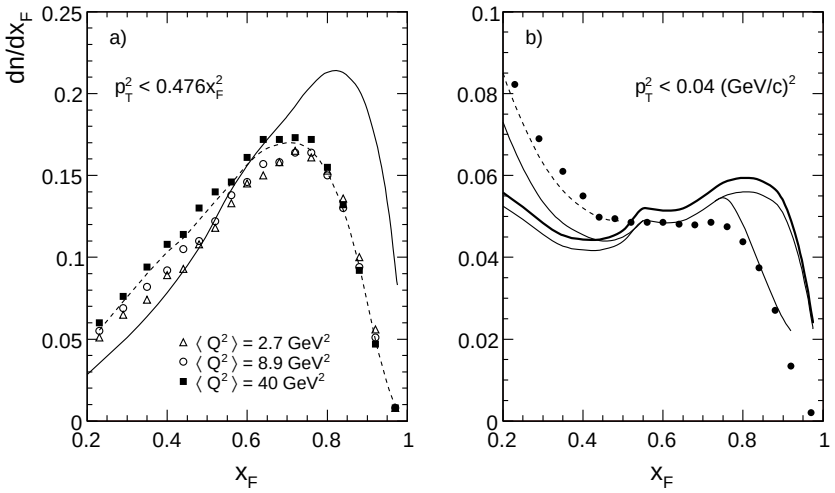

Figure 72: Comparison of the p_T integrated neutron data from [39] to NA49 results (full lines) as a function of x_F; a) p_T integration is performed in the range $p_T < 0.69 x_F$, b) p_T integration at $p_T < 0.2$ GeV/c

subsamples with different $\langle Q^2 \rangle$ are presented. The pattern of enhancement below $x_F \sim 0.5$ and depletion above $x_F \sim 0.7$ is very similar to Fig. 71a. This is also apparent in Fig. 72b with a constant p_T integration window. Here the NA49 results are given as thick line and compared to the ZEUS data points corresponding to the full DIS sample. A re-normalization of the NA49 yield by about 6% at $x_F = 0.6$ (see also Fig. 71) is indicated as a thin line. The contributions from K^0_L and $\overline{n}$ production, from hyperon feed-down as well as the high-x_F depletion are referred to this line as in Fig. 71b.

12.3 Hadronic factorization

The equality, within the experimental errors, of the production of forward protons and neutrons in deep inelastic e+p collisions to the purely hadronic p+p interaction is reminiscent of hadronic factorization, that is of the independence of target fragmentation on the type of hadronic projectile used. This factorization has been well established with pion, kaon and baryon beams on a proton target. In this sense the above results would indicate the virtual photon to act as an $I_3 = 0$ mesonic state. The important point here is that the observed factorization extends to low x_F values, well into the region of non-diffractive hadronic collisions, where it has been shown that neither charge nor flavour exchange is present in the hadronic sector, see for instance the discussion in [41]. The detailed study of other particle species also in the region of central rapidity and of the long-range correlations (or their absence) with the photon hemisphere would be mandatory to further clarify this situation.

13 Conclusion

New inclusive data on proton, anti-proton and neutron production in p+p interactions at SPS energy have been presented. These data represent a continuation of the systematic study of hadronic collisions by the NA49 experiment at 158 GeV/c beam momentum. They offer an unprecedented coverage of the available phase space with double differential inclusive cross sections featuring systematic errors in the few percent range. This allows for a very detailed comparison with existing data with the aim at establishing a reliable data base up to ISR energies

including especially the hitherto unclear situation concerning neutron production. In this context several points are noteworthy:

- the consolidation of the wealth of data available in the SPS and ISR energy ranges, mostly obtained some 30 years ago, has been attempted here with only partially satisfactory results, in particular concerning neutrons.
- the necessity of taking care of baryonic feed-down from strange hyperons on a quantitative level has been demonstrated.
- the global independence of transverse momentum distributions up to about 1.5 GeV/c on reaction type and $\sqrt{s}$ and their equality for protons and neutrons has been shown.
- the s-dependence through the ISR energy range and up to HERA and p+$\overline{\text{p}}$ collider energies has been investigated. In particular a specific yield suppression at $x_F > 0.7$ with increasing cms energy has been quantified.
- the question of the scaling of baryon yields versus cross sections has been addressed in the context of the rapid increase of the total inelastic cross sections with interaction energy. Scaling of yields rather than cross sections is necessary in order not to violate baryon number conservation.
- the comparison to deep inelastic lepton scattering establishes hadronic factorization also in this reaction within the experimental uncertainties and the phase space region available.

Finally it should be stated that the establishment of a precise base of single inclusive data on baryon production is only a first step in an effort to shed some light on the general problem of baryon number transfer. The transition from the incoming baryonic target or projectile to the observed final state is, as a part of the non-perturbative sector of QCD, not understood on the level of any reliable theory. In hadronic interactions, most approaches are using ad-hoc assumptions like for instance the concept of di-quark fragmentation. In electroproduction baryon production is described in most approaches by the scattering of the virtual photon off an exchange pion. There is no doubt that this situation can only be clarified by further and more detailed experimental studies which go beyond the single inclusive level.

One of these experimental openings is the study of resonance production and decay which is accessible to the NA49 detector via its good phase space coverage. This widely neglected field will provide very strong constraints concerning the repartition of particle species as products of the cascading decay of heavy resonances, especially concerning the relation between neutrons and protons as it is given by the isospin structure of the initial state. Another field of studies concerns internal baryonic correlations. By selecting a leading proton in either the target or the projectile hemisphere the forward-backward correlation of baryon number transfer may be studied, in particular the feed-over of baryon number from one hemisphere to the other and its evolution with interaction energy. The use of neutron projectiles and of non-baryonic, mesonic beams as they are available in fixed-target operation opens the possibility of model-independent studies essentially relying on baryon number conservation and concepts like isospin symmetry.

In this context the study of nuclear reactions, in particular of proton-nucleus and pion-nucleus scattering with controlled centrality, provides unique access to multiple hadronic interactions. The strong dependence of the final state baryon distributions on the number of projectile subcollisions inside the nucleus, generally misnamed as ”stopping” and as yet not understood on any theoretical level, offers a further and very strong constraint on the possible mechanism of baryon number transfer.

Acknowledgements

This work was supported by the Bundesministerium fuer Forschung und Technologie (06F137), the Polish State Committee for Scientific Research (P03B00630), the Polish Ministry of Science and Higher Education (N N202 078735), the Hungarian Scientific Research Fund OTKA (T68506), the Bulgarian National Science Fund (Ph-09/05) and the EU FP6 HRM Marie Curie Intra-European Fellowship Program.

References

[1] C. Alt et al., Eur. Phys. J. **C45** (2006) 343
[2] D. Antreasyan et al., Phys. Rev. **D19** (1979) 764
[3] F. Sannes et al., Phys. Rev. Lett. **30** (1973) 766
[4] S. Childress et al., Phys. Lett. **B65** (1976) 177
[5] R. D. Schamberger et al., Phys. Rev. **D17** (1978) 1268
[6] Y. Akimov et al., Phys. Rev. Lett. **39** (1977) 1432
[7] J. W. Chapman et al., Phys. Rev. Lett. **32** (1974) 257
[8] J. Whitmore et al., Phys. Rev. **D11** (1975) 3124
[9] A. E. Brenner et al., Phys. Rev. **D26** (1982) 1497
[10] J. R. Johnson et al., Phys. Rev. **D17** (1978) 1292
[11] M. G. Albrow et al., Nucl. Phys. **B51** (1973) 388
[12] M. G. Albrow et al., Nucl. Phys. **B54** (1973) 6
[13] M. G. Albrow et al., Nucl. Phys. **B73** (1974) 40
[14] M. G. Albrow et al., Nucl. Phys. **B108** (1976) 1
[15] M. G. Albrow et al., Phys. Lett. **B42** (1972) 279
[16] M. G. Albrow et al., Nucl. Phys. **B56** (1973) 333
[17] P. Capiluppi et al., Nucl. Phys. **B79** (1974) 189
[18] B. Alper et al., Nucl. Phys. **B100** (1975) 237
[19] K. Guettler et al., Nucl. Phys **B116** (1976) 77
[20] M. R. Whalley et al., UM HE 79-14 (1979)
[21] J. Engler et al., Nucl. Phys. **B84** (1975) 70
[22] W. Flauger, F. Mönnig, Nucl. Phys. **B109** (1976) 347
[23] S. Afanasiev et al., Nucl. Instrum. Meth. **A430** (1999) 210
[24] D. Varga, PhD Thesis, Dep. of At. Phys., Eötvös Loránd University, Budapest (2003)
[25] C. De Marzo et al., Phys. Lett. **B112** (1982) 173
[26] C. De Marzo et al., Nucl. Instrum. Meth. **217** (1983) 405
[27] V. Eckardt et al., Nucl. Instrum. Meth. **155** (1978) 389
[28] W. W. M. Allison, J. H. Cobb, Ann. Rev. Nucl. Part. Sci. 30:253-298 (1980)
J. Berkowitz, Atomic and molecular photoabsorption, 1: Absolute total cross section, Academic press (2002)
[29] Inclusive charged kaons production at SPS energies, NA49 collaboration, to be published
[30] C. Alt et al., Eur. Phys. J. **C49** (2007) 897
[31] V. Blobel et al., Nucl. Phys. **B69** (1974) 454
[32] V. V. Abramov et al., Nucl. Phys. **B173** (1980) 348
[33] H. G. Fischer et al., Heavy Ion Phys. **17** (2003) 369

[34] M. Bozzo et al., Phys. Lett. **B136** (1984) 217
[35] M. Aguilar-Benitez et al., Z. Phys. **C50** (1991) 405
[36] J. L. Bailly et al., Z. Phys. **C35** (1987) 295
[37] Hadron production with a neutron beam at SPS, NA49 collaboration, to be published
[38] S. Chekanov et al., Nucl. Phys. **B658** (2003) 3
[39] S. Chekanov et al., Nucl. Phys. **B776** (2007) 1
[40] J. Adams et al., Phys. Lett. **B637** (2006) 161
D. Acosta et al., Phys. Rev. **D72** (2005) 052001
G. Bocquet et al., Phys. Lett. **B366** (1996) 441
R. E. Ansorge et al., Z. Phys. **C41** (1988) 179
T. Alexopoulos et al., Phys. Rev. **D48** (1993) 984
[41] G. Barr et al., Eur. Phys. J. **C49** (2007) 919
[42] http://cern.ch/spshadrons, document S8
[43] F. Videbaek, nucl-ex/0801.1696v1 (2008)
[44] A. Rybicki et al., MESON 2008 Krakow, June 2008, to appear in Int. J. Mod. Phys. A
[45] M. Della Negra et al., Phys. Lett. **B59** (1975) 401
[46] R. Cottrell et al., Phys. Lett. **B55** (1975) 341